Dissertation

submitted to the
Combined Faculties of the Natural Sciences and Mathematics
of the Ruperto-Carola-University of Heidelberg, Germany
for the degree of
Doctor of Natural Sciences

Put forward by

Dipl.-Phys. Alexander Windberger

born in: Timişoara, Romania

Oral examination: 29.04.2015

Identification of optical transitions in complex highly charged ions for applications in metrology and tests of fundamental constants

Gutachter: PD Dr. José R. Crespo López-Urrutia

Prof. Selim Jochim

Identification of optical transitions in complex highly charged ions for applications in metrology and tests of fundamental constants

Forbidden optical transitions in highly charged ions have become subject of extensive theoretical investigations due to their suitability as next generation frequency standards and for tests on a possible variation of the fine structure constant α. In particular, a level crossing in the Nd-like ion Ir^{17+} provides optical transitions with the highest sensitivity to such a variation ever predicted for a stable atomic system. However, the vast majority of the proposed ions have never been investigated experimentally, and accurate theoretical calculations are difficult due to complex electron correlations. This work explores the optical spectra of Nd-like W, Re, Os, Ir, and Pt with the Heidelberg electron beam ion trap. A method has been developed to identify fine structure transitions in isoelectronic sequences by exploiting the scaling of transition energies depending on the atomic number Z. This method was independently validated by the analysis of the Zeeman splitting in high resolution and accuracy spectra of the brightest Ir^{17+} lines. Advanced atomic structure calculations could be experimentally tested for the first time in this class of complex ions providing a benchmark for future calculations. From the achieved identifications, the transition energies of proposed frequency standards in Hf^{12+} and W^{14+} were inferred, as well as possible values for the sought-after α-sensitive M2/E3 transition energies in Ir^{17+}.

Identifikation optischer Übergänge in komplexen hochgeladenen Ionen mit Anwendungen in der Metrologie und zum Test fundamentaler Konstanten

Auf Grund ihrer vielversprechenden Eigenschaften als Frequenzstandard und zum Test einer möglichen Variation der Feinstrukturkonstanten α, sind verbotene optische Übergänge in hochgeladenen Ionen Gegenstand ausführlicher theoretischer Studien. Insbesondere das Ion Ir^{17+} ermöglicht, durch eine Niveauentartung, optische Übergänge mit einer Empfindlichkeit auf eine solche Änderung, die in stabilen atomaren Systemen unerreicht ist. Trotz dieser Vorteile wurde die überwiegende Mehrheit der vorgeschlagenen Ionen experimentell bisher nicht untersucht und die Genauigkeit theoretischer Vorhersagen wird durch komplexe Elektronenkorrelationen eingeschränkt. Dieser Arbeit ist der Erforschung solcher Systeme gewidmet. Die optischen Spektren von Nd-artigem W, Re, Os, Ir und Pt wurden in der Heidelberger Elektronenstrahl-Ionenfalle vermessen. Mithilfe einer neu entwickelten Methode konnten Feinstrukturübergänge in den Spektren identifiziert werden, indem die Skalierung der Übergangsenergien als Funktion der Ordnungszahl Z ausgenutzt wurde. Diese Methode konnte durch die Analyse hochaufgelöster und hochgenauer Spektren der hellsten Ir^{17+} Linien überprüft werden. Die diese Arbeit unterstützenden Atomstrukturberechnungen konnten durch die durchgeführten Messungen zum ersten Mal für diese Klasse von komplexen Ionen getestet werden. Ein solcher Vergleich stellt eine wichtige Referenz für zukünftige Berechnungen dar. Aus den Identifikationen konnten die Übergangsenergien zweier vorgeschlagener Frequenzstandards in Hf^{12+} und W^{14+} abgeleitet sowie mögliche Energien der gesuchten α-empfindlichen M2/E3 Übergänge in Ir^{17+} vorgeschlagen werden.

Contents

Chapter 1

Introduction

The fine structure constant α

The state of the art understanding of elementary particles and their interactions is condensed in the Standard Model of Particle Physics (see figure 1.1). It can be divided into quarks and leptons, the elementary particles interacting with each other through fields to form the matter the world is composed of. The three fundamental forces between interacting particles and fields are conveyed by quanta of these fields represented by gauge bosons. On smallest scales, quarks are linked to each other by exchanging gluons, the gauge boson of the strong interaction, and thus building up the tightly bound hadrons. Although there are three elementary particle generations, all naturally abundant matter consists of the lightest generation. The reason for this is a second fundamental interaction, the weak interaction. Through emitting weak interaction gauge bosons, the second and third generations can decay into the lighter, energetically favorable first one. The lightest hadrons are protons and neutrons, the constituents of atomic nuclei. The third fundamental interaction, the electromagnetic or Coulomb interaction, is the most frequent one in everyday life. It is responsible for the attraction and repulsion of electrically charged particles by exchanging virtual photons, the gauge bosons of the Coulomb interaction. By these means, the electrically charged, or for simplicity just charged, nuclei attract electrons classified as first generation leptons, and keep them in stable bound states thus leading to the formation of atoms.

In the Standard Model, the magnitude of the strength of interaction between an electromagnetic field and a charged particle is given by the coupling constant

$$\alpha = \frac{e^2}{4\pi\epsilon_0\hbar c}, \tag{1.1}$$

with the elementary charge e, the vacuum permittivity ϵ_0, the reduced Planck constant $\hbar$, and the vacuum speed of light c. Hence, α is directly related to light-matter interaction

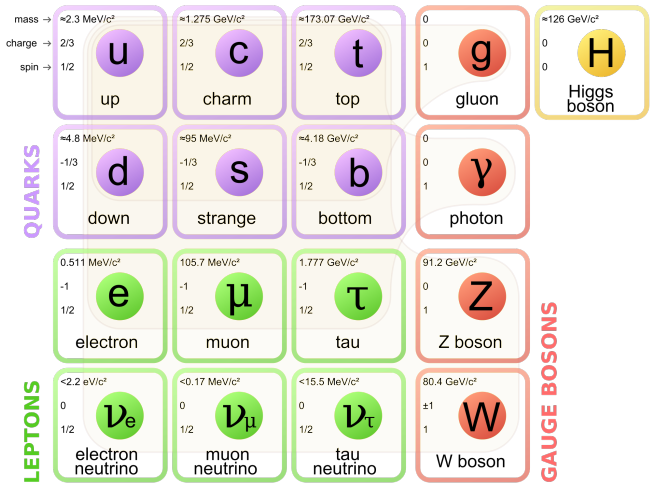

Figure 1.1: Illustration of the elementary particles of the SM.[1]

processes. The higher the value of α is the more virtual photons will be scattered off charged particles in an electromagnetic field, which increases the momentum transfer rate and therefore the force. The consequential importance of α for atomic processes can be emphasized by its first introduction through Sommerfeld in 1916 [2]. Here, the same constant was interpreted in a very different way even before the development of a quantum field theory to explain a substructure, introduced as fine structure, in the spectra of hydrogen atoms that was not predicted by Bohr's theory [3]. Sommerfeld expanded the scope of Bohr's theory from the originally circular electron orbit with index n around a nucleus to relativistic Kepler-ellipsoids and added a correction to the electron energy $E_{\mathrm{Bohr,n}}$ emerging from Bohr's theory as an polynomial expansion around v_e/c, the ratio of the electron velocity in the first Bohr orbital to the vacuum speed of light. Referring to the related physical effect, this constant was named the fine structure constant α. Even in a full quantum mechanical framework, this approximation is still valid for hydrogen-like systems, meaning one electron around a nucleus with charge Z. The energy E_{n} for the n-th orbital in such a system is given by

$$E_{\mathrm{Bohr,n}} = -\frac{(Z\alpha)^2 m_{\mathrm{e}} c^2}{2n^2} \tag{1.2}$$

$$E_{\mathrm{nj}} = E_{\mathrm{Bohr,n}} \left[1 + \frac{(Z\alpha)^2}{n^2} \left(\frac{n}{j+\frac{1}{2}} - \frac{3}{4} \right) \right] \tag{1.3}$$

accounting for the Coulomb interaction between electron and nucleus, and first order relativistic effects. The electron angular momentum l in Sommerfeld's original formula is replaced here by j, the total angular momentum additionally accounting for the electron spin.

The impact of α on astrophysics

As for all fundamental constants, the value of α does not arise from the Standard Model but has to be measured. Currently, this value amounts to $\alpha^{-1} = 137.035\,999\,084(51)$ [4] and is determined by a combination of measurements of the electron magnetic moment in a Penning trap [5] and quantum-electro-dynamical (QED) calculations [6]. The fact α has this exact value is essential for several characteristics of the universe and consequently also for human life as the following examples point out. Roughly 1 s after the Big Bang (in the ΛCDM model) α leaves its marks in the primordial nucleosynthesis [7, 8]. Before the universe was cold enough for light elements (up to ^{7}Li) to build up, the weak interaction process $n + e^+(\nu_e) \leftrightarrow p + \bar{\nu_e}(e^-)$ kept the proton number N_p and neutron number N_n in thermal equilibrium at a ratio

$$\frac{N_n}{N_p} = e^{-\Delta m\, c^2/k_B T}. \tag{1.4}$$

Through an electromagnetic contribution to the binding energy of neutrons and protons, their mass difference $\Delta m = m_n - m_p$ is proportional to α. At a thermal energy of $k_B T < 0.8\,\text{MeV}$, the weak interaction rates drop below the expansion rate of the universe and become negligible. The thereby temperature independent ratio N_n/N_p determines the material available for the formation of the first elements. The nucleosynthesis is stopped when $k_B T < 0.05\,\text{MeV}$. The tunneling through the Coulomb barriers of nuclei, a process necessary for nuclear fusion, is strongly suppressed at this energy. Since α affects the height of the Coulomb barrier, it affects the stopping point of primordial nucleosynthesis. At this point H accounts for ≈75% and ^{4}He for ≈25% of the matter density.

The prerequisite for the formation of atoms is met 300 000 years ($k_B T < 0.3\,\text{eV}$) later. Hitherto, primordial photons were thermalized with matter by elastic scattering and the recombination of electrons and nuclei was impeded by the constant photon bombardment. But as the universe cools down below the ionization energy of hydrogen, at $k_B T < 13.6\,\text{eV}$, electrons and nuclei start to recombine and exit the scattering processes. Similar to the weak interaction, the electromagnetic interaction freezes out. The now sterile photons represent the first directly observable signal from the Big Bang: the cosmic microwave background (CMB). The point in time and the duration of the freeze out process is governed by the atomic physics of the produced H and ^{4}He [9]. α enters in several of these atomic processes, e.g. scattering cross sections ($\propto \alpha^2$), photoionization cross section ($\propto \alpha^{-1}$), transition energies (see equation 1.2: $\propto \alpha^2$), transition rates ($\propto \alpha^5$), recombination coefficient and ionization coefficient ($\propto \alpha^3$). These effects, among many others, are imprinted upon the CMB as temperature fluctuations still detectable today. Just from these cosmological considerations the value of α can be already extracted on a percent level of accuracy.

The reason for the abundance of heavier elements than ^{3}Li is the nuclear fusion in stars. Without the radiation pressure caused by primordial photons, the freshly neutralized atomic matter begins to clump. If such a cloud becomes big enough to exceed a certain mass limit, called the Jeans mass, it collapses and eventually heats up sufficiently to ignite the nuclear fusion of H. While young stars predominantly burn H to produce ^{4}He, older stars above a certain mass can efficiently produce ^{12}C, ^{14}N, and ^{16}O, major essential for all known life forms. They are formed through the reactions

$$3\ ^4\mathrm{He} \rightarrow {}^{12}\mathrm{C} + 7.3\,\mathrm{MeV} \text{ and} \tag{1.5}$$

$$^{12}\mathrm{C} + {}^4\mathrm{He} \rightarrow {}^{16}\mathrm{O} + 7.2\,\mathrm{MeV}. \tag{1.6}$$

These processes would be far too slow to account for the observed abundance of these elements if there was not a nuclear excited state in ^{12}C about 300 keV above the released energy in reaction 1.5 that amplifies its rate drastically, as predicted in [10]. The energy of this excited state depends on the binding energy of the ^{12}C nucleus including an α-dependent Coulomb contribution. Calculations performed in [11] underline the crucial importance of the tuning of α in this process: If its value deviated outside of a window of 4% a factor of 30-1000 either less carbon or less oxygen would be produced.

A possible variation of α

The chronological examples listed above represent only a small selection but emphasize the huge variety of fields and effects α has an impact on. Consequently, the question arises why α seems so perfectly tuned to allow for life to evolve, also referred to as the fine tuning problem. This problem applies to many other fundamental constants of the Standard Model as well, in which the origin of constants lacks an explanation. One solution was probably first brought into the discussion by Dirac [12]. If constants varied, too slowly though to notice in everyday life, they would not require this tuning but life would just happen to exist at a time and in a place where the conditions match. Dirac argued from an aesthetic point of view that dimensionless ratios between atomic and cosmological quantities yield very large numbers that should not appear in nature. Since many of these ratios are in the same order of magnitude, he concluded that combinations of these numbers that cancel in magnitude are meaningful numbers rather than mere coincidences [12, 13]. For example, the age of the universe measured in atomic units of time and the ratio between the gravitational and the Coulomb forces between proton and electron are

on the same order of magnitude

$$14 \times 10^9 \text{yrs} \frac{e^2}{4\pi\epsilon_0 \, m_\text{e} c^3} \approx \frac{e^2}{4\pi\epsilon_0 \, G m_\text{p} m_\text{e}} \approx 10^{40} \tag{1.7}$$

For this relation to be harmonized at all times, it is required that the gravitational constant $G \propto t^{-1}$. Later, Gamow pointed out that a variation of G is ruled out by observations but proposed that α, contained in equation 1.7, might vary instead [14]. In the same paper, he even proposed to search for an α variation in absorption spectra of distant quasars, an idea that has been realized as expanded upon below.

A variety of theories allow for or even require a variation of constants [8]. Extra dimensional theories as Kaluza-Klein models or string theories induce the variation of fundamental constants by higher dimensional metrics or as expectation values of dynamical fields. In another class of theories, fundamental constants couple to a time dependent scalar field, often linked to other mysterious features of cosmological models such as dark energy. Hence, a variation of α would not only disprove the otherwise robust Standard Model but would also give access to alternative theories that have so far been untested since their effects were predicted to be unmeasurably small.

Recently, this field has been attracting special attention as new astrophysical observations of quasar-absorption systems provide evidence that α might vary spatially over large distances [15, 16]. Quasars emit light of a broad spectral range. This light is absorbed at discrete wavelengths by atoms, ions, and molecules while passing interstellar clouds. Depending on the velocities of these absorbing clouds relative to the earth, and therefore their distance through Hubble's law, the produced absorption spectra are redshifted compared to reference spectra of the same elements measured on earth. Hence, the distance of the absorber can be determined through the redshift of its absorption spectrum.

While the velocities of absorbers cause a common energy shift to the spectra, a change of α would modify transition energies individually. This can be seen in equation 1.3: The sensitivity of a transition energy on a variation of α depends on the difference in relativistic contributions of the involved energy levels. This sensitivity can be quantified by the enhancement factor q in

$$\omega \approx \omega_0 + 2q \frac{\Delta\alpha}{\alpha}, \tag{1.8}$$

where ω_0 is the transition frequency in an atom or ion. If there was a deviation $\Delta\alpha$ at a certain redshift from the value of α on earth the same transition would be shifted to a frequency ω proportionally to q. While systematic effects, which could essentially mimic an $\Delta\alpha$, can be estimated by spectral lines with $q \approx 0$, positive or negative shifters ($q \gg 0$ or $q \ll 0$) can be used to extract the value of $\Delta\alpha/\alpha$ (see figure 1.2). First evidence (at 3σ confidence) of an α variation has been reported in [17], when spectral lines of 30 absorbers

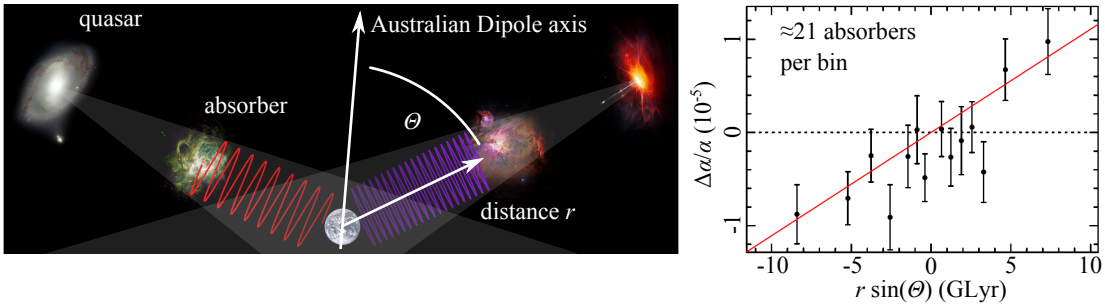

Figure 1.2: Illustration of the Australian Dipole and the observed data, taken from [15]. Light emitted by quasars can be absorbed at discrete wavelengths by interstellar clouds. Even if, as in this example, the same transition is responsible for a certain absorption line, it can still be shifted depending on the projection of the distance r of the cloud on an empirically found dipole axis.

were analyzed at redshifts of $0.5 < z < 1.6$ with the Keck telescope in Hawaii. In the following years more absorption spectra have been added, also from the VLT in Chile and therefore the northern as well as the southern hemisphere is covered. In total, 141 absorbers observed with Keck were combined with 154 absorbers from VLT and several transitions in 14 ion species were considered ranging from redshifts of $0.4 < z < 3.6$. The data favors a dipole-like gradient in the value of α. It is growing by $1.1(0.25)\times10^{-6}\,\mathrm{GLyr}^{-1}$ in one direction along the dipole axis and decreases towards the opposite direction (see firure 1.2). Although this effect is significant at a level of $4.2\,\sigma$, the complex data analysis could be susceptible to unknown systematic errors. Due to the far-reaching nature of this result a vivid discussion has developed. Two recent tests of quasar absorption spectra using the same methods agree with a constant α but show no significant deviation from the expected dipole value either [18, 19]. This extraordinary claim still needs extraordinary proof.

Laboratory tests on an α variation

Complementary to testing the variation of α on very large cosmological scales, highly precise tests can be performed on earth, using extremely accurate atomic clocks. Because the earth, the solar system, and the galaxy move in a hypothetical α-dipole field, the spatial variation changes into a temporal variation on earth. As calculated in [20], a temporal variation of $\dot{\alpha}/\alpha = 1.35 \times 10^{-18}\,\mathrm{y}^{-1}\sin\psi$ is the consequence of the sun's movement with an angle ψ relative to the dipole axis. Unfortunately, this movement is directed almost in parallel to the dipole axis so that $\sin\psi = 0.07(0.1)$ and thus the variation of α amounts to $\approx 10^{-19}\,\mathrm{y}^{-1}$. This constant change is modulated with the earth's annual motion around the sun with an amplitude of 1.4×10^{-20}.

One already implemented method to perform a laboratory test is the comparison of two frequency standards. Thus far, the most accurate frequency standard is based on light absorbed by atoms during electronic transitions. This light in the optical regime is figuratively the pendulum or balance wheel of an atomic clock but oscillates 10^{15} times faster, therefore, providing a much finer scale to measure time. Simultaneously it ticks perfectly periodically, resulting in a narrow frequency width. Up to now, atomic clocks are restricted to the optical regime since the frequency standard transition has to be driven by an optical laser which is locked to the standard, similar to the escapement in a classical clock. The narrow bandwidth lasers needed for that application are so far only available at wavelengths up to 200 nm. A major advantage of atomic clocks is their low susceptibility to their surrounding. Atoms are naturally very compact systems that show little response to atmospheric perturbations and, additionally, new experimental methods have been developed to store isolated single ions or small ensembles at rest in space, and cool them down to few mK.

In laboratory tests of an α variation, two such atomic clocks are compared. As they are are based on atomic transitions, their frequency standards generally depend on α proportionally to the factor q introduced in equation 1.8. It is advantageous to choose transitions that have largely different q-factors. A variation of α can be detected by a variation of the frequency ratio of the clocks. Such experiments have been performed by measuring a transition in $^{171}Yb^+$ against two cesium fountain clocks [21], by comparing two different transitions in $^{171}Yb^+$ [22], and by comparing an Al^+ ion clock to a Hg^+ ion clock [23]. The most stringent constraint is contributed by the Al^+/Hg^+ clock comparison at a level of $-1.6(2.3) \times 10^{-17}\,y^{-1}$ and still a factor of 100 too large to test the astrophysical claim as described above. There are two possibilities to meet this factor of 100 improvement: On the one hand the clocks' accuracy can be improved and on the other hand frequency standards with a higher sensitivity to an α variation, represented by the q-value, can be used.

One promising way to achieve this goal is the use of highly charged ions (HCI) as frequency standards instead of atoms or singly charged ions as discussed in more detail in the theory chapter 2 of this thesis. A large variety of theoretical publications [24–34] revolve around particular transitions in HCI that work as frequency standards with an improved accuracy of more than one order of magnitude compared to atoms and singly charged ions. Many of these transitions are also ten times more sensitive to an α variation. But despite these advantages, the vast majority of these HCI are yet experimentally unexplored. One reason is that the ionization potential increases qualitatively quadratically with the ion's charge state (see equation 1.2). The ionization energy typically amounts from few 100 eV up to several 100 keV which impedes the production for experimental investigation. More-

over, a large recombination cross section quickly causes them to neutralize by collisions with surrounding gas atoms.

A second reason for the lack of experimental data on HCI might originate from the challenges that theory faces for these complicated systems. The strong relativistic contributions impede a perturbative treatment of HCI while, simultaneously, many of the proposed HCI have open shells populated with multiple, strongly coupled electrons. A prime example for this class of HCI is Nd-like Ir^{17+}. It features optical transitions with the highest sensitivity to an α variation ever predicted for a stable atomic system [25]. Transitions in other Nd-like ions have been found to be suitable for frequency standards below 10^{-19} relative accuracy [30]. However, the open and quasi-degenerate $4f$ and $5s$ shells form a $4f^{13}5s^1$ ground state configuration above 56 closed shell electrons. Even for the most advanced atomic structure codes, uncertainties on these transition energies exceeding a 10% level are common. Searching a sub-Hz linewidth highly forbidden transition with a narrow-band spectroscopy laser in a window tens of THz, as it is necessary for clock applications, would prove a fruitless endeavor. First, the spectra of these HCI must be explored experimentally and the uncertainty of their energy levels must be decreased by several orders of magnitude. For this purpose, spectral lines must be identified and assigned to the involved atomic levels. The goal of this thesis is to achieve this first crucial step of measuring and identifying optical transitions in Nd-like HCI around Ir^{17+}.

In the course of this work, HCI were produced, trapped, and investigated in the Heidelberg electron beam ion trap (EBIT) [35]. Neutral atoms injected into the EBIT's vacuum chamber were sequentially ionized by a dense electron beam and trapped by its space charge as well as a set of electrodes. The HCI cloud is located in the center of the EBIT, where the electron beam is focused by the magnetic field of two superconducting coils. A cryogenic environment surrounding the trap center provides a vacuum sufficient to keep the recombination rates below the ionization rates. As a result, HCI are prepared in the desired charge state adjusted by the electron beam energy. The HCI produced in this manner are excited by the electron beam which causes them to emit radiation. This work is focused on the light emitted in the optical regime as mentioned above. The spectra are generated by a Czerny-Turner type spectrometer [36] with optical access to the ion cloud which is imaged onto a charge-coupled device (CCD) chip [37]. The experimental setup and the measurement procedure are explained in chapters 3 and 4.

In chapter 5, acquired spectra of W, Re, Os, Ir, and Pt are presented. Test measurements have been performed on an optical transition in Ti-like Ir to confirm the successful trapping of Ir ions. In order to verify the achievable resolution and accuracy, on a few or even sub-ppm level, a well-known transition in Ar^{13+} has been remeasured [38, 39]. The spectra of Nd-like ions are divided in two parts: Overview spectra, used for example for charge state identification, were taken with a low-resolution high-bandwidth grating.

The most accurate results of selected spectral lines were achieved with a high-resolution grating, allowing to investigate the Zeeman splitting in the strong magnetic field of the EBIT.

The spectra of the Nd-like ions prove to be very rich, containing 30 spectral lines in a range of 370 nm resulting in an average separation of roughly 0.1 eV in case of Ir^{17+}. The uncertainties of calculations being of the same order, a reliable identification by comparing calculated transition energies to the energies of the acquired spectral lines is impossible. Instead, a novel method is demonstrated in chapter 6, which allows to identify magnetic dipole (M1) transitions through their characteristic energy scaling with Z (see equation 1.3) in isoelectronic sequences, as in these in Nd-like ions. An independent test of this method is given by a comparison of the resolved Zeeman splitting in Ir^{17+} and a model using calculated g-factors. Through the M1-scaling identification method, the two proposed clock transitions mentioned above [30] can be derived from the data. In total, 84 hitherto unknown spectral lines in Nd-like W, Re, Os, Ir, and Pt have been categorized of which 47 were identified. Apart from the immediate application in frequency metrology, the acquired data reclaims a small piece of land in the sea of unexplored ion species, as shown in figure 1.3. Chapter 7 concludes the work and discusses further possibilities of spectral line identification. As an outlook, the very recent achievement of Lisa Schmöger and co-workers [40] is introduced to trap HCI in the cryogenic radio frequency trap CryPTEx [41–44] for the first time. In an EBIT, HCI are usually stored at MK temperatures due to the constant electron bombardment, whereas in CryPTEx they can be sympathetically cooled down to tens or hundreds of mK. With that milestone, the way is paved for future applications of quantum logic readout schemes [45] for the here investigated transitions and for the use of HCI as frequency standards.

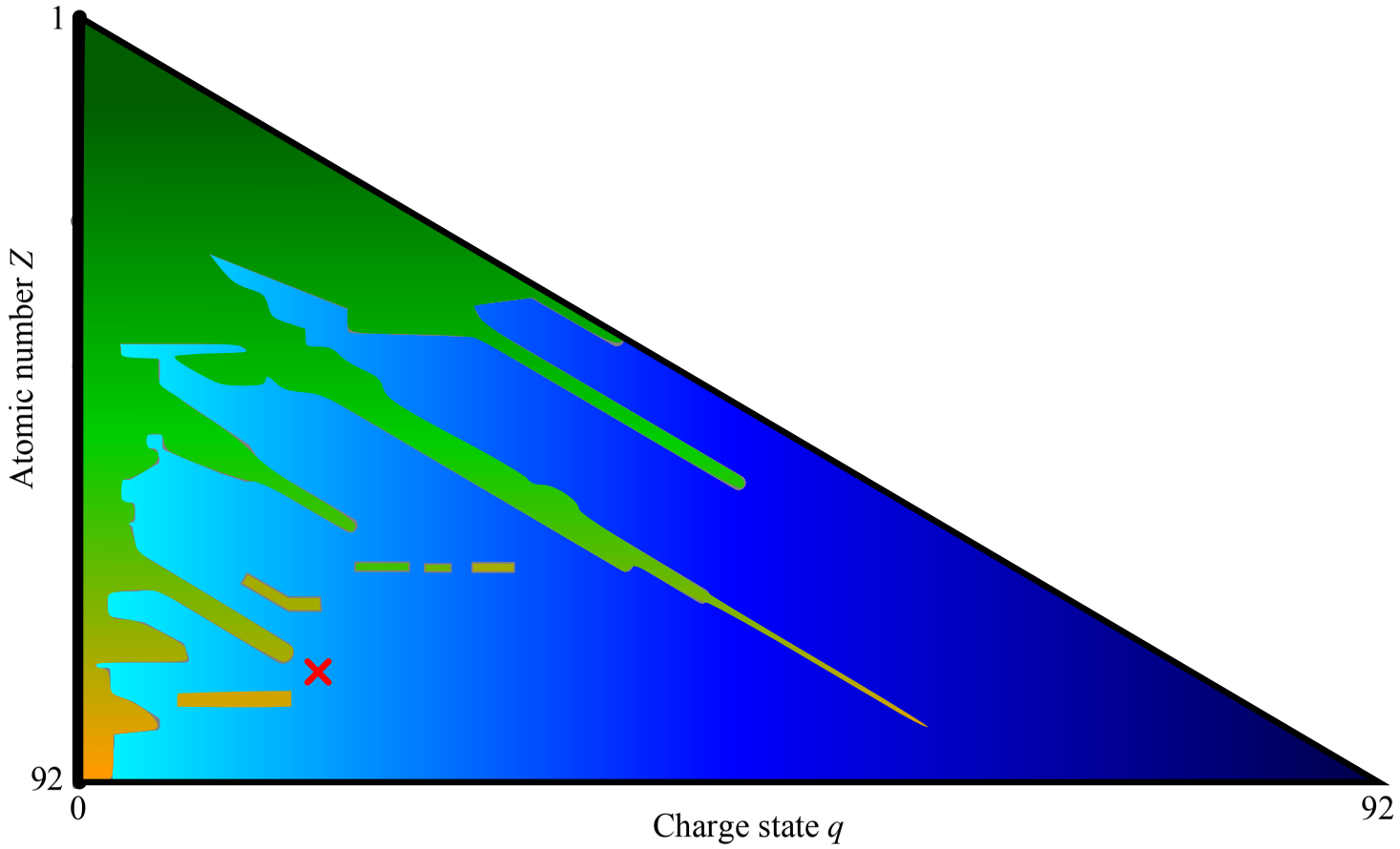

Figure 1.3: The World of atomic physics by [46]. The landmass represents the area of experimentally investigated ion species with atomic number Z and charge state q, following a loose interpretation from [46]. The sea consists of unexplored HCI. The subject of this work is the isoelectronic sequence of Nd around Ir^{17+}, marked by the cross.

Chapter 2

Theory

In this chapter, the theoretical background of the thesis is briefly outlined. Models are introduced that describe the basic concepts of single electron H-like HCI and will be used to motivate the advantages of HCI in the context of a laboratory test of an α variation. In practice, much more complex multi-electron HCI, such as the Nd-like ions discussed below, have to be considered for such a test, for which simple analytical models do not hold. Nevertheless, many characteristics can be qualitatively described by their scaling with the atomic number Z, such as that of transition energy which is exploited for the interpretation of the measured spectra. However, to perform quantitative calculations for the here investigated cases, elaborate atomic structure codes have to be employed as the examples presented below show. Subject of this work are Nd-like HCI near the level-crossing of $4f$ and $5s$ shell, with special emphasis on Ir^{17+}. Section 2.3 deals with the level crossing phenomenon and the consequential unique level structure of Ir^{17+}. As already mentioned, even the here utilized advanced atomic structure codes encounter difficulties predicting level energies accurately in Nd-like systems. The physical processes on which the experimental approach is based are explained in section 2.4.1, including the production of HCI by ionization, the spectroscopic investigation of excitation and radiative decay, as well as the study of resulting spectral line shapes. The last case plays an important role in the identification of transitions by their resolved Zeeman pattern.

2.1 Single electron ions

Hydrogen-like ions, consisting of one electron bound to a nucleus with Z protons, form the simplest atomic systems possible. These systems can be used to exemplify various characteristics of HCI. In particular, the advantages of using HCI for laboratory tests on a possible α variation are discussed with the H-like system as an example. H-like ions are

the only case for which Schrödinger's equation

$$H_{\mathrm{D}}\Psi = E\Psi \tag{2.1}$$

is analytically solvable, where Ψ is the single electron wavefunction describing the quantum state of the H-like ion and E are the energy eigenvalues of the Hamilton operator H_{D}. As relativistic effects are of great importance in HCI, H_{D} represents the relativistic Dirac-Hamiltonian

$$H_{\mathrm{D}} = c\boldsymbol{\alpha}\boldsymbol{p} + \beta m_{\mathrm{e}}c^2 + V_{\mathrm{nuc}}, \tag{2.2}$$

with the vacuum speed of light c, the electron mass m_{e}, the Dirac matrices $\boldsymbol{\alpha}$ and β, and the nuclear Coulomb potential $V_{\mathrm{nuc}} = -\frac{1}{4\pi\epsilon_0}\frac{Ze^2}{r}$ [47]. It is interesting to note that Sommerfeld's bottom-up approach (equation 1.3) is in fact a good approximation of the full solution to equation (2.2).

For the more complex examples below, it is useful to treat them using corrections to the H-like system, by considering single active electrons above closed shells, as in the case of alkaline-like ions. The solutions for equation 2.2 can still be used for a qualitative treatment if the closed shells are treated as an effective screening of the nuclear charge for the active electron. This can be done by replacing Z with the effective charge Z_{eff} in the ionization potential I_{n} (which corresponds to $E_{\mathrm{Bohr,n}}$ in equation 1.2)

$$I_{\mathrm{n}} = -\frac{(Z_{\mathrm{eff}}\alpha)^2 m_{\mathrm{e}}c^2}{2n^2}. \tag{2.3}$$

In this case, $Z_{\mathrm{eff}} \approx Z - n_{\mathrm{e}}$ is the difference between Z and the number of screening electrons n_{e}. Hence, a sufficiently accurate solution is given by

$$E_{\mathrm{nj}} = I_{\mathrm{n}}\left[1 + \frac{(Z\alpha)^2}{n^2}\left(\frac{n}{j+\frac{1}{2}} - \frac{3}{4}\right)\right]. \tag{2.4}$$

The quantum state of the ion is characterized by wavefunctions with main quantum number n, electron orbital momentum $l = 0 \ldots n-1$ (labeled $s(l=0)$, $p(l=1)$, $d(l=2)$, $f(l=3)$, $g(l=4)$, etc.), and electron spin s while the nuclear spin can be neglected. Spin and orbital momenta couple to the total angular momentum $j = l + s$. A full state description given by the relativistic nomenclature, i.e. the electronic configuration followed by ${}^{2s+1}l_j$.

2.1.1 Transition energies

Electrons can perform transitions between the atomic states by absorbing or emitting photons. In the experiments presented in this thesis, the photons emitted from spon-

taneous emission are investigated. These photons carry an energy that corresponds to the energy difference of the involved states which can be extracted from equation 2.4. A higher Z_{eff} causes a stronger nuclear potential and the energy levels are pulled apart. In first order (for $(Z_{\mathrm{eff}}\alpha) \ll 1$), the energy of an atomic state is determined by I_{n}, hence, transition energies between states with different n (inter-configuration transitions) scale with $E(n'-n) \approx I_{\mathrm{n}'-\mathrm{n}} \propto Z_{\mathrm{eff}}^2$. This means that the $n = 2-1$ transition in neutral H ($Z_{\mathrm{eff}} = 1$) moves from 10 eV [48] to the 1.236 keV [49] region for H-like Na ($Z_{\mathrm{eff}} = 10$).

In the relativistic framework given in equation 2.4, this energy is corrected by the fine structure splitting, which removes the degeneracy of states with same n and makes the energy depend on j. Transition energies within a fine structure configuration (intra-configuration transitions) scale with $(Z_{\mathrm{eff}}Z)^2$. In neutral H, fine structure transitions are of the order of 10^{-4} - 10^{-5} eV [50] but quickly shift into the visible range of few eV for heavier elements with higher nuclear charge. Most of the observed transitions in this work are of this type and the fact that they exhibit this simple scaling in powers of Z and Z_{eff} will be used to identify them.

2.1.2 Transition rates

The spontaneous transition rate between the states Ψ' and Ψ is determined by its Einstein coefficient [47]

$$A_{\Psi',\Psi} = \frac{e^2\omega}{2\pi\hbar c}\left|\langle\Psi'|\boldsymbol{\alpha}\boldsymbol{\epsilon}\mathrm{e}^{-\mathrm{i}\boldsymbol{k}\boldsymbol{r}}|\Psi\rangle\right|^2, \tag{2.5}$$

with the transition frequency of the emitted photon $h\omega = E_{\Psi'} - E_{\Psi}$, and the photon polarization $\boldsymbol{\epsilon}$ and momentum $\boldsymbol{k}$. The transition matrix element $\langle\Psi'|\boldsymbol{\alpha}\boldsymbol{\epsilon}\mathrm{e}^{-\mathrm{i}\boldsymbol{k}\boldsymbol{r}}|\Psi'\rangle$ and its transition operator can be expanded in multipole operators. In the simplest case, it takes the form of an electric dipole operator, hence, allowing for electric dipole, or E1 type, transitions. The next higher orders are the magnetic dipole M1, the electric quadrupole E2, and so on, up to orders Mκ and Eκ. With increasing multipole orders, the matrix elements are suppressed for optical transitions by factors of order $\alpha^{2\kappa-2}$ for Eκ transitions and $\alpha^{2\kappa}$ for Mκ transitions. In addition to energy conservation, which holds for all κ, there are selection rules determining the main transition channel [47]

$$\Delta j = 0, \pm 1, .., \pm\kappa, \tag{2.6}$$

$$\Delta m = 0, \pm 1, .., \pm\kappa, \tag{2.7}$$

$$\Delta P = \begin{cases} (-1)^{\kappa} & \text{for E}\kappa \text{ transitions} \\ (-1)^{\kappa+1} & \text{for M}\kappa \text{ transitions} \end{cases}, \tag{2.8}$$

covering the conservation of angular momentum for j and its projection, the magnetic quantum number m. P is the parity, describing the symmetry of the wavefunction under

inversion of all spatial dimension ($r \to -r : \Psi \to P\Psi$). Except for the multiplicity of a transition, its rate is also strongly influenced by the overlap of the wavefunctions through $\langle \Psi' | \boldsymbol{\alpha} \boldsymbol{\epsilon} \mathrm{e}^{-\mathrm{i}\boldsymbol{kr}} | \Psi \rangle$.

Frequency standard transitions need to be highly forbidden, of E2/M2 type or higher multipoles, since the natural line width (see section 2.4.3) is inversely proportional to $A_{\Psi',\Psi}$ and a narrow line width allows for an accurate determination of its center frequency. The Al^+ clock, which is the most accurate ion clock so far, is locked to an 8 mHz wide transition, i.e. a transition emitting one photon every two minutes. For this thesis, the main focus lies on E1 and M1 transitions, meaning $\Delta j = 0, \pm 1$, $\Delta m = 0, \pm 1$, and a parity change for E1 transitions, as their rates direct observation in an EBIT is possible. Nevertheless, higher order multipole transitions that are not directly detectable can be inferred by the exact knowledge of the level structure. By these means, E2 transitions in Hf^{12+} and W^{14+} could be determined (see section 6.1), which were predicted to be particularly suitable as frequency standards [30].

2.1.3 Stark effect

For a high accuracy clock it is not sufficient to be locked to an optical and highly forbidden, thus narrow, transition. Without going into the details of the working principles of atomic clocks (for further information see, e.g., [51]), an optical frequency standard needs to be extremely stable and unaffected by its experimental surrounding, which includes influences from all kinds of external fields, as cooling lasers, spectroscopy lasers, trapping fields, and the blackbody radiation background. The use of transitions in HCI are beneficial for this cause, as explained below.

While increasing Z_{eff}, V_{nuc} causes a stronger attractive force acting on the electron at a constant distance r. A straightforward effect of this scaling is that the electron is pulled closer towards the nucleus. Its expected distance to the nucleus is $r \propto Z_{\mathrm{eff}}^{-1}$, thus the ion compacts with increasing charge. This opens up interesting possibilities to test fundamental quantum theory since a considerable part of the electronic wavefunction is located within the nucleus and the strong fields acting at such a close distance strongly enhance quantum electrodynamical effects [52]. The main aspect for applications in metrology, which is the focus of this work, is the result of a reduced polarizability of the electron cloud in HCI. The above-mentioned fields impose an energy shift on the levels involved in the clock transition resulting in a frequency uncertainty of the clock, and are therefore undesirable. The energy shift ΔE caused by electric fields F can be described by the Stark effect. In first order pertubation theory $\Delta E^{(1)}$ is given by [47]

$$\Delta E_{\mathrm{a}}^{(1)} = F \langle \Psi_{\mathrm{a}} | D | \Psi_{\mathrm{a}} \rangle \,. \tag{2.9}$$

$\langle \Psi_\mathrm{a}|D|\Psi_\mathrm{a}\rangle$ represents a dipole matrix element for states with a set of quantum numbers a. The dipole operator $D = e\,r$ (if the dipole z-axis is in parallel to the electric field) can be interpreted as a displacement r between the nucleus and the active electron which is proportional to Z_eff^{-1}.

Equation 2.9 is only valid for angular momentum degenerate states a, i.e. disregarding the fine structure. This means that this picture can only be applied if the energy splitting by the external field is much larger than the fine structure splitting, which is not the case in the discussed clock experiments. Moreover, $\Delta E^{(1)}$ becomes zero for fields that have vanishing time averages, such as laser fields. A more applicable treatment is the quadratic Stark shift, following from second order pertubation theory [47]

$$\Delta E_\mathrm{a}^{(2)} = F^2 \sum_{k\neq a} \frac{|\,\langle \Psi_\mathrm{a}|D|\Psi_\mathrm{k}\rangle\,|^2}{E_\mathrm{a} - E_\mathrm{k}}, \tag{2.10}$$

with the unperturbed energies $E_\mathrm{a,k}$. Uncertainties arising from this shift have to be considered in most atomic clocks [51]. As $|\,\langle \Psi_\mathrm{a}|D|\Psi_\mathrm{k}\rangle\,|^2 \propto Z_\mathrm{eff}^{-2}$ and $E_\mathrm{a} - E_\mathrm{k} \propto Z_\mathrm{eff}^2$, this effect scales even more favorably for higher charge states than the linear Stark effect. For $j > 1/2$, ions can have higher multipole momenta, for example a quadrupole moment. However, in the naive picture used here, the quadrupole operator is of dimension $r^2 \propto Z_\mathrm{eff}^{-2}$ and should therefore be reduced as well for HCI.

Several proposals have been made to use transitions in HCI as frequency standards [24–34, 53]. By calculating the actual error budgets, it has been found that these transitions are extremely stable, down to level of 10^{-19} s such as in the above mentioned Hf^{12+} and W^{14+} ions which means than an order of magnitude improvement compared to state of the art clocks [54, 55]. At this level accuracy, the gravitational redshift will cause a measurable effect if the height of the experiment is changed by 1 mm [30].

2.1.4 Sensitivity on the fine structure constant

Apart from the features that are advantageous for improving the accuracy of optical clocks, HCI additionally have a strongly enhanced sensitivity to a possible α variation. Using the simple expression given in equation (2.4), the enhancement factor q introduced in equation (1.8) becomes

$$q \approx I_\mathrm{n} \frac{Z\alpha}{n(j+1/2)}, \tag{2.11}$$

the relativistic fine structure correction [24]. Consequently, q experiences the same scaling as fine structure transitions $(ZZ_\mathrm{eff})^2$, meaning that heavy HCI have generally enhanced sensitivities to an α variation. For a laboratory test, a large q-factor is not sufficient. Since transitions between electronic states are probed in the experiment, a large difference Δq

for the involved states is desirable. Within one fine structure configuration with the same n, q-factors are rather similar. Therefore, for an optimized sensitivity, states in different configurations have to be investigated. As stated above, it can be difficult to find optical inter-configuration transitions in HCI, as they generally tend to be at keV energies.

An elaborate analysis of q-factors has been carried out in several publications (e.g. [24, 25, 27]) and, indeed, many HCI show strong relativistic contributions and thus large q-factors. In order to find inter-configuration transitions in the optical range for these ions, the phenomenon of Coulomb degeneracy of multiple configurations was exploited. Because the energy of configurations scales differently with Z, a mutual cancellation of different energy terms can appear, and the resulting inter-configuration transitions can shift into the optical range. Level-crossing effects are explained in more detail in section 2.3. The level-crossing system with the highest sensitivity of all stable ions, and subject of this thesis, is Nd-like Ir with a $\Delta q \approx 750\,000\,\mathrm{cm}^{-1}$ [25]. Compared to the most sensitive former experiment, measuring the frequency ration between an Al^+ and a Hg^+ ion clock [23] with $\Delta q \approx 57\,000\,\mathrm{cm}^{-1}$ [25], this means more than an order of magnitude improvement in sensitivity.

Level-crossings are usually predicted for complex and heavy HCI with many electrons, such as Nd-like Ir. The models discussed above give only a qualitative overview but for a precise analysis of these systems sophisticated atomic structure codes have to be employed that account for the strong correlations between electrons. For the identification of observed transitions, several advanced methods have been employed in this work.

2.2 Multi-electron ions

The straightforward way to understand an experimental spectrum would be to predict the transition energies of the desired ion theoretically and then assign them to the closest observed spectral lines. Unfortunately, theory is not accurate enough, or, respectively, the spectral density is too high to allow for unambiguous identification in this way, as will be shown in Chapter 4. Nevertheless, it is essential to have at least an schematic knowledge of the level structure of the investigated ion species. In the present case, these are Nd-like W, Re, Os, Ir, and Pt ions. The Nd-like isoelectronic sequence contains 60 bound electrons, 14 of which are located in open sub-shells, implying strong electron correlations. To tackle these problematic cases, two classes of atomic structure codes have been in use most successfully: the coupled cluster (CC) method [56–58] (calculations by A. Borschevsky [59]), and the configuration interaction (CI) method [60, 61] (calculations by N. Oreshkina [62]). Additionally, calculations have been performed in the course of this work using the Flexible Atomic Code (FAC) [63], which also belongs to the class of CI methods.

To account for the electron correlations, the Hamiltonian from equation (2.2) has to be extended. In an N-electron ion each electron i is represented by a single electron operator $H_{\mathrm{D,i}}$. The Coulomb-Breit-Hamiltonian $H_{\mathrm{CB,ij}}$ additionally accounts for the potentials arising from interelectronic interactions between the electrons i and j at a distance r_{ij}, including the non-relativistic Coulomb-interaction as well as relativistic angular momentum coupling. The resulting Hamiltonian

$$H = \sum_{i=1}^{N} H_{\mathrm{D,i}} + \frac{1}{2} \sum_{i \neq j} H_{\mathrm{CB,ij}}, \tag{2.12}$$

with

$$H_{\mathrm{CB,ij}} = \alpha \left(\frac{1}{r_{\mathrm{ij}}} - \frac{\boldsymbol{\alpha_{\mathrm{i}}} \boldsymbol{\alpha_{\mathrm{j}}}}{r_{\mathrm{ij}}} - \frac{(\boldsymbol{\alpha_{\mathrm{i}}} \boldsymbol{r_{\mathrm{ij}}})(\boldsymbol{\alpha_{\mathrm{j}}} \boldsymbol{r_{\mathrm{ij}}})}{2 r_{\mathrm{ij}}^3} \right), \tag{2.13}$$

is applied for both methods.

2.2.1 The configuration interaction method

The configuration interaction method starts with the Hamiltonian of equation (2.12). A trial wavefunction Ψ is constructed from a set of one-electron basis functions a_i. The total wavefunction has to be anti-symmetric to account for the Pauli principle. It can be represented in terms of Slater determinants, for example. By adding up the single-electron angular momenta j_{i} and magnetic quantum numbers m_{i}, the configuration state function [64]

$$\phi_{\gamma \mathrm{JM}} = \sum_{m_{\mathrm{i}}} |a_1, a_2, .., a_{\mathrm{N}}\rangle \, \langle j_1 m_1, j_2 m_2, .., j_{\mathrm{N}} m_{\mathrm{N}} | \gamma J M \rangle \tag{2.14}$$

can be composed with γ being a set of quantum numbers representing the a_{i}, and J,M being the ion's total angular momentum quantum number and the corresponding magnetic quantum number. Single electron configurations ϕ are used to assemble the trial wave function

$$\Psi_{\mathrm{JM}} = \sum_{i} c_{\mathrm{i}} \phi_{\mathrm{i}}, \tag{2.15}$$

with the coefficients $\mathrm{c_i}$. Most systems are too complex for a full expansion into all possible configurations of electrons, since the size of the basis grows with N^K, with K being the maximum degree of single electron excitations (number of single-electron states above the ground state). A systematic way of truncating the series is the expansion into all possible single, double, and triple electron excitations, etc. up to a limit set by the quantum

numbers K_1, K_2, and K_3, respectively, etc.:

$$\Psi = \phi_0 + \sum_{l}^{K_1} c_{\mathrm{l}}^{\mathrm{single}} \phi_{\mathrm{l}} + \sum_{l,l'}^{K_2} c_{\mathrm{l,l'}}^{\mathrm{double}} \phi_{\mathrm{l,l'}} + \sum_{l,l',l''}^{K_3} c_{\mathrm{l,l',l''}}^{\mathrm{triple}} \phi_{\mathrm{l,l',l''}} \ldots \quad . \tag{2.16}$$

Equivalently, this expansion can be expressed by excitation operators C_{p} ($p = 1$ single excitations, $p = 2$ double excitations, etc.) acting on ϕ_0 to generate the excited states [65]

$$\Psi = \left(1 + \sum_{p} C_{\mathrm{p}}\right) \phi_0. \tag{2.17}$$

The energy eigenvalues E from the Schrödinger equation 2.1 can now be calculated by

$$E = \langle \Psi | H | \Psi \rangle = \langle \phi_0 | H | \phi_0 \rangle + \sum_{l,m} c_{\mathrm{l}}^{\mathrm{single}} c_{\mathrm{m}}^{\mathrm{single}} \langle \phi_{\mathrm{l}} | H | \phi_{\mathrm{m}} \rangle \ldots, \tag{2.18}$$

with the normalization condition $\langle \phi_0 | \Psi \rangle = 1$. By varying the c coefficients, equation (2.18) can be minimized to yield the proper energy eigenvalues. At this point, the trial function Ψ corresponds to an approximation of the real atomic wavefunction, which is an approximate eigenstate of H.

More explicitly, the method used by N. Orseshkina and co-workers for the calculations used for comparison in this work is the configuration interaction Dirac-Fock Stormian (CIDFS) method, which is described in detail in [60, 61]. The single-electron wavefunctions were considered up to single-excitations of $7s$, $7p$, $7d$, and $7f$ as well as double-excitations up to $5p$ states. For this size of basis, the calculation for a single Nd-like ion took more than a month to be completed on a single cluster node with the serial CIDFS code available. Unfortunately, the calculation did not yet show a convergent behavior of the level energies with respect to the size of the basis set. The resulting accuracy could be improved by parallelizing the code and hence taking the opportunity to use a longer basis, including triple excitations as well. The theoretical uncertainty was estimated at a 1% level for the fine structure splitting, which is similar to what is expected from other methods, the absolute energy uncertainty at 1 eV.

For the FAC calculations, single-excitations up to $5p$, $5d$, $5f$ and double excitations up to $5d$ were included. The addition of configurations changed the energy of the fine structure splitting only on a percent level. The calculations were optimized to treat the whole isoelectronic sequence with the same quality in a reasonable time and with the main focus on the fine structure splitting. One ion could be calculated on roughly one day using a single node. Adding more configurations did not only increase the calculation time but also the memory consumption above the cluster's capacities. These calculations did not

converge and were not expected to have a quality comparable to the CIDFS calculations although fine structure splittings were very stable over many different bases.

2.2.2 The coupled cluster method

The coupled cluster approach originates from nuclear physics [66] and is widely used in quantum chemistry today [65]. The CI and CC methods work with similar principles. The difference is the generation of the model functions ϕ. Instead of using the multiple excitation operators C_p (see equation 2.17), the cluster operator T is used in the form [65]

$$\Psi_\mathrm{JM} = \mathrm{e}^T \phi_0 = \left(1 + T + \frac{T^2}{2} + \frac{T^3}{3!} + \ldots\right) \phi_0. \tag{2.19}$$

In equivalent to C, T can be decomposed into p-electron excitations

$$T = T_1 + T_2 + T_3 + \ldots + T_\mathrm{p}. \tag{2.20}$$

The series (2.20) needs to be truncated, as for example for double excitations T_2. Thereby, the expansion in equation (2.19) takes the form

$$\mathrm{e}^T = 1 + T_1 + T_2 + \frac{1}{2}T_1^2 + T_1 T_2 + \frac{1}{2}T_2^2 + \ldots \ . \tag{2.21}$$

An advantage of the CC method can be illustrated by comparison with the excitation operators C used in the CI method [65]:

$$C_1 = T_1, \tag{2.22}$$

$$C_2 = T_2 + \frac{1}{2}T_1^2, \tag{2.23}$$

$$C_3 = T_3 + T_1 T_2 + \frac{1}{3}T_1^3, \tag{2.24}$$

$$C_4 = T_4 + \frac{1}{2}T_2^2 + T_1 T_3 + \frac{1}{2}T_1^2 T_2 + \frac{1}{4}T_1^4, \tag{2.25}$$

$$\vdots$$

As shown for instance in equation (2.25), terms as T_2^2 and T_1^4 are effective quadruple excitations. By that, the series (2.21) in principle contains all orders of correlations (although $p \leq 2$) but because of its fast convergent behavior, it is naturally truncated after a finite number of terms. This makes CC methods particularly suitable for treating highly correlated electron systems. The energy can again be obtained by the expectation value

$$E = \langle \phi_0 | \mathrm{e}^T H \mathrm{e}^{-T} | \phi_0 \rangle = \langle \phi_0 | \bar{H} | \phi_0 \rangle \,. \tag{2.26}$$

For the relativistic Fock space coupled cluster (FSCC) calculations presented below [56, 57], performed by A. Borschevsky, single and double excitations were considered (T_1 and T_2). The model wavefunctions ϕ_0 were first obtained from an effective Hamiltonian for the closed shell systems W^{12+}, Re^{13+}, Os^{14+}, Ir^{15+}, Pt^{16+}. Subsequently, two electrons are removed to generate the Nd-like ions, and a new effective Hamiltonian is iteratively found in a self-consistent way to yield approximated energy eigenvalues applying equation 2.26. In this case, convergence could be reached with respect to the size of the basis set.

A list of the results of these calculations can be found in table 2.1. In addition to the described calculations, COWAN-code calculations (a Hartree-Fock code including relativistic corrections [67]) were performed by U. I. Safronova and CI-type calculations from [25] are shown. There are large differences between the calculations, as become obvious from table 2.1.

2.3 The $4f$-$5s$ level crossing in Nd-like ions

The results of the FSCC calculations for Nd-like W, Re, Os, Ir, and Pt are listed in table 2.2 and are depicted as a Grotrian diagram in figure 2.1 and 2.2. The atomic

Table 2.1: Calculated level structure of Ir^{17+} performed with multireference Fock space coupled cluster (FSCC) method, configuration-interaction-Dirac-Fock-Sturmian (CIDFS) method, the COWAN code, Flexible Atomic Code (FAC) [63], and configuration interaction (CI) method. Energies are given in eV.

configuration	level	FSCC [59]	CIDFS [62]	COWAN [68]	FAC	CI [25]
$4f^{13}5s^1$	$^3F_4^o$	0	0	0	0	0
	$^3F_3^o$	0.578	0.604	0.525	0.599	0.600
	$^3F_2^o$	3.119	3.105	3.246	3.180	3.257
	$^1F_3^o$	3.744	3.788	3.796	3.821	3.905
$4f^{14}$	$^1S_0$	1.686	0.871	0.700	7.396	0.627
$4f^{12}5s^2$	$^3H_6$	3.003	3.641	4.215	8.843	4.375
	$^3F_4$	4.159	4.748	5.249	10.043	5.606
	$^3H_5$	5.912	6.530	7.241	11.912	7.405
	$^3F_2$	6.820	7.479	7.911	12.930	8.498
	$^1G_4$	6.970	7.556	8.237	13.007	8.541
	$^3F_3$	7.291	7.916	8.558	13.418	8.917
	$^3H_4$	9.737	10.285	11.109	15.870	11.434
	$^1D_2$	10.219	10.943	11.391	16.558	12.159
	$^1J_6$	11.638	12.627	12.605	17.820	13.646
	$^3P_0$	11.656	12.351	12.540	18.050	13.727
	$^3P_1$	12.326	13.141	13.382	18.832	14.428
	$^3P_2$	13.327	14.044	–	19.830	–
	$^1S_0$	21.684	23.031	–	28.220	–

structure of the investigated ions shows several remarkable features, which will be discussed in the following. $4f^{12}5s^2$, $4f^{13}5s^1$, and the $4f^{14}$ configurations are the lowest energy configurations in these ions. The $4f^{12}5s^2$ and $4f^{13}5s^1$ configurations exhibit a rich fine structure, while the $4f^{14}$ configuration forms a $^1S_0$ state and thus has no fine structure splitting. There is a dense quasi-continuum of higher energy states that can be observed in the vacuum ultra violet (VUV) spectra but only the three lowest energy configurations significantly produce optical transitions. Within the configurations, level energies scale smoothly and slowly with Z as expected. The energy separation between configurations, in contrast, changes by approximately $10\,\mathrm{eV}/Z$, as the slopes differ for each configuration.

The combination of these effects leads to the level crossing in Ir^{17+}, as predicted in [25]. Such level crossings take place as orbitals of different angular momentum change their energy ordering from the Coulomb ordering, dominated by the electro-static nuclear potential, to the Madelung ordering, where the angular momentum coupling between electrons becomes dominant. This process is illustrated in figure 2.3. For the Coulomb ordering the atomic states are firstly ordered by their main quantum numbers n and secondly by the angular momentum l. For for many electron systems, the Madelung ordering dictates that orbitals with lower $n + l$ are occupied first. Starting from the Madelung-ordering in the neutral Ir atom, the influence of the nuclear potential increases as more and more electrons are removed. Approaching the H-like ion, the electron correlation effects become insignificant. Somewhere in between these cases, a transition between the two orderings has to occur, such as in Ir^{17+} where the $4f$ and the $5s$ orbitals cross. In the vicinity of the crossing, these orbitals are almost degenerate, and optical transitions between them are possible. A crossing between the $4f$ and $5s$ orbitals is particularly interesting with regard to an α variation, since their q-factors are markedly different due to a large difference in angular momentum.

2.3.1 Sensitivity on an α variation in Ir^{17+}

The above mentioned high sensitivity to an α variation in Ir^{17+} is due to a combination of effects. First, as explained in section 2.1.4, its atomic number of $Z = 70$ and a relatively high charge state generate the needed strong relativistic contributions. This effect is even enhanced because of the fact that Ir^{17+} has two holes in the otherwise closed shell configuration $4f^{14}5s^2$. Compared to single electrons above closed shells, the screening of the nuclear potential by other electrons is diminished if the active electron is located in an open shell. The transitions taking place in such systems can be viewed as electron hole transitions which increase the scaling from section 2.1.4 to $(ZZ_{\mathrm{eff}}^{3/2})^2$. Atomic structure calculations have been carried out in [25], taking different values of α to study the dependence of the state energies on α. In these studies, q-values for many transitions were

calculated, such as

$$q(4f^{13}5s^1) \approx 10\,000\,\mathrm{cm}^{-1}, \tag{2.27}$$

$$q(4f^{14}) \approx 370\,000\,\mathrm{cm}^{-1}, \tag{2.28}$$

$$q(4f^{12}5s^2) \approx -370\,000\,\mathrm{cm}^{-1}. \tag{2.29}$$

For intra-configuration fine structure transitions Δq would be close to zero. To exploit the high q-values, optical inter-configuration transitions have to be employed which is only possible due to the level crossing, expected to occur in Ir^{17+}.

The level structure of Ir^{17+} is visualized as a Grotrian diagram in figure 2.4. If two clock transitions in Ir^{17+} could be compared, for example between $4f^{14} - 4f^{13}5s^1$ and $4f^{12}5s^2 - 4f^{13}5s^1$, their frequencies would change in opposite directions due to the different signs of q. Such a scheme would thus double the sensitivity. Moreover, to be suitable for a frequency standard, these transitions need to be very narrow and therefore highly forbidden. One particularly sensitive candidate, the $4f^{14}\,{}^1S_0$-$4f^{13}5s^1\,{}^3F_3^o$ E3 transition at a wavelength of 1119 nm (from FSCC), could prove challenging, as the system first needs to be prepared with full population in the $4f^{13}5s^1\,{}^3F_4^o$ state. Moreover, the theoretical uncertainty of transition energy could be on the order of 1 eV (0.7 eV for each state en-

Table 2.2: Calculated level structure of W^{14+}, Re^{15+}, Os^{16+}, Ir^{17+}, and Pt^{18+} performed with a FSCC method [59]. Energies are given in eV.

configuration	level	W^{14+}	Re^{15+}	Os^{16+}	Ir^{17+}	Pt^{18+}
$4f^{13}5s^1$	${}^3F_4^o$	18.441	11.812	4.654	0	6.064
	${}^3F_3^o$	18.957	12.349	5.212	0.578	6.661
	${}^3F_2^o$	20.663	14.310	7.451	3.119	9.529
	${}^1F_3^o$	21.296	14.939	8.077	3.744	10.154
$4f^{14}$	${}^1S_0$	40.882	28.065	13.335	1.686	0
$4f^{12}5s^2$	${}^3H_6$	0	0	0	3.003	17.200
	${}^3F_4$	1.051	1.087	1.122	4.159	18.388
	${}^3H_5$	2.064	2.324	2.605	5.912	20.436
	${}^3F_2$	3.188	3.400	3.610	6.820	21.220
	${}^1G_4$	2.958	3.273	3.609	6.970	21.547
	${}^3F_3$	3.279	3.593	3.929	7.291	21.868
	${}^3H_4$	4.954	5.502	6.095	9.737	24.620
	${}^1D_2$	5.896	6.314	6.754	10.219	24.902
	${}^1J_6$	7.175	7.644	8.130	11.638	26.357
	${}^3P_0$	7.343	7.757	8.134	11.656	26.255
	${}^3P_1$	7.720	8.236	8.770	12.326	27.097
	${}^3P_2$	8.253	8.904	9.593	13.327	28.297
	${}^1S_0$	15.485	16.339	18.106	21.684	36.880

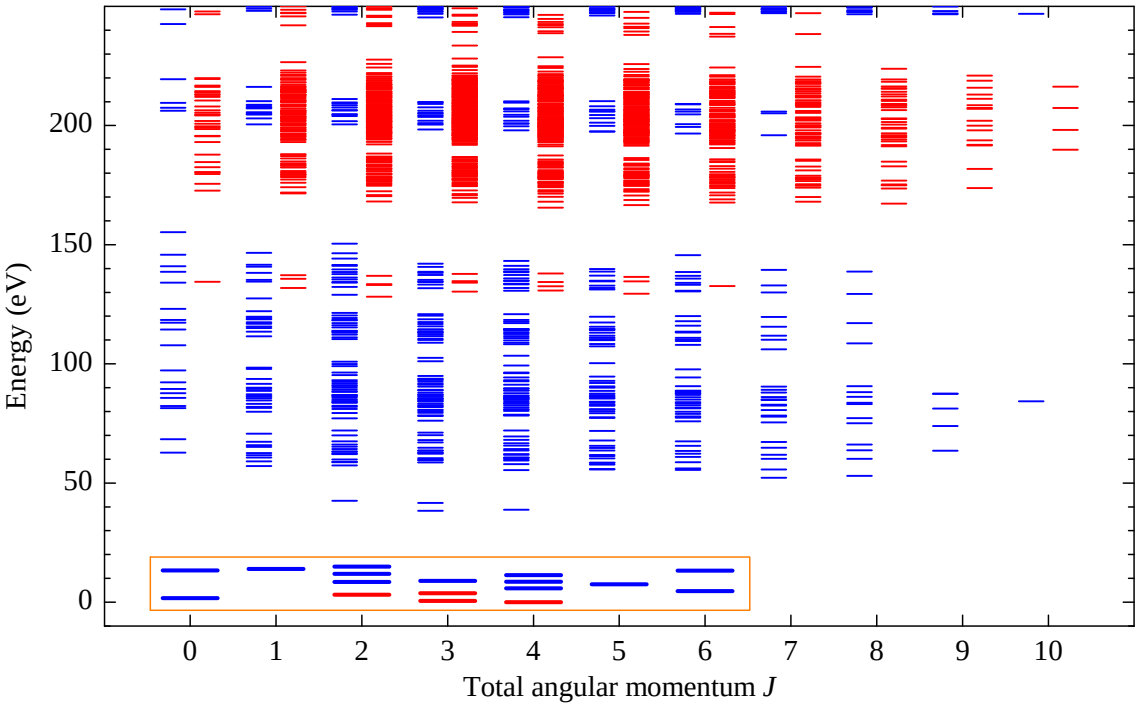

Figure 2.1: Level structure of Ir^{17+} up to an energy of 250 eV, calculated using FAC. Even parity states are depicted in blue, odd parity states in red. The density of states above 50 eV is extremely high. Excited electrons from these states will decay primarily through VUV transitions towards lower energy states. The optical transitions, investigated in this work, take place mainly in the lowest energy configurations marked by the orange box. Magnified versions of this region can be found in the Grotrian diagrams in figures 2.2 and 2.4

ergy [25]), which means that the $4f^{14}\,{}^1S_0$-$4f^{13}5s^1\,{}^3F_3^o$ E3 transition could, in the worst case, be at a wavelength of 12 µm, where high accuracy laser spectroscopy becomes more difficult. A much more promising candidate is the transition $4f^{12}5s^2\,{}^3H_6$-$4f^{13}5s^1\,{}^3F_4^o$ at a wavelength of 413 nm (from FSCC). This transition is of M2-type and can be driven directly from the ground state. The $4f^{12}5s^2\,{}^3H_6$ excited state can decay spontaneously via an E3-channel into the $4f^{13}5s^1\,{}^3F_3^o$ or ${}^1F_3^o$ states. Although this competitive branch could have Einstein coefficients of the same order, the $4f^{13}5s^1\,{}^3F_3^o$ and ${}^1F_3^o$ states would quickly decay back into the ground state via an M1 channel. In that way, the population is not pumped out of the ground state. Nevertheless, if both transitions prove feasible the total Δq-value would add up to the above quoted 750 463 cm^{-1}.

2.3.2 Frequency standards in Hf^{12+} and W^{14+}

For the Nd-like elements with $Z < 70$, the ground state configuration is $4f^{12}5s^2$, with a ${}^3H_6$ ground state. In [30], the transition $4f^{12}5s^2\,{}^3F_4$-$4f^{12}5s^2\,{}^3H_6$ was suggested as frequency standard. This transition is of E2-type with a lifetime of 4.6 days and, hence, a radiative

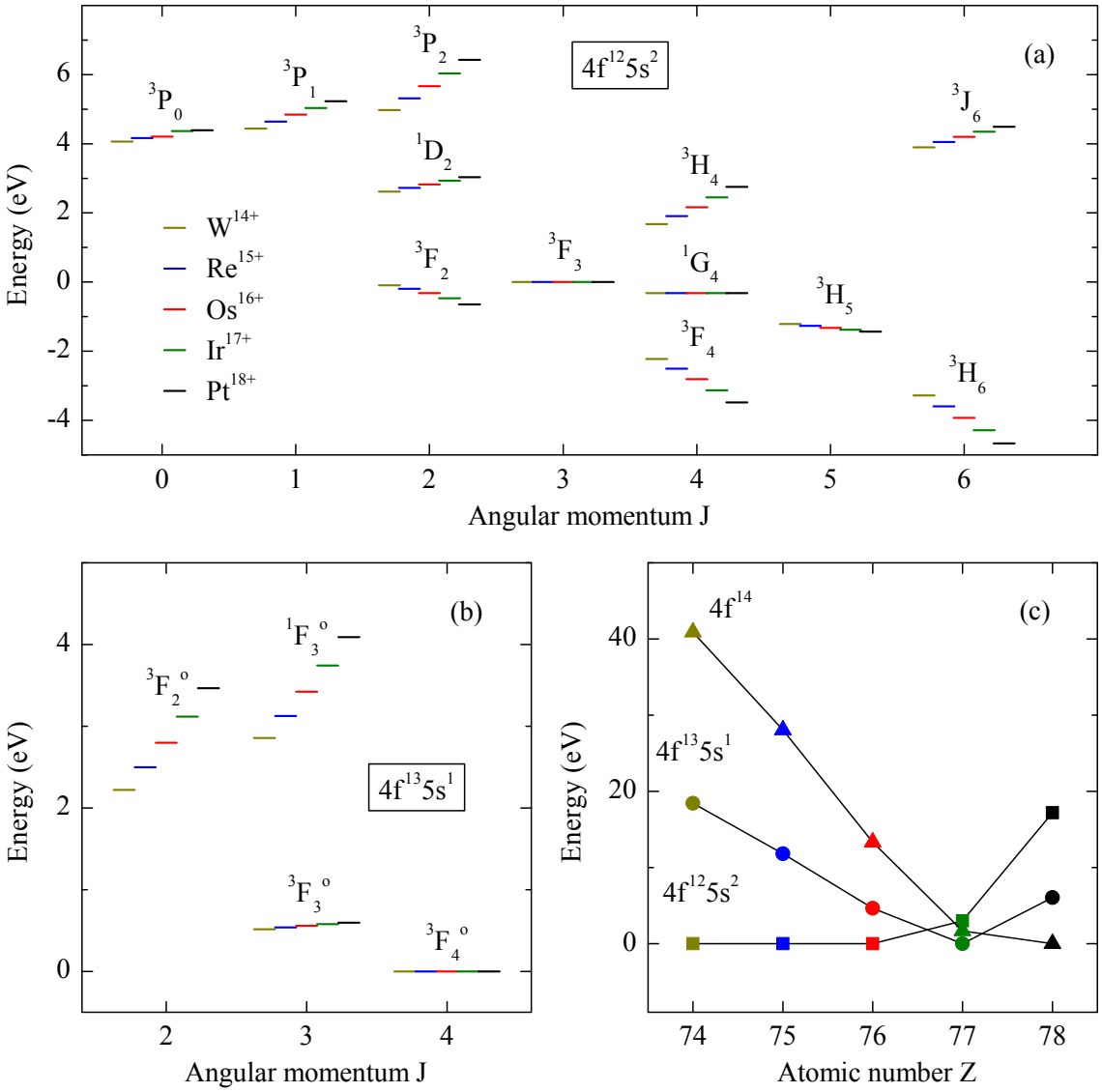

Figure 2.2: Grotrian diagrams based on FSCC calculations of the (a) $4f^{12}5s^2$, and (b) $4f^{13}5s^1$ configurations of Nd-like W, Re, Os, Ir, and Pt (Z=74–78). The fine structure splitting, shown here relative to the levels (a) $^3F_3$ and (b) $^3F^o_4$, scales smoothly and slowly which enables optical intra-configuration transitions for the all investigated ions. In (c), the energy separation between the lowest energy states in each configuration, $4f^{14}\,^1S_0$, $4f^{13}5s^1\,^3F^o_4$, and $4f^{12}5s^2\,^3H_6$ is plotted. The three configurations cross near Ir^{17+}, resulting in several α-sensitive optical inter-configuration transitions only in this ion.

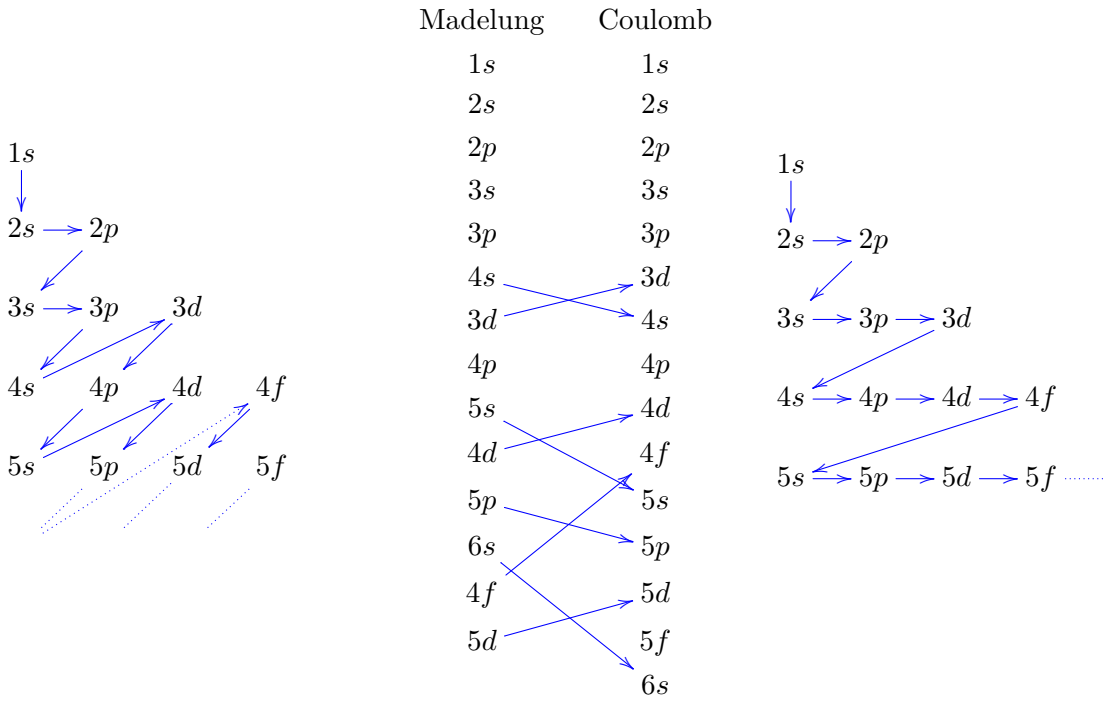

Figure 2.3: Transition between the Coulomb energy ordering of atomic orbitals and the Madelung ordering. In this work, the level crossing of the $4f$ and $5s$ orbitals is investigated. Adapted from [26].

width of approximately only 10 µHz. A prominent feature of these two ions is the absence of a nuclear spin, which simplifies the level structure for a clock application. Without a hyper fine structure, uncertainties arising from electric quadrupole shifts can be canceled by probing two transition frequencies ω_1, ω_2, involving states with different magnetic quantum numbers m_J. The unperturbed frequency $\omega_0 = (\omega_1 + \omega_2)/2$ is obtained by averaging, for example with $\omega_1(|^3F_4, m_\mathrm{J} = 3\rangle - |^3F_6, m_\mathrm{J} = 2\rangle)$ and $\omega_2(|^3F_4, m_\mathrm{J} = 3\rangle - |^3F_6, m_\mathrm{J} = 5\rangle)$ [30]. The external field dependence cancels out in this scheme and ω_0 only depends on the ratio of the two quadrupole moments leading to two orders of magnitude suppression of the uncertainty. The remaining error budget has been estimated below 10^{-19} relative frequency uncertainty which makes these ions perfectly suitable candidates for next generation frequency standards. However, as this scheme deals with intra-configuration transitions, there is no particularly high sensitivity to a changing fine structure constant, only on the order of $1000\,\mathrm{cm}^{-1}$ [25].

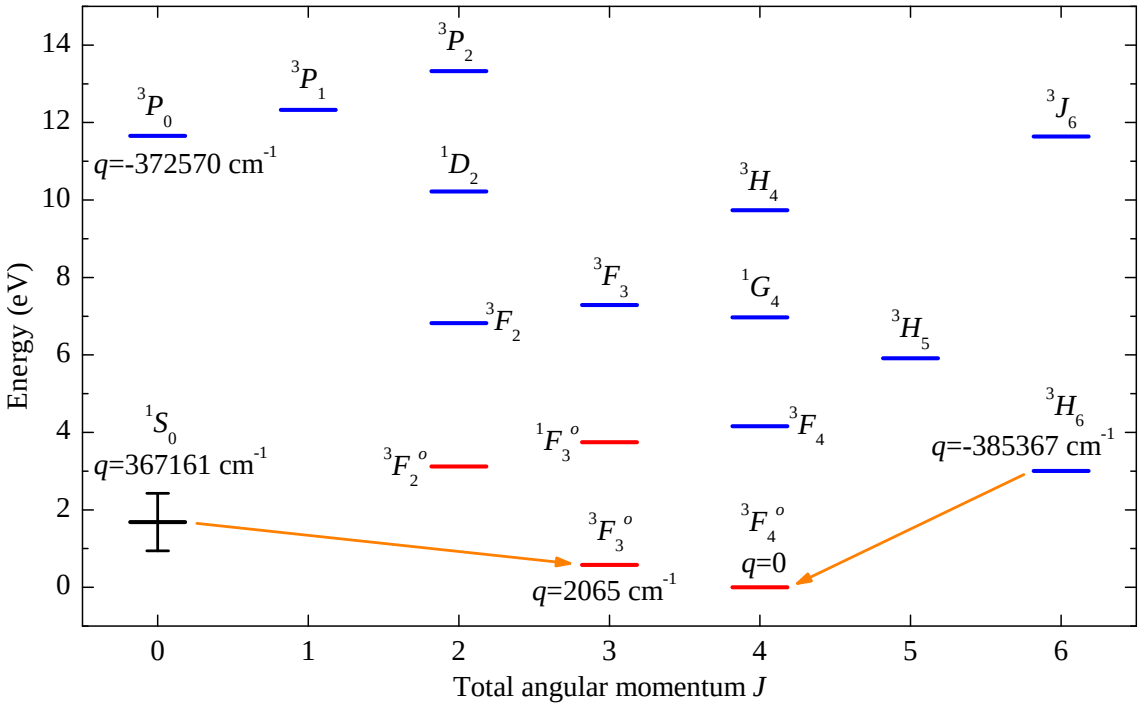

Figure 2.4: Grotrian diagram of the $4f^{12}5s^2$ (blue), $4f^{13}5s^1$ (red), and $4f^{14}$ (black) configurations in Ir^{17+}. The state energies are extracted from FSCC calculations and the q values from [25]. The transitions proposed as α-sensitive frequency standards are highlighted by orange arrows. While the $4f^{12}5s^2$ configuration shifts uniformly to higher energies for an increasing value of α, the $4f^{14}$ configuration shifts to smaller energies, and the $4f^{13}5s^1$ configuration is stays approximately constant. The estimated theoretical uncertainty [25] of roughly 0.7 eV for each state is representatively shown as error bar of the $^1S_0$ state.

2.4 Processes of highly charged ions in an electron beam ion trap

The first step towards the the application of Nd-like ions in metrology is gaining precise knowledge about their atomic structure, since the uncertainties of theoretical predictions are far too large to start with laser spectroscopy. Most of the ions studied in this work have never been investigated experimentally. Without having a benchmark or reference for the quality of the different theory methods, this challenge has to be approached experimentally. Ideal instruments to map the unknown spectra of Nd-like ions next to the $4f$-$5s$ level crossing are EBITs. Before proceeding with a general description of the experimental setup, in this section, an overview over the important physical processes in an EBIT is given. A dense electron beam, focused by the magnetic field of two superconducting coils, ionizes atoms sequentially up to the desired charge state by electron impact ionization. Simultaneously, the charge state of the ion can be reduced by electron exchange processes

with residual gas and recombination with the electron beam. The different competing processes cause an equilibrium state in which different charge states coexist in a population distribution. Trapped HCI are frequently excited by collisions with the electron beam. A huge advantage of these electron collisions is that ions are excited close to the continuum, regardless of photonic selection rules. While cascading from the continuum towards the ground state, ions emit photons from many possible transitions. Moreover, the deep trapping potentials in the EBIT are capable of storing large numbers of ions in the desired charge state, producing a strong photon signal. As a consequence, the full optical range of optical transitions can be obtained by spectroscopic investigation of the fluorescing ion cloud. The experimentally acquired spectral lines are broadened due to Doppler broadening, related to high temperatures in the EBIT, and features partially resolved Zeeman splitting. A model is introduced to recreate the resulting line shape, characteristic for each transition, and will be used for spectral line identification.

2.4.1 Ionization and recombination

To ionize an atom or ion X of positive charge q, an electron e^- needs to be removed from its outer shell. In an EBIT, this is achieved by colliding a beam of accelerated electrons with the ion X. If the kinetic energy E_e of the electron beam exceeds the ionization potential of the weakest bound electron in X, electron impact ionization

$$\mathrm{X}^{q+} + e^- \rightarrow \mathrm{X}^{(q+1)+} + 2e^- \tag{2.30}$$

can occur. By this process, the charge state of an ion can be increased step wise, until $\mathrm{X}^{q+} < E_\mathrm{e} < \mathrm{X}^{(q+1)+}$. At this point, the electron beam energy becomes too low to ionize the ion to produce the next higher charge state, and an charge equilibrium state will be established. The efficiency of the electron impact ionization can be expressed through its cross section $\sigma_\mathrm{ie}(E_\mathrm{e})$ approximated by the Lotz-formula [47, 69]

$$\sigma_\mathrm{ie} = \sum_n a_\mathrm{n} k_\mathrm{n} \frac{\ln E_\mathrm{e}/I_\mathrm{n}}{E_\mathrm{e} I_\mathrm{n}} \left(1 - b_\mathrm{n} \mathrm{e}^{c_\mathrm{n}(1-E_\mathrm{e}/I_\mathrm{n})}\right). \tag{2.31}$$

The cross section is summed over the number of subshells N, while k_n is the number of electrons in each subshell. a_n, b_n, and c_n are empirical parameters. Several electron impact ionization cross sections of relevant Ir ions, calculated using equation (2.31), are presented in table 2.3. While the electron beam energy E_e is increased, the ionization threshold I_n of the charge state q is crossed and σ_ie rises with $E_\mathrm{e}/I_\mathrm{n}$ up to a maximum at an electron beam energy of approximately $E_\mathrm{e} \approx 2.3 I_\mathrm{n}$. From this point on, the population of X^{q+} is shifted to $X^{(q+1)+}$. In heavy many-electron systems, as the Nd-like ions investigated here, the ionization potentials for the different charge states are very close, only separated by

Table 2.3: Examples of electron impact ionization cross sections calculated using equation (2.31). The ionization potentials are taken from [50] and the parameters a_n, b_n, and c_n from [70]. In Chapter 5, the spectra of the intermediate charge states around Ir^{17+} are mainly investigated, but also Ir^{55+} which is significantly more difficult to produce at high quantities.

Charge state q	Ionization potential I_n (eV)	Maximum cross section σ_ie (cm^2)
0→1	9	1.9×10^{-15}
16→17	407	6.6×10^{-19}
54→55	5229	1.4×10^{-21}
76→77	88 113	3.0×10^{-25}

tens of eV. In these cases, the maximum population in a charge state q is not determined by the maximum cross section. Beforehand, the ionization threshold of of the next higher charge state $q+1$ is reached and the population is transferred from charge state q to $q+1$. From that point on, the population in q decreases although the cross section still increases. Thus, the ionization threshold of $q+1$ marks the electron beam energy which maximizes the population in q.

The radiative recombination process is responsible for a decrease of the charge state. An ion can capture a free electron from the electron beam by

$$\mathrm{X}^{q+} + e^- \rightarrow \mathrm{X}^{(q-1)+} + h\omega. \tag{2.32}$$

The energy difference ΔE between the electron beam energy and the ionization potential of $\mathrm{X}^{(q-1)+}$ is released as a photon with the energy $h\omega$. The cross section for this process can be estimated using a formula derived by Y. S. Kim and R. H. Pratt [71]

$$\sigma_\mathrm{rr} = \frac{8\pi\alpha^5 Z_\mathrm{eff}^4}{3\sqrt{3}n^3 E_\mathrm{e} h\omega} \tag{2.33}$$

and depends on the main quantum number n of the state the electron recombines into, as well as the electron beam energy. The cross section σ_rr increases with the charge state of the trapped ions, but decreases for the higher electron beam energies needed. More generally, the charge state can also be reduced by the exchange of j electrons during collisions with neutral residual gas particles A as described by the process

$$\mathrm{X}^{q+} + \mathrm{A} \rightarrow \mathrm{X}^{(q-j)+} + \mathrm{A}^{(j)+}. \tag{2.34}$$

For a short period of time, the two approaching particles form a quasi-molecule with a common potential curve. Since the HCI ionization potential is much deeper than the

ionization potential for its neutral partner $I_{\mathrm{A,n}}$, electrons can be transferred from the neutral atom to the ion. The cross section for the charge exchange can be empirically approximated by the Müller and Salzborn formula [72, 73]

$$\sigma_{\mathrm{ce}} = 2.6 \times 10^{-13} \frac{jq}{I_{\mathrm{A,n}}^2} \,\mathrm{eV}^2\,\mathrm{cm}^2, \tag{2.35}$$

under the assumption of slow collisions and $q \gg j$ which is usually justified for trapped highly charged ions. While charge exchange can be strongly suppressed by working at very low residual gas densities, e.g., in the cryogenic vacuum of an EBIT, radiative recombination (2.32) cannot be prevented. However, radiative recombination is commonly much slower than electron impact ionization (2.30) in an EBIT [74] as long as the charge states are not too high.

The listed processes govern the production of charge states trapped at equilibrium conditions in the EBIT. Other interesting processes as Auger decays, resonant recombination, and ion-ion charge exchange do not play a major role for this work. The different competing processes can be condensed in the rate equation [74]

$$\begin{aligned}\frac{\mathrm{d}N_{\mathrm{q}}}{\mathrm{d}t} =& \frac{j_{\mathrm{e}}}{e}\left[N_{\mathrm{q}-1}\sigma_{\mathrm{ie,q}-1}(E_{\mathrm{e}})f_{\mathrm{q}-1} + N_{\mathrm{q}+1}\sigma_{\mathrm{rr,q}+1}(E_{\mathrm{e}})f_{\mathrm{q}+1} - N_{\mathrm{q}}\left(\sigma_{\mathrm{ie,q}} + \sigma_{\mathrm{rr,q}}\right)f_{\mathrm{q}}\right] \\ &+ N_{\mathrm{A}}\left(N_{\mathrm{q}+1}\sigma_{\mathrm{ce,q}+1}\bar{v}_{\mathrm{q}+1} - N_{\mathrm{q}}\sigma_{\mathrm{ce,q}}\bar{v}_{\mathrm{q}}\right) - N_{\mathrm{q}}R_{\mathrm{esc,q}}.\end{aligned} \tag{2.36}$$

The solution to this differential equation yields the number of ions N in the charge state q. The contributions from impact ionization and radiative recombination depend on the electron beam current density j_{e} and the charge exchange on the number of residual gas atoms N_{A} as well as the mean ion velocities $\bar{v}$. $R_{\mathrm{esc,q}}$ accounts for rate of ions escaping the trap and the parameters f for the spatial overlap between ion and electron beam. Equation (2.36) features strong correlations between the number of ions in different charge states. For these reasons ions cannot be prepared in a single charge state but rather as a distribution depending on the electron beam energy.

2.4.2 Excitation and deexcitation

Besides the electron impact ionization and radiative recombination, ions can also be excited to a higher electronic state by electronic collisions:

$$\mathrm{X}^{q+} + e^- \rightarrow (\mathrm{X}^{q+})^* + e^- \rightarrow \mathrm{X}^{q+} + e^- + \sum_i^I h\omega_{\mathrm{i}}. \tag{2.37}$$

A part of the kinetic energy of the electron is here transferred to the electronic shell of the ion, leaving it in an excited state marked by $*$. In fact, the different collisional processes

cannot be disentangled. When ions are ionized or recombine, they are generally excited simultaneously. An excited state may decay by the emission of a photon. Usually, the ions are highly excited by electron impact inside the EBIT, so that states close to the ionization threshold are populated. The highly excited electrons quickly cascade down towards the ground state via I lower states. During the decay I photons with a variety of energies can be emitted. Although transitions with a high energy are preferred (from equation (2.5): for E1 transitions $A \propto \omega^3$), all excited states finally decay back into the ground state configuration. For the Nd-like ions this means that a considerable population will decay through transitions in the lowest energy configurations $4f^{12}5s^2$ and $4f^{13}5s^1$ which ensures a strong optical photon signal.

In addition, excited states can be depleted by collisions

$$(\mathrm{X}^{q+})^* + e^- \rightarrow (\mathrm{X}^{q+})^{**} + e^-, \tag{2.38}$$

which prevents photonic decay from the specific electronically excited state * by transforming it into **. If the electron collision rate exceeds the the photonic decay rate of a state, the spectral lines of the corresponding transitions are quenched. To obtain an order of magnitude estimate, a typical cross section $\sigma \approx 10^{-22}\,\mathrm{cm}^2$ (from FAC calculations), an electron beam of 40 mA, and approximately 25 µm radius (see equation 3.1) would result in collision rates on the order of 50 Hz. Consequently, the detection of transition rates much lower than 50 Hz would be hampered. A signal would of course additionally depend strongly on the excited ion population, but for a qualitative statement the collision rate can be compared to radiative transition rates resulting from FAC calculations. Commonly M1 transition rates in $4f^{12}5s^2$ and $4f^{13}5s^1$ configurations of the Nd-like ions are on the order of few 100 Hz and can thus be spectroscopically investigated. Even lower transition rates could be investigated by switching the electron beam of and confining the ions in the magnetic trapping mode, as has been demonstrated for instance in [75, 76].

2.4.3 Spectral lines

The photon intensity emitted during an electronic transition is spectrally distributed as a resonance curve around a centroid determining the transition energy. The shape of these resonance curves, which are detected in the experiment, depends on several factors. The reason for the finite energy width of the resonance curves, is the energy-time uncertainty relation. An ensemble of ions in an excited state decaying at a rate A (see equation (2.5)), emits photons distributed around a center frequency ω_0 corresponding to the transition energy. The spectral intensity distribution $I(\omega)$, as a function of the photon frequency ω,

is the Fourier transform of the time t dependent amplitude of the field (see e.g. [77])

$$I_{\mathrm{N}}(\omega) = \frac{I_0}{\sqrt{2\pi}} \int_{-\infty}^{\infty} \mathrm{e}^{(\mathrm{i}\omega_0 - A)t} \mathrm{e}^{\mathrm{i}\omega t} \mathrm{d}t = \frac{1}{2\pi} \frac{A}{(\omega - \omega_0)^2 + (A/2)^2}. \tag{2.39}$$

I_0 is a normalization constant. Thus, the decay rate A translates directly into the FWHM of the resultant Lorentz profile, also referred to as the natural linewidth. In the case of the investigated optical transitions, the natural linewidths are expected to be of the order of 10^2 Hz.

With the experimental setup used in this work, natural line broadening cannot be observed as there are two other dominating broadening mechanisms that are superimposed on it. The first effect, the Doppler broadening, originates from the production and storage of the fluorescing HCI. Through the constant electron bombardment, the HCI in the EBIT are heated up to typical temperatures of 10^5 to 10^6 K (see Chapter 3). The thermal velocities of HCI are characterized by a Boltzmann distribution and have velocity components towards and against the direction of the observer. Each emitted photon is frequency shifted according to the Doppler effect. For a large ensemble, these shifts yield a statistical line broadening and a normalized Gaussian profile [77]

$$I_{\mathrm{D}}(\omega) = \frac{1}{\sqrt{2\pi}\sigma_{\mathrm{D}}} \mathrm{e}^{-\frac{1}{2}\left(\frac{\omega-\omega_0}{\sigma_{\mathrm{D}}}\right)^2}, \tag{2.40}$$

$$\sigma_{\mathrm{D}} = \omega_0 \sqrt{\frac{k_{\mathrm{B}} T}{m_{\mathrm{ion}} c^2}}, \tag{2.41}$$

with the Boltzmann constant k_{B}. The Gaussian width σ_{D} takes values of 10^{10} Hz at temperatures of $T = 1$ MK for the ion mass of Ir $m_{\mathrm{ion}} = 192$ u and an optical frequency of $\omega_0 = 750$ THz. Compared to the Doppler broadening, the natural line width can be completely neglected.

The other broadening mechanism is due to the spectral response of the spectrometer used to acquire the spectral lines. This instrumental resolution σ_{inst} is in the present case expected to be similar in amplitude to the Doppler width and adds another Gaussian contribution $\sigma = \sqrt{\sigma_{\mathrm{D}}^2 + \sigma_{\mathrm{inst}}^2}$. The width σ_{inst} is obtained experimentally and is evaluated in Chapter 4.

2.4.4 Zeeman splitting

The electron beam in the EBIT is focused through the trap center by a magnetic field of 8 T which induces another modification of the Gaussian profile of the spectral lines emitted by the ion cloud. By breaking the spatial isotropy, the magnetic field splits the otherwise energy degenerate states $|\gamma J m_{\mathrm{J}}\rangle$ depending on their magnetic quantum number

$m_\mathrm{J} = -J \ldots J$. Assuming the energy splitting caused by the magnetic field is much smaller than the fine structure splitting, which is usually justified for HCI, it can be described by the linear Zeeman effect. Unlike the other perturbative effects mentioned in section 2.1, the Zeeman effect is not strongly influenced by the increased nuclear charge of HCI. In first order pertubation theory the small energy correction to the Hamiltonian is given as (see e.g. [47])

$$\Delta E^{(1)} = \mu_\mathrm{B} m_\mathrm{J} g B_\mathrm{z}. \tag{2.42}$$

The magnetic field is aligned along the z-axis, parallel to the electron beam. The g-factors are gyromagnetic ratios, indicating the magnetic moment induced by an electron with a total angular momentum J. The Zeeman splitting related to the nuclear spin states m_I is not considered because the magnetic moment of the nucleus has negligible size compared to that of the electron. The g-factors can be estimated by the Landé formula

$$g_\mathrm{J} = 1 + \frac{J(J+1) - L(L+1) + S(S+1)}{2J(J+1)}. \tag{2.43}$$

The $2J + 1$ Zeeman components are split symmetrically around the line centroid and are separated by equal energy intervals. For transitions between Zeeman substates, the m_J levels have to be treated individually. According to the selection rule (2.7), only transitions with $\Delta m = 0, \pm 1$ are strong enough to be observed. The Nd-like ions have angular momenta as high as $J = 6$, which means that spectral lines can be divided into 13 Zeeman components for each value of Δm. The typical energy separation can be estimated using equation (2.42) to be on the order of $10^{10}\,\mathrm{Hz}$, similar to the Doppler width and therefore on the edge of the resolving power. Even if single Zeeman components cannot be resolved, spectral lines can be significantly broadened and the Gaussian lineshape would be distorted.

To reconstruct the line shape of transitions between arbitrary J-states, a model is introduced as depicted in figure 2.5 is introduced. The energy for the Zeeman components of a transition $m_\mathrm{J} \rightarrow m_\mathrm{J} + \Delta m$ can be written as

$$E(\Delta m, m_\mathrm{J}) = E_0 + \mu_\mathrm{B} B (m_\mathrm{J}(g - g') + \Delta m g'), \tag{2.44}$$

with the upper (lower) level $g(g')$-factor. E_0 is the unperturbed transition energy, now represented as the centroid of the Zeeman split spectral line.

To calculate the relative intensity for the Zeeman components within one Δm-group equation (2.5) can be used

$$\frac{A_{|\gamma \mathrm{J} m_\mathrm{J}\rangle, |\gamma \mathrm{J} m_\mathrm{J} + \Delta \mathrm{m}\rangle}}{A_{|\gamma \mathrm{J} m'_\mathrm{J}\rangle, |\gamma \mathrm{J} m'_\mathrm{J} + \Delta \mathrm{m}\rangle}} = \frac{|\langle \gamma J m_\mathrm{J} | T | \gamma J m_\mathrm{J} + \Delta m \rangle|^2}{|\langle \gamma J m'_\mathrm{J} | T | \gamma J m'_\mathrm{J} + \Delta m \rangle|^2}, \tag{2.45}$$

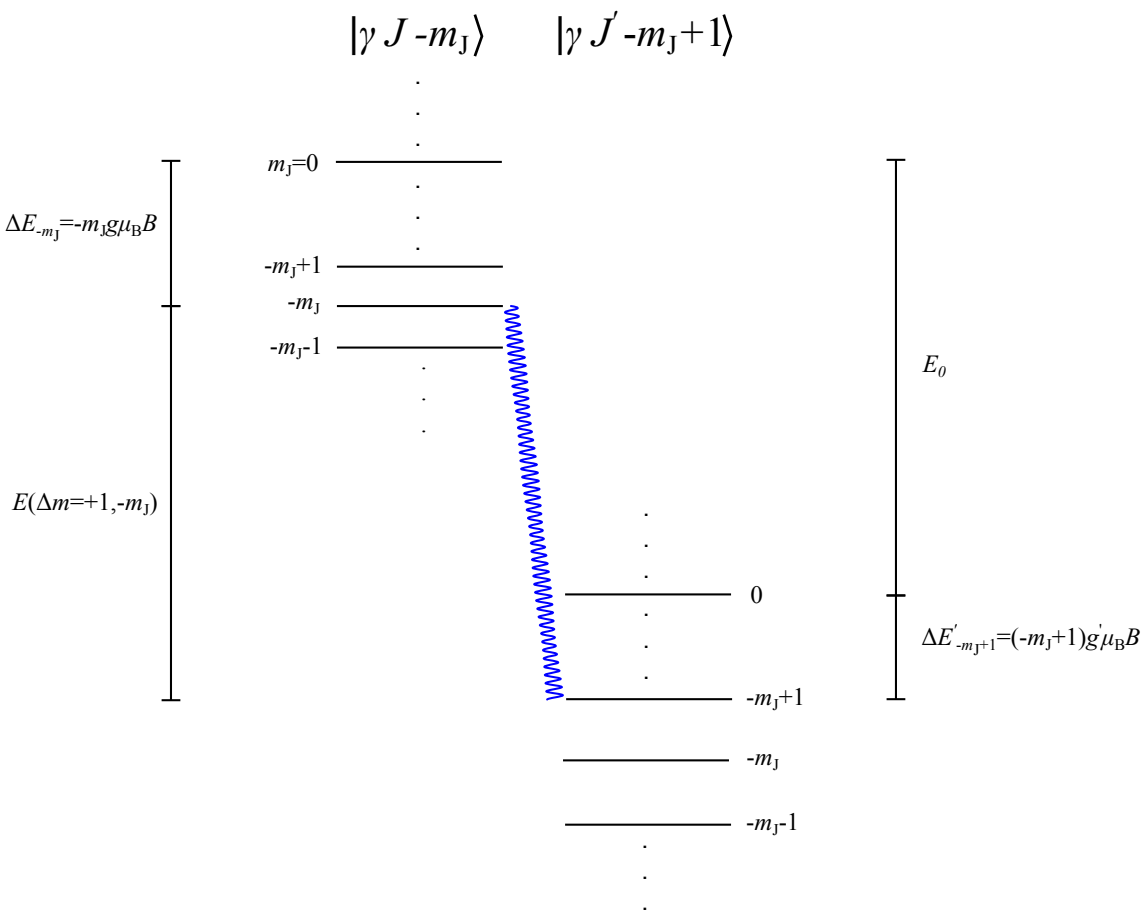

Figure 2.5: Exemplary sketch for the determination of the transition energy $E(\Delta m = 1, m_\mathrm{J})$ between two Zeeman split states $|\gamma\ J\ -m_\mathrm{J}\rangle \rightarrow\ |\gamma\ J'\ -m_\mathrm{J}+1\rangle$. The energy can be obtained by $E(1,-m_\mathrm{J}) = E_0 + \Delta E'_{-\mathrm{m_J}+1} - \Delta E_{-\mathrm{m_J}}$ and can be generalized to yield equation (2.44).

assuming that $\Delta E^{(1)}$ is much smaller than the transition energy. The transition operator is represented by T. The magnetic quantum number m'_J is fixed and taken as a reference state for the Δm-group. According to the Wigner-Eckart theorem (see e.g. [77]) equation (2.45) can be simplified by using reduced matrix elements $\langle\gamma J||T||\gamma J\rangle$. Their m_J-dependence is transferred into the Clebsch-Gordan coefficient $\langle J\ m_\mathrm{J}\ 1\ \Delta m|J'\ m_\mathrm{J}+\Delta m\rangle$:

$$\frac{|\langle\gamma J m_\mathrm{J}|T|\gamma J m_\mathrm{J}+\Delta m\rangle|^2}{|\langle\gamma J m'_\mathrm{J}|T|\gamma J m'_\mathrm{J}+\Delta m\rangle|^2} \tag{2.46}$$

$$= \langle J\ m_\mathrm{J}\ 1\ \Delta m|J'\ m_\mathrm{J}+\Delta m\rangle^2\ \frac{|\langle\gamma J||T||\gamma J\rangle|^2}{|\langle\gamma J||T||\gamma J\rangle|^2} \tag{2.47}$$

$$= \langle J\ m_\mathrm{J}\ 1\ \Delta m|J'\ m_\mathrm{J}+\Delta m\rangle^2\,. \tag{2.48}$$

The full Zeeman pattern can now be obtained by summing over all components

$$f'(E) = \sum_{\Delta m=-1,0,1} a_{\Delta \mathrm{m}} \sum_{-J\leq m_\mathrm{J}\leq J} \langle J\ m_\mathrm{J}\ 1\ \Delta m|J'\ m_\mathrm{J}{+}\Delta m\rangle^2\, \delta(E - E(\Delta m, m_\mathrm{J})) \quad (2.49)$$

The $a_{\Delta \mathrm{m}}$ are are empirical scaling factors accounting for the absolute measured intensities. These depend on Einstein coefficients and the electronic population in the excited state. Moreover, the $a_{\Delta \mathrm{m}}$ are different for the different polarizations Δm due to polarization-dependent optical elements used in the experimental setup. The overlap of the angular intensity distributions with the detection area also changes with Δm. This can be shown with the help of the angular intensity distributions

$$I_{\Delta \mathrm{m}=0} \propto \sin^2\theta, \quad (2.50)$$

$$I_{-1,1} \propto \frac{1+\cos^2\theta}{2}, \quad (2.51)$$

with the angle θ with respect to the magnetic field. For $\Delta m = 0$ the maximum of the radiation intensity points in direction of the optical spectrometer at $\theta = 90°$ but is tilted to $0°$ in case of the $\Delta m = -1$ and $\Delta m = 1$, which is why $a_0 > a_{-1,1}$ for the experimental setup used in this work. Considering M1 transitions without parity change, the polarization of the $\Delta m = 0$ components is perpendicular to the magnetic field of the EBIT while the polarization of the $\Delta m = -1$ and $\Delta m = 1$ components is aligned with it. Because of their identical polarization a_{-1} can be assumed equal to a_1. For transitions with parity change, such as E1 transitions the polarizations would be switched between the $\Delta m = 0$ components and the $\Delta m = -1, 1$ compared to the parity conserving case.

Examples of possible Zeeman patterns for several J, g, and g' are shown in figure 2.6. By convolving the Zeeman pattern of equation (2.49) with the Gaussian profiles expected from Doppler broadening and the spectral resolution, a model is obtained that is generally applicable for the Zeeman splitting of any transition

$$\begin{aligned} f(E) = &\sum_{\Delta m=-1,0,1} a_{\Delta \mathrm{m}} \sum_{-J\leq m_\mathrm{J}\leq J} \langle J\ m_\mathrm{J}\ 1\ \Delta m|J'\ m_\mathrm{J}{+}\Delta m\rangle^2 \\ &\times \exp\left(-\frac{(E - E_0 - \mu_\mathrm{B} B\,(m_\mathrm{J}\,(g-g') + \Delta m\, g'))^2}{2w^2}\right). \end{aligned} \quad (2.52)$$

As can be seen in figure 2.6, the final line shapes depend strongly on characteristic parameters of the involved states. These dependencies are used in Chapter 6 as a powerful tool for the identification of spectral lines.

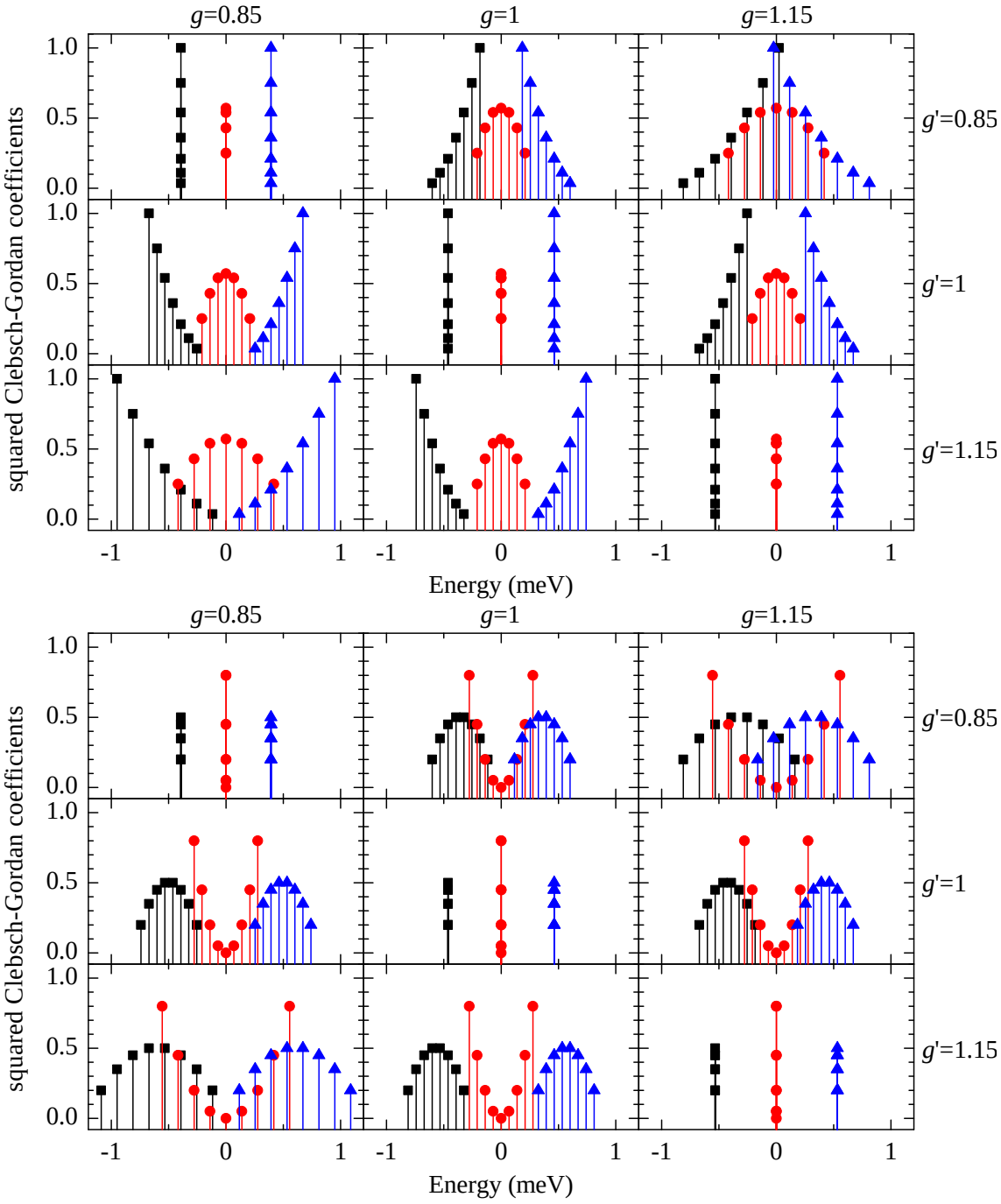

Figure 2.6: Examples of observable Zeeman patterns. The different symbols and colors refer to the different photon polarizations $\Delta m = -1, 0, 1$ (black squares, red circles, blue triangles, respectively). The Zeeman components can be obtained from equation (2.49) for $a_{-1,0,1} = 1$. Several combinations of g,g'-factors are shown for a $J = 3 \rightarrow 4$ (top) and a $J = 4 \rightarrow 4$ transition (bottom). It can be noticed that the difference in the g,g'-factors strongly influences the spread of the spectral lines. Although the g,g'-factors are only changed on the order of 10 %, the patterns are significantly distinct. In particular, the Zeeman structure changes fundamentally between $\Delta J = 1$ and $\Delta J = 0$ transitions.

Chapter 3

Experiment

The experimental setup used to trap, produce and analyze the optical light radiated by the Nd-like ions consisted of the Heidelberg EBIT [35] combined with a Czerny-Turner (CT) spectrometer. The working principles and the setup of these instruments will be outlined in this chapter. Neutral atoms were injected into the EBIT, where they were ionized and excited to fluoresce. The emitted light by the ions in the optical wavelength region was collected by an imaging system inside the vacuum chamber to maximize the solid angle and imaged through a window onto a periscope box outside of the EBIT vacuum chamber. The periscope box rotated the horizontal ion cloud image by 90° along the entrance slit of the CT spectrometer. Here the light was dispersed into its spectral components by an exchangeable grating. Gratings with different groove densities could be chosen to switch between low-resolution broadband and high-resolution narrow-band spectra. The spectral components are imaged onto a nitrogen cooled CCD chip where the spectra are acquired.

3.1 The Heidelberg Electron Beam Ion Trap

Electron beam ion traps are very efficient tools for the production and storage of HCI [78]. The name already describes the working principle: A monochromatic electron beam is used to ionize ions successively by electron impact and keep them trapped by its negative space charge potential. The required energy is much lower for the step-wise ionization of the atoms and ions compared to removing all electrons at once, as it is done in storage ring ion sources [79] by shooting the ions through stripping foils. As a consequence, EBITs can be constructed in a very compact fashion compared with accelerator-based sources. As example, FLASH EBIT [80] is frequently transported to external x-ray and vacuum-ultra-violet light sources [81, 82] and novel permanent-magnet EBITs can be even set up on a table top [83].

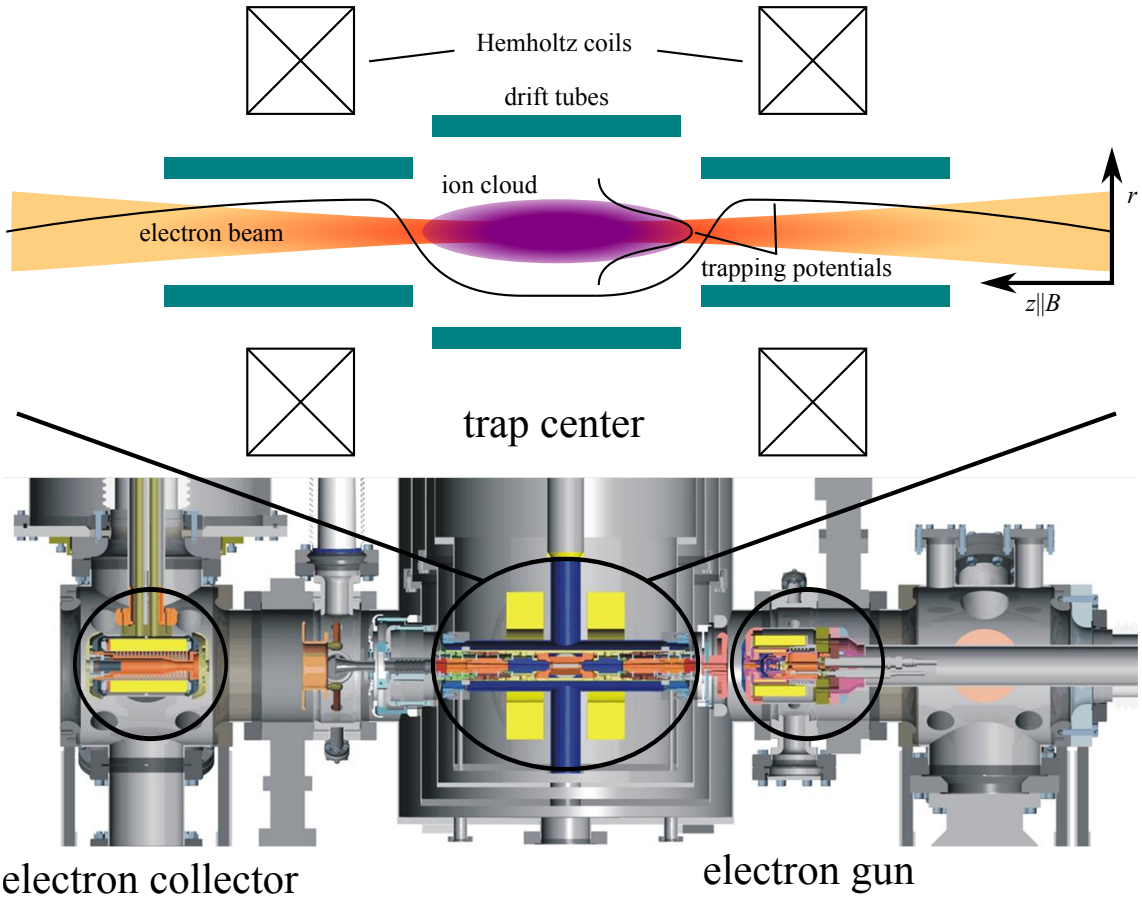

Figure 3.1: Top: Sketch of the working principle of an EBIT. Bottom: Section view of the Heidelberg EBIT. The three main components, the electron gun, the collector, and the trap center are introduced in this section.

The components of an EBIT are depicted in figure 3.1 and will be introduced in the following. The electron beam is produced in the electron gun by thermal emission from a heated cathode. An acceleration potential, generated by a set of electrodes, extracts the electrons from the gun and leads them towards the center of the EBIT. Two superconducting magnet coils in Helmholtz configuration, left and right of the trap center, generate a homogenic magnetic field along the electron beam axis in the vicinity of the trap center. The electrons leaving the electron gun circle around the magnetic field lines and the electron beam is compressed towards the trap center, where the magnetic field is strongest. After passing the center, the electron beam expands again and is absorbed in the electron collector which is water cooled to handle the large beam currents.

A beam of neutral atoms or molecules is injected crossing the electron beam perpendicularly from below. Impact ionized ions are axially trapped by electrostatic potentials formed by a set of nine drift tubes. The negative space charge of the dense electron beam in the center traps the ions radially and attracts them towards the central axis where

they are further ionized. This process continues until the ionization potential of the next higher charge state exceeds the electron beam energy. The fluorescence signal produced by trapped ions bombarded by electrons is analyzed by the optical setup introduced in the section 3.2

The main attributes of the Heidelberg EBIT are the high-voltage suitability, the cryogenic engineering, and its horizontal alignment. The insulation of the Heidelberg EBIT is commissioned to withstand potential differences of 300 kV between the electron gun and the trap center. The resulting electron beam energy enabled the production of He-like Hg^{78+} [84] and would potentially suffice for the efficient ionization of U^{91+}. Another advantage, more relevant for this work, is the efficient cooling system. The magnets and the trap center were contained by a 50 l liquid He cryostat which is isolated by two thermal shields, pre-cooled at 50 K and 20 K. With this setup the EBIT can be operated for approximately one week with a single He fill which is important for maintaining reproducible conditions for long term measurements. The horizontal alignment simplifies the extraction of ions.

3.1.1 The electron gun

A section view of the electron gun is given in figure 3.2. The central element of the electron gun is a cylindrically shaped cathode, with a diameter of 3 mm, and a concave emitting surface facing the trap center. The cathode consists of a tungsten matrix doped with barium. Due to its low work function of approximately 2 eV, the barium deposited on the surface emits a sufficient number of electrons if the cathode is heated to temperatures of around 1100 °C. The emitting barium layer is constantly replenished by barium diffusion through the tungsten matrix to the surface which provides a constant supply of free electrons.

The electrons are extracted from the gun by applying a potential difference between the cathode and the anode. A voltage applied to a focusing electrode between the two are used to control the electron beam current. For the experiments with Nd-like ions the cathode is kept at voltages of 170 V to 300 V and the anode at 0 to few 10 V. By setting the focus electrode to a negative voltage below the cathode voltage, the beam can be blocked. In order to reach the desired current, the focus voltage is carefully ramped up to currents of typically 10 mA ot 40 mA. The residual magnetic field from the superconducting magnet coils in the center could disturbs the electron beam when exiting the gun. The bucking coil and the trimming coil can be used to compensate for such effects and improve the electron beam focusing.

3.1.2 The electron collector

After passing the trapping region the electron beam needs to be decelerated and absorbed. This is achieved through the electron collector which is schematically depicted in figure 3.3. The residual magnetic field of the central coils is compensated by the collector coil which causes the electron beam to diverge inside the collector and hit the walls. Secondary electrons produced in this process are prevented from escaping the collector by a small suppressor electrode voltage. A voltage applied to the extractor electrode at the end of collector stops remaining beam electrons and can be used to extract HCI produced in the EBIT for external experiments. With an optimized beam pointing, the whole beam current should be absorbed in the collector.

3.1.3 The trap center

Eight cylindrical drift tubes and a central one having slotted apertures in the center of the EBIT are used to shape an axial trapping potential for the HCI. Their diameters decrease towards the center, but expand at the entrance to drift tube 9 which has an inner diameter of 10 mm. The drift tubes can be addressed individually or biased commonly. In first order the electron beam energy is determined by the potential difference between its origin in the gun and the central drift tube. By controlling the bias voltage, this allows to adjust the desired electron beam energy while conserving the trap shape. The trapped ions can be dumped to avoid a slow build up of tungsten or barium originating from the cathode by increasing the central electrode voltage for about 100 ms. Both, the super conducting magnet coils and the drift tubes are located in a 50 l liquid He cryostat. By cooling the walls of the vacuum chamber down to 4.2 K, the vacuum at the trap center can be brought below 10^{-13} mbar. As has been shown in section 2.4.1, the good vacuum is essential to produce high ionic charge state efficiently. The magnet is operated at a current of 76.24 A to generate a magnetic field of 8 T at the central drift tube. This field is necessary to compress the electron beam to approximately 50µm. Otherwise the electron beam would expand due to its own negative space charge potential.

The slotted apertures on the central drift tube gave access to the trap center. Vertical apertures were used to detect the fluorescence signal emitted by the ion cloud. An optical telescope was mounted directly to the magnet housing in a distance of 150 mm from the trap center to increase the solid angle.

3.1.4 The injection

Below the center, an injection system is installed, which guides an atomic or molecular beam through the trap center containing the species of interest. The investigated Nd-like ions were injected into the EBIT as volatile organo-metallic compounds: $W(CO)_6$,

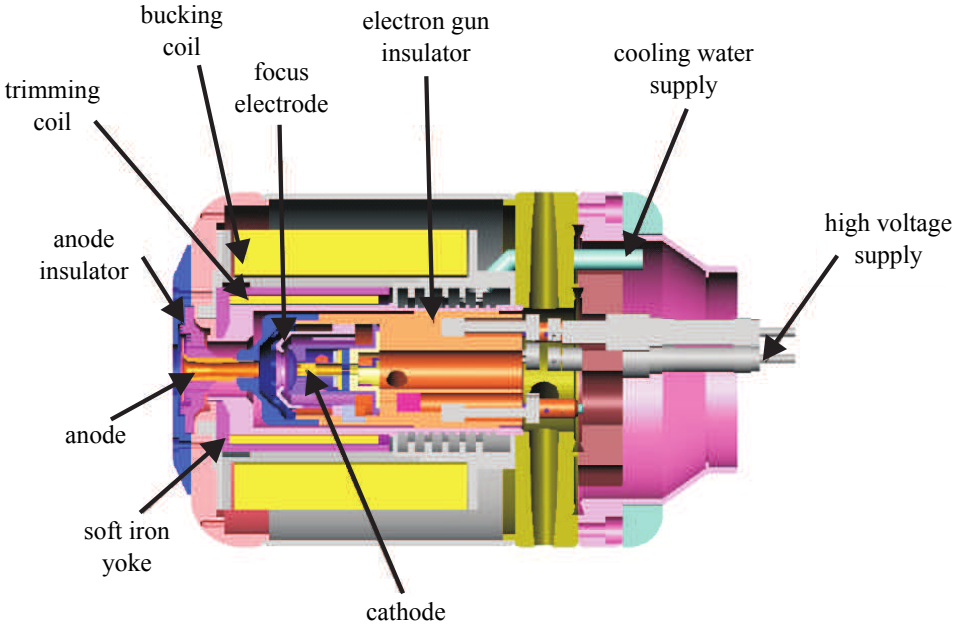

Figure 3.2: Section view of the electron gun.

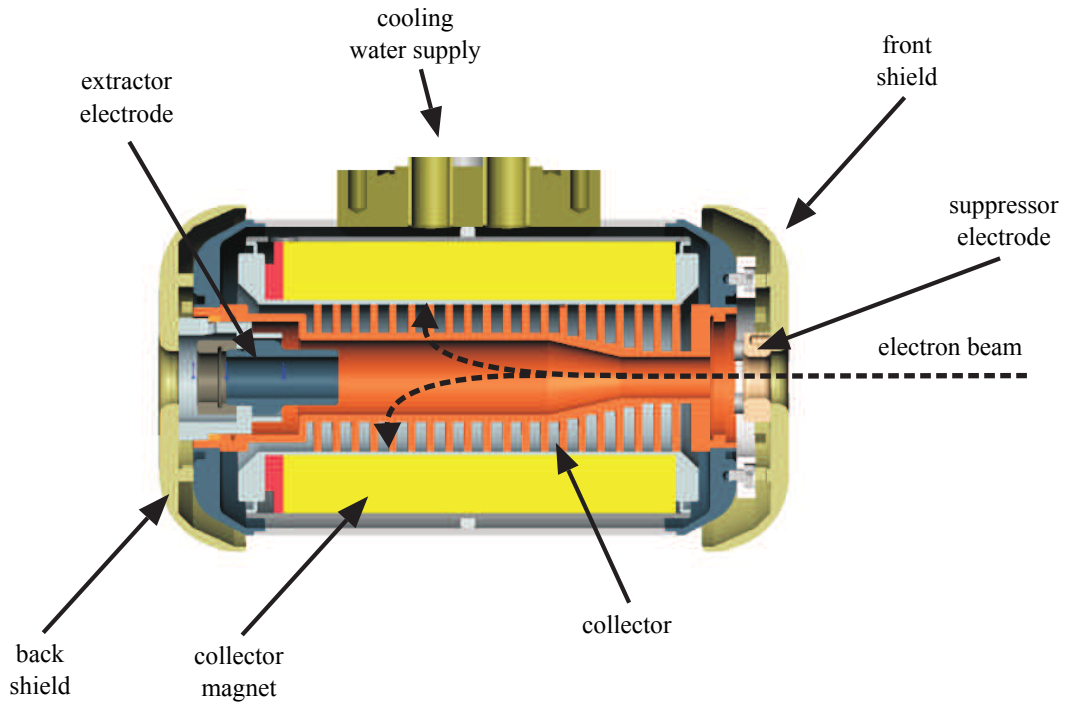

Figure 3.3: Section view of the electron collector.

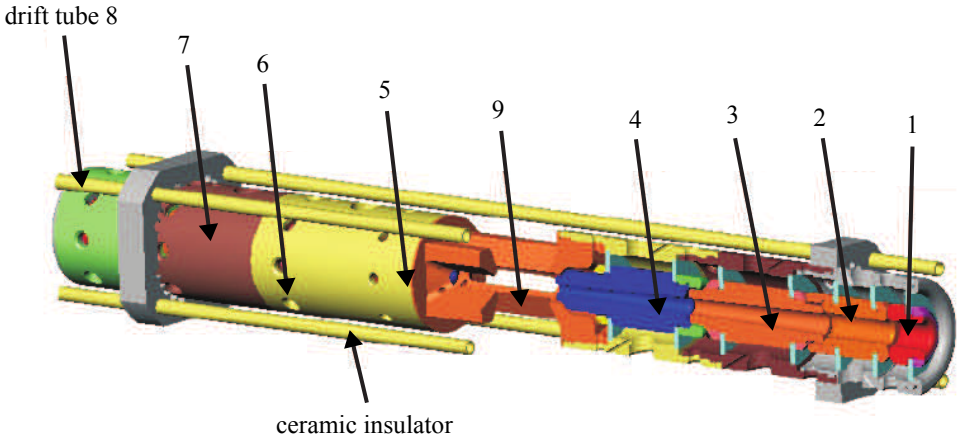

Figure 3.4: Section of the drift tube assembly in the center of the EBIT.

$C_5H_5Re\,(CO)_3$, $C_{10}H_{10}Os$, $(C_6H_7)(C_8H_{12})Ir$, and $C_5H_4CH_3Pt(CH_3)_3$. An amount of 0.1–1 g of organo-metal was kept in a small vacuum container and attached to the injection system below the EBIT. The compounds evaporate at room temperature inside of a vacuum vessel providing a source of gas at the temperature-dependent vapor pressure. Through a set of two apertures, a collimated molecular beam is formed and overlapped with the electron beam. The space between the two apertures is differentially pumped to minimize the contamination of the trap region with gas molecules. The injection pressure, measured between the two apertures, was set to values of 1-5$\times 10^{-8}$ mbar. Molecules hit by the electron beam dissociate. Only the metallic ions remain efficiently trapped and were cooled by the loss of light ions from the trap.

3.1.5 The electron beam

An accurate determination of the electron beam energy is important to predict the produced charge states of the ions trapped in the EBIT. At the high electron density in the trap center, the electron beam generates a strong space charge potential. This negative potential plays a substantial role in the trapping of ions and moreover, decreases the effective acceleration potential, hence, the electron beam slows itself down. In order to estimate these effects, the electron beam needs to be characterized.

Electrons emitted by the cathode have a spacial distribution along the cathode radius r_c. Since the cathode is heated to temperatures of T_c, the electron momenta are thermally distributed. Thereby, the electrons have different trajectories depending on their initial conditions. For an estimate of space charge effects the average radius r_0 of the electron beam is most important. This quantity can be approximated by the analytical equation [85]

$$r_0 = \sqrt{\frac{r_\mathrm{B}^2}{2} + \sqrt{\frac{r_\mathrm{B}^4}{4} + \frac{8 m_\mathrm{e} k_\mathrm{B} T_\mathrm{c} r_\mathrm{c}^2}{e^2 B^2} + \frac{B_\mathrm{c}^2 r_\mathrm{c}^4}{B^2 r_\mathrm{B}^4}}}, \tag{3.1}$$

with the Brillouin radius

$$r_\mathrm{B} = \sqrt{\frac{m_\mathrm{e} I_\mathrm{e}}{\pi \epsilon_0 v_\mathrm{z} e B^2}}. \tag{3.2}$$

Equation (3.1) accounts for the initial electron temperature T_c and for an expansion due to electron repulsion depending on the current I_e. The beam is most strongly compressed at the trap center where the magnetic field B is at its maximum. The magnetic field at the cathode B_c can be neglected in since $B \gg B_\mathrm{c}$. The electron velocity v depends implicitly on the electron beam space charge and could in principle be calculated in a self-consistent way. However, a sufficiently accurate approximation of the velocity is given by

$$v_\mathrm{z} = \sqrt{\frac{2eU}{m_\mathrm{e}}}, \tag{3.3}$$

with the potential difference U between the position of the cathode and the trap center.

The radius r_0 can be used to calculate the charge density ρ_e in the trap center. By solving the Poisson-equation

$$\Delta \Phi_\mathrm{sc} = -\frac{\rho_\mathrm{e}}{\epsilon_0} \tag{3.4}$$

inside an infinite tube-shaped electrode, the space charge potential Ψ_sc can be obtained for radii r inside and outside the electron beam:

$$\Phi_\mathrm{sc}(r) = \begin{cases} \frac{I_\mathrm{e}}{2\pi\epsilon_0 v}\left(\frac{r^2}{2r_0^2} - \frac{1}{2} + \ln\left(\frac{r_0}{r_\mathrm{DT}}\right)\right) & \text{for } r \leq r_0 \\ \frac{I_\mathrm{e}}{2\pi\epsilon_0 v}\ln\left(\frac{r_0}{r_\mathrm{DT}}\right) & \text{for } r > r_0 \end{cases}. \tag{3.5}$$

The drift tube radius r_DT enters as boundary condition. The correction obtained from equation (3.5) decreases the electron beam energy by $\Phi(0)_\mathrm{sc}$. Moreover, the space charge $\Phi(0)_\mathrm{sc}$ is responsible for the radial confinement of positively charges ions. An additional effect has to be taken into account as soon as ions were trapped. The positively charged particles compensate the negative electron beam space charge by a factor of

$$f = \frac{\sum_q \rho_\mathrm{q}}{\rho_\mathrm{e}}, \tag{3.6}$$

with positive ion densities ρ_q. The total electron beam energy is determined by the sum of the three potentials:

$$E_\mathrm{e} = e\left(U - (1-f)\Phi_\mathrm{sc}(0)\right). \tag{3.7}$$

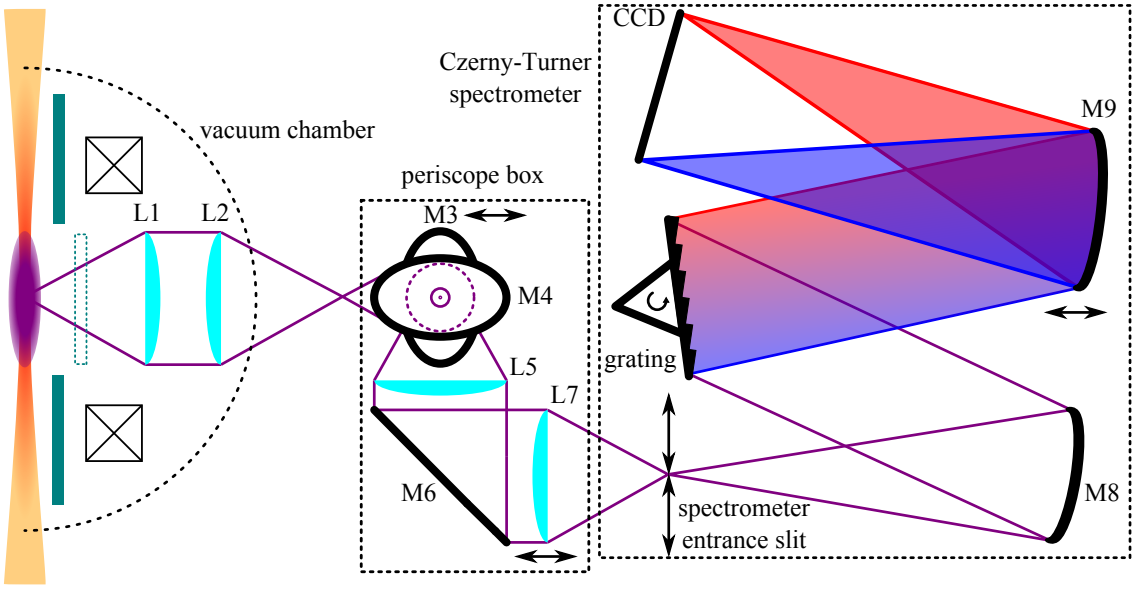

Figure 3.5: Sketch of the optical setup used for the spectroscopy of Nd-like ions.

While $\Phi_{sc}(0)$ can be estimated roughly, the factor $(1 - f)$ strongly depends on the ion species and the trapping conditions. Thereby, the acceleration potential U has to be calibrated. By combining the equations (3.1), (3.3), and (3.5)

$$E_e \approx e\left(U - C\frac{I_e}{\sqrt{U}}\right) \tag{3.8}$$

can be be obtained. The calibration constant C can be measured if the ionization potential of an ion is known. This ionization potential can be used as E_e. If the production of the ion is verified, for example by observing characteristic fluorescence lines, the electron beam energy E_e equals the ionization potential at the threshold. Determining the appearance of a charge state in dependence of I_e and U yields the constant C. For scans along small voltage regions of U the space charge correction is proportional to the current I_e. At large acceleration potentials, the correction becomes less significant. The here-expanded considerations are applied in section 5.3 to identify Nd-like charge states of W, Re, Os, Ir, and Pt.

3.2 Optical setup

The optical setup used for the analysis of the fluorescence light emitted by the ions trapped in the EBIT is sketched in figure 3.5. It can be divided into an imaging system inside the vacuum chamber of the EBIT, and a periscope box to adjust an image of the ion cloud on the entrance slit of a CT spectrometer. Similar setups have been successfully used and presented in [86, 87].

3.2.1 Imaging system and periscope box

An imaging system consisting of plano-convex lenses with diameters of 2.54 cm, L1 and L2, is mounted directly to the heat shield of the EBIT magnet. By this, an intermediate image of the ion cloud in the center of the EBIT is projected through a window to 20 mm outside of the vacuum system. The distance between the ion cloud and the vacuum windows measures 300 mm. By inserting L1 and L2, both with a focal length of 150 mm, the object distance is cut in half, so the solid angle of light collected from the ion can be increased by a factor of four. All transmitting optical elements in the setup are made of fused silica with a transmittance higher than 90% in the wavelength range from 200 nm to more than 1300 nm.

The image outside of the EBIT window is relayed up by a periscope box. It rotates the horizontal ion cloud image by 90° to be aligned with the entrance slit of the CT spectrometer. In that way, the light intensity coupled into the spectrometer is maximized. It is essential that the light incides exactly along the optical axis of the CT spectrometer to optimize the resolution and to avoid imaging errors. Therefore, the ion cloud image is elevated and shifted. The mirror M3 reflects the image 90° in the vertical direction and the mirror M4 rotates the image by reflecting it 90° along the horizontal axis. The light is collimated by the lens L5 and aligned with the optical axis of the spectrometer by the mirror M6. The lens L7 finally projects an image of the ion cloud onto the spectrometer entrance slit. The entrance slit can be closed to a minimum width of 50 µm which is up to a factor of ten smaller than the radius of the ion cloud. Hence, the adjustment and focusing of the ion cloud image is very delicate. Therefore, the mirror M3 has to be translated along the optical axis with 10 µm resolution. Due chromatic aberration of the lenses, the focal plane of the ion cloud image is shifted along the optical axis for different wavelengths. The lens L7 has to be adjusted to correct for that depending on the wavelength range of interest.

3.2.2 Czerny-Turner spectrometer

The light diverging from the spectrometer entrance slit is collimated by the toroidal mirror M8 and reflected towards a dispersive diffraction grating. The grating is mounted on a turret and can be rotated to cover different spectral ranges. The spectral components emerging from the grating are reflected and focused onto a CCD chip by the parabolic mirror M9 to form images of the entrance slit for every spectral line. The CT spectrometer has a total focal length of 550 cm and an focal ratio of $f/6.4$. An advantage of the CT setup is the partial compensation of image aberrations inherent to off-axis reflexions of the light [36]. The light entering the spectrometer expands as circular wave front segment in the horizontal plane. If the wave front is reflected off the toroidal mirror under

an angle the wave front becomes distorted. In a Czerny-Turner setup this distortion is partially compensated by the second reflector. Additionally, the toroidal shape and the small reflection angles reduce the aberrations further in the setup used for this work. Nevertheless, a residual distortion remains. In the ideal case, every point entering the spectrometer through the entrance slit should be focused back on a plane equivalent to the surface of the CCD chip. The residual distortions, summarized as coma and astigmatism, cause the ideal focal plane to become a curved surface meaning spatially distinct points on the entrance slit had different effective focal lengths. In order to optimize the imaging of the entrance slit onto the CCD chip the parabolic mirror M9 can be moved along its normal to adjust the focal length. It is set in a way that the focus is tightest in the vertical center of the chip. The effect of the residual distortion is noticeable in a slight blur and a skew of the images in an instance of the vertical CCD center. These effects could be compensated in the post processing of the recorded CCD images as explained in section 4.2.

3.2.3 CCD camera

The CCD chip consists of 2048 pixel in the dispersive horizontal and 512 pixel in the vertical axis. The total area amounts to $30 \times 8\,\mathrm{mm}^2$ consisting of $13.7 \times 13.7\,\mu\mathrm{m}^2$ pixels. The chip is coated and back-illuminated to enhance the quantum efficiency in the range of 200 nm to 700 nm above 50%. The thermal noise resulting from dark current is reduced to a level of $1\,e^-$/(pixel h) by cooling the chip to liquid nitrogen temperatures. This allows for illumination times on the order of hours. The main source of noise is the readout noise of $3\,e^-$/pixel. The spectral lines appear as projected images of the entrance slit. The wavelength information can be extracted from the horizontal pixel positions of these lines. The information in the vertical axis is used for image corrections and the removal of cosmic ray events. A binning in 8 to 16 stripes was usually applied to the vertical axis.

3.2.4 Blazed diffraction grating

The diffraction grating is the central component of a CT spectrometer. Combined with the geometry of the spectrometer, it determines the dispersion of light into its wavelength components which are imaged, spatially separated, as spectral lines on the CCD chip. A dispersion function has to be found to assign wavelengths to spectral lines.

The diffraction grating is structured as depicted in figure 3.6. The diffraction of the light is described by the grating equation (see [88] for example)

$$\sin\alpha + \sin\beta_\mathrm{n} = Gn\lambda. \tag{3.9}$$

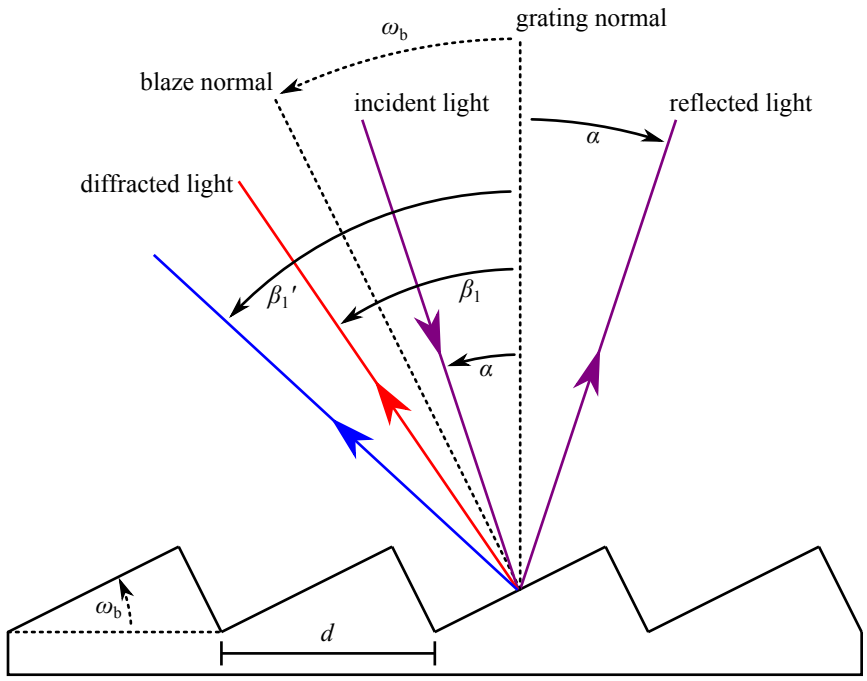

Figure 3.6: Working principle of a blazed grating. Incident light is reflected at an angle α to the grating normal and diffracted at the wavelength dependent angle β. The triangular shape of the grooves enhances enhances the diffraction efficiency for the red beam since the first order diffraction angle β_1 coincides with the reflection angle off the blaze normal, tilted by the blaze angle ω_β.

For the order $n = 0$, incident light with an angle α with respect to grating normal is reflected off the surface as for a mirror independently of the wavelength λ. For higher orders in n, light is diffracted at an angle β_n if the interference condition (3.9) is met for a certain λ. Different wavelengths are diffracted at different angles β depending on the groove density $G = d^{-1}$.

As can be seen in figure 3.6, the grating is grooved at a specified angle with respect to the grating surface. This angle ω_B, called the blaze angle, enhances the reflection efficiency for a certain wavelength range. The blaze ω_B is chosen in a way that the diffraction angle coincides with the reflection angle off the groove surface for this wavelength.

In the experiment, the grating turret is rotated, determining α, to a spectral region of interest. A spectral range depending on G is acquired by the CCD for a fixed α. To calibrate the CCD chip, each pixel p has to be assigned to a wavelength. A function determining the pixel dependence of the wavelength can be obtained by the inverse linear dispersion

$$D(\lambda) = \frac{\partial \lambda}{\partial p} = \frac{\partial \beta_\mathrm{n}}{\partial p}\frac{\partial \lambda}{\partial \beta_\mathrm{n}} = \frac{1}{L_\mathrm{f}(p)}\frac{\cos\beta_\mathrm{n}(p)}{Gn}, \tag{3.10}$$

with equation (3.9). In general, the diffraction angle β_n as well as the focal length of the instrument (L_f) can be functions of p. A calibration function

$$\lambda(p) = \lambda_0 + \int_0^p D(\lambda, p')\mathrm{d}p', \tag{3.11}$$

has to be found for every chosen angle of incidence α. In practice, a polynomial expansion has been performed for equation (3.11)

$$\lambda = \lambda_0 + D_1 p + D_2 p^2 + D_3^3 \ldots \tag{3.12}$$

to the highest statically significant order. The calibration function is fitted with the help of reference wavelengths emitted by a calibration light source. This is explained in more detail in section 4.5.

The spectrometer turret allows for the installation of three different gratings which can be exchanged without opening up the system. For the here presented measurements, two gratings with $G = 300$ lines/mm, for large range scans, and 2400 lines/mm, for high accuracy and resolution, are used. Their blaze angles are chosen for 300 nm and 400 nm, respectively, which allows for reflection efficiencies above 40% for the region 250 nm to 700 nm. The gratings are operated in the first diffraction order.

3.2.5 Calibration source

Well known spectral lines have to be imaged as a references to calibrate the CCD chip. This is achieved by coupling light from an FeAr hollow cathode lamp into the spectrometer. The spectral lines obtained in this way originated from Ar, Ar^+, and Fe and are listed with accuracies on the order of 10^{-5} nm. With this lamp, the spectral range from 220 nm to 600 nm can be covered with reference lines. Their spectral profiles are only negligibly broadened through Doppler broadening compared to spectral lines emitted by HCI in the EBIT. The line shape of calibration lines can therefore be used to characterize the Gaussian spectrometer response function (see Chapter 4).

It is essential to couple the calibration light on the exact same path into the spectrometer as the ion cloud light to avoid systematic uncertainties. This is achieved by a diffuse reflector in front of the entrance to the periscope box that can be inserted and removed from the optical path by a magnet-driven manipulator. The calibration light is brought to the reflector by a fiber light guide. If a calibration measurement is switched on the reflector is pulled in front of the periscope box entrance and blocks the ion cloud fluorescence out. In its place, the light from the hollow cathode lamp is reflected into the periscope box. During ion cloud acquisitions, the calibration light is stopped by a shutter. The calibration source has been build in the course of [87].

Chapter 4

Measurement

The applied identification techniques presented in Chapter 6 put high demands on the resolution and accuracy of the measurements performed in this work. Moreover, the here measured spectral lines will supply data needed for later laser spectroscopy experiments on HCI. To narrow down the frequency scan range for narrow-band spectroscopy lasers, it is important to determine transition wavelengths as accurately as possible. In this Chapter, the necessary steps are explained. For the first installation, the optical setup (see section 3.2) had to be accurately aligned with the center of the EBIT and the internal focusing of the CT spectrometer was optimized. The fine adjustment and the focusing of the ion cloud image on the CT entrance slit depended on the wavelength and was hence optimized before each measurement run. Residual imaging errors, such as aberrations and cosmic ray events, were corrected in the data post processing. At the achieved level of accuracy, even small fluctuations of the room temperature or pressure as well as mechanical instabilities of the spectrometer could cause drifts or other systematic shifts in the pixel position of spectral lines imaged on the CCD chip. Hence, a measurement procedure is presented to prevent these systematic uncertainties. Since the highest resolution and accuracy were the aims of the presented methods, the measurements were performed with the 2400 lines/mm grating if not mentioned otherwise. Nevertheless, the optimization procedures analogously worked for 300 lines/mm grating.

4.1 Spectrometer alignment

The goal of the first alignment step was to ensure that the CT spectrometer was correctly aligned internally in order to maximize signal intensity and resolution. Moreover, the optical axis had to be defined to align the periscope box with the spectrometer and finally with the EBIT. A basic sketch of the alignment setup is shown in figure 4.1. The CT spectrometer was mounted together with the periscope box onto a retractable platform

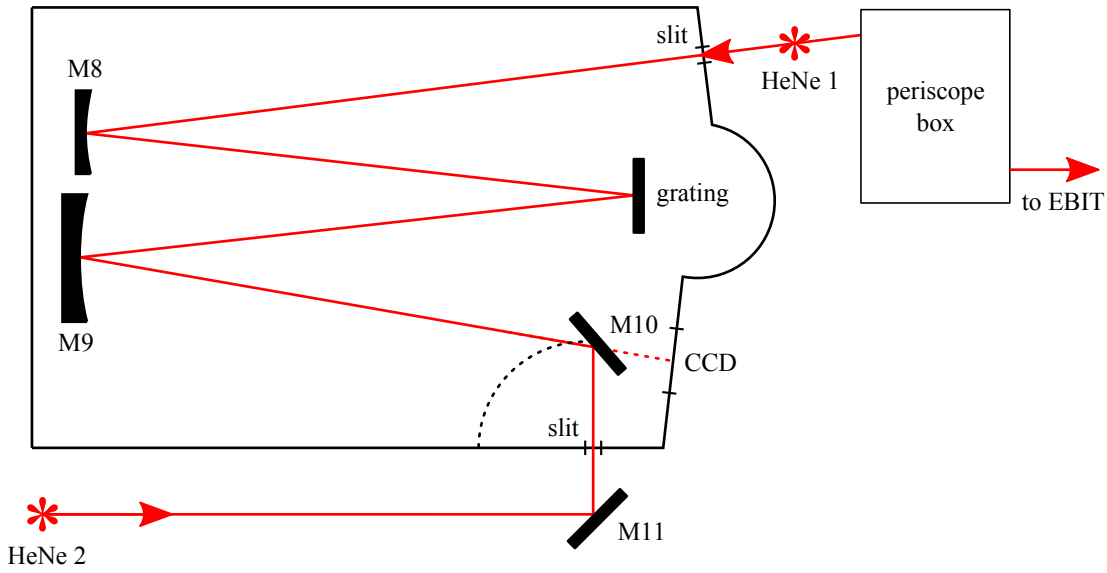

Figure 4.1: Alignment of the optical setup with the EBIT.

on rails. For the alignment procedure the spectrometer was initially pulled back from the EBIT window, and the periscope box was removed. A horizontally oriented HeNe laser was installed in front of the entrance slit and aligned with the optical axis by shining the laser through the 1 mm wide entrance slit onto the center of the toroidal mirror M8 (see figure 3.5), marked by a fixed aperture. The mirror M8, the grating, and the mirror M9 were sequentially adjusted to reflect the beam to the center of apertures in front of each element marking the optical axis.

After checking the internal alignment of the spectrometer, the flippable mirror M10 was rotated into the beam path to reflect it out through a side exit slit, also opened to 1 mm. Via the mirror M11, the beam was deflected onto a second HeNe laser. The second laser was subsequently align to hit the first one after passing through the spectrometer.

Now the first HeNe laser could be removed to proceed with the assembling of the periscope box. Each element (see figure 3.5) was set up to guide the beam centrally to the next one. In order to rotate the the ion cloud image in the experiment by 90°, all mirrors had to reflect the beam precisely within the horizontal plane for M6 and M3, or within the vertical for M4. The proper rotation could be verified through the diffraction pattern of the laser beam imposed on it while passing the spectrometer entrance slit.

As a last step, the beam needed to be aligned with the center of the vacuum window to the trap center. The spectrometer and the periscope box could then be pushed back towards the EBIT, the laser still pointing to the center of the vacuum window. The final position had to be fixed to ensure the stability of the alignment.

4.2 Image correction

For the next optimization steps, the imaging properties of the spectrometer had to be characterized, and remaining aberrations corrected. For this purpose, light from the FeAr calibration lamp was coupled into the spectrometer through the periscope box. Its spectral lines were imaged onto the CCD chip, as shown in figure 4.2.

Spectral lines are wavelength-dispersed images of the spectrometer entrance slit on the chip. The spectra were obtained by integrating the CCD signal along the non-dispersive vertical axis. A high spatial resolution along this axis has thus impact on the spectral quality. However, some spatial information was needed for image correction, as shown below. For most applications the vertical axis of the chip was binned in groups of 32 pixel which reduced the camera read out steps from 1 048 576 pixel to 32 768 pixel. Consequently, a reduction of the read out noise by a factor $\sqrt{32} \approx 5$ was achieved.

Although the vertical axis of the chip was adjusted in parallel to the entrance slit, a slight remaining tilt could be observed when magnifying individual spectral lines. Moreover, residual coma and astigmatism produce a skew on the spectral line. To correct for these errors, the centroids of spectral lines were determined for each of the individual 32 stripes. A correction function was obtained by fitting these centroids with a second order polynomial. All vertical stripes were shifted according to this function to straighten the image.

As can be seen in figure 4.2, the imaged spectral lines were not only skewed but also increasingly broadened in a distance from the chip center. Since most of the line intensity was accumulated in the vertically central part of the CCD, only the center stripes were used for the projection of the intensities onto the dispersive axis. The obtained 1D spectra used for the further analysis exhibited an improved resolution and a symmetrical Gaussian line shape. The same image correction as for the calibration spectra had to be applied to the ion cloud acquisitions in order to obtain the proper wavelengths. Nevertheless, the ion cloud fluorescence was coupled into the spectrometer the same way as the calibration source, and hence the correction function had the same benefits for the ion cloud spectra.

After the line straightening, cosmic muon signals were removed from the image. During typical acquisition times of several minutes, tens of high energetic cosmic muons hit the CCD chip. A muon impact strongly charged a few consecutive pixels. These pixels would have produced a high amplitude noise and thus had to be discriminated. Because muon signatures were relatively strong, they could easily be distinguished from fluorescence photons. An algorithm searches pixels in neighboring vertical stripes for strongly deviating intensities. While the intensity distribution of fluorescence lines form smooth curves along the vertical axis, the muon signals form sharp peaks. If the intensity difference between

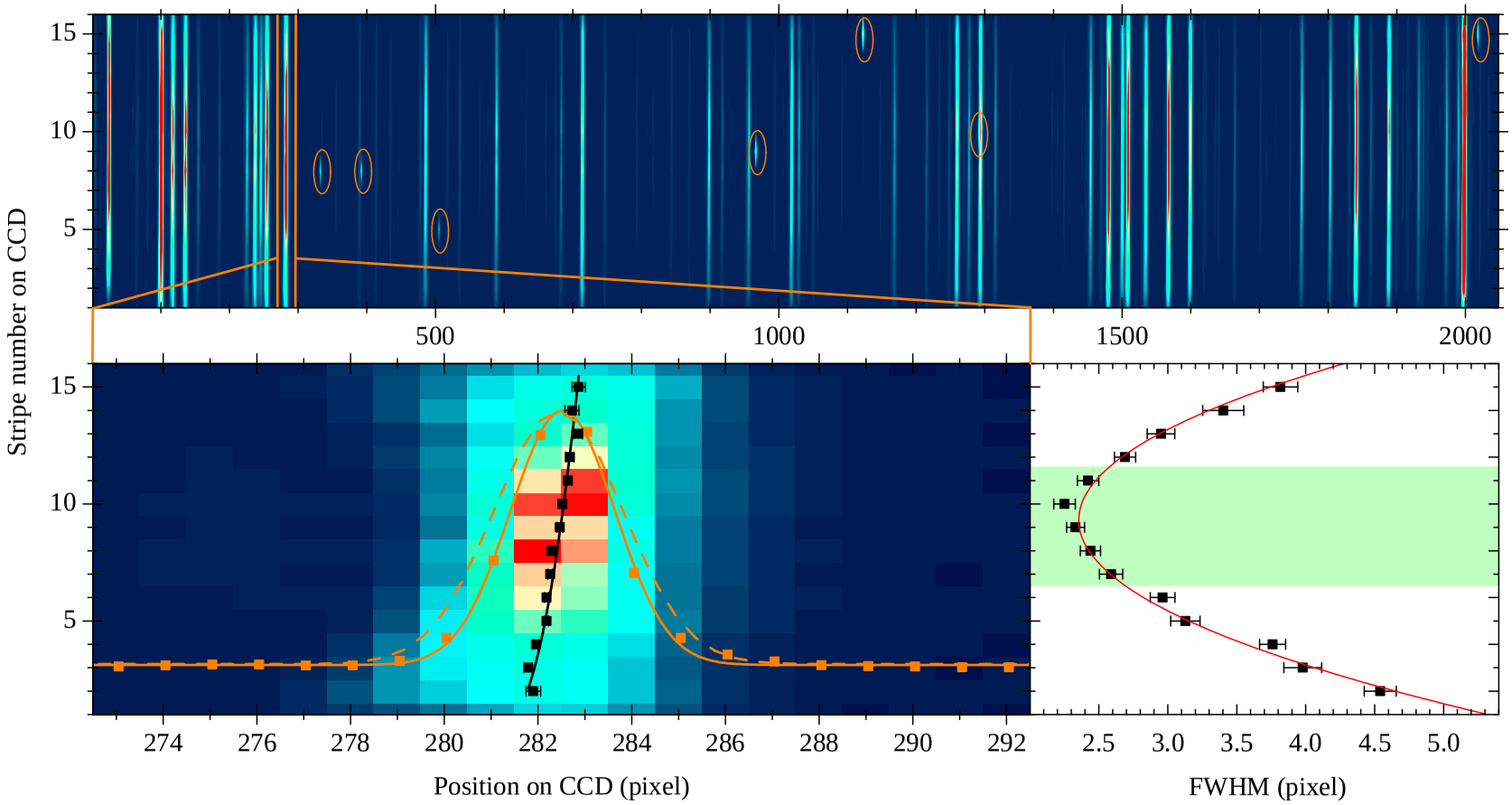

Figure 4.2: Top: CCD image of a calibration spectrum. Cosmic ray events are encircled in orange and removed by an algorithm. Bottom left: Magnified spectral line. The whole image can be corrected by a parabolic function (black line) fitted to the line centroids (black squares). After this correction, the projected CCD image (orange squares) can be fitted by a Gaussian curve (solid orange line), with reduced width compared uncorrected version (dashed orange line). Bottom right: The FWHM parameter of the improved Gauss fit (black squares) reduces towards the center. By fitting a parabolic function (red line), the region with the best resolution (green) is selected for further analysis.

two vertically consecutive pixels exceeds a threshold, these pixels are disregarded for the further analysis. In this way, dead or bright pixels are detected as well.

4.3 Spectral resolution

As shown above, the image of the entrance slit illuminated by the calibration lamp and projected onto the CCD chip produced a Gaussian type line shape in the 1D spectra. Since no Doppler broadening was evident in the calibration lines, their line shape defined the the instrumental response. The width of these Gaussian curves yielded information about the instrumental resolution. The Doppler width of fluorescence lines from trapped HCI could be modeled by quadratically subtracting the the instrumental resolution from the total width [89].

The spectrometer response was optimized after the alignment with the EBIT. The parabolic mirror M9 was moved by a micrometer screw in parallel to the spectrometer side wall to determine the optimal distance to the CCD chip. After a rough adjustment by eye the position of M9 was incremented in small steps. The procedure is depicted in figure 4.3. For every screw setting, the width of one spectral line, produced as described above, was obtained. The ideal position of M9 was determined at the minimum position of a second order polynomial fitted to the measured widths.

4.4 Adjustment of the ion cloud image

Once the spectrometer was set up and aligned with the EBIT and the internal focus was optimized, the previously explained steps did not have to be repeated as long the spectrometer was not been moved. However, several fine adjustments had to be made before starting a measurement series. After each warm-up and cool-down cycle of the EBIT, the electrodes might have contracted slightly differently and the position of the ion cloud could be displaced on a µm scale. More importantly, the plano convex lenses of the coupling optics were susceptible to chromatic aberration. For each spectral range the ion cloud images were projected at different positions. The micrometer screws used for the adjustment of the optical elements were not exactly reproducible, such that the following fine tuning steps had to be repeated before each measurement run.

Firstly, a bright spectral line had to be found at the spectral range of interest by searching different charge states of the trapped ion species while scanning the electron beam energy. The spectrometer entrance slit was opened to 2 mm. For the most spectral ranges a line could be found that could be imaged on the CCD chip with illumination times of a few tens of seconds. The ion cloud image produced outside the vacuum chamber of the EBIT, after L2, was vertically aligned with the entrance aperture of the periscope box

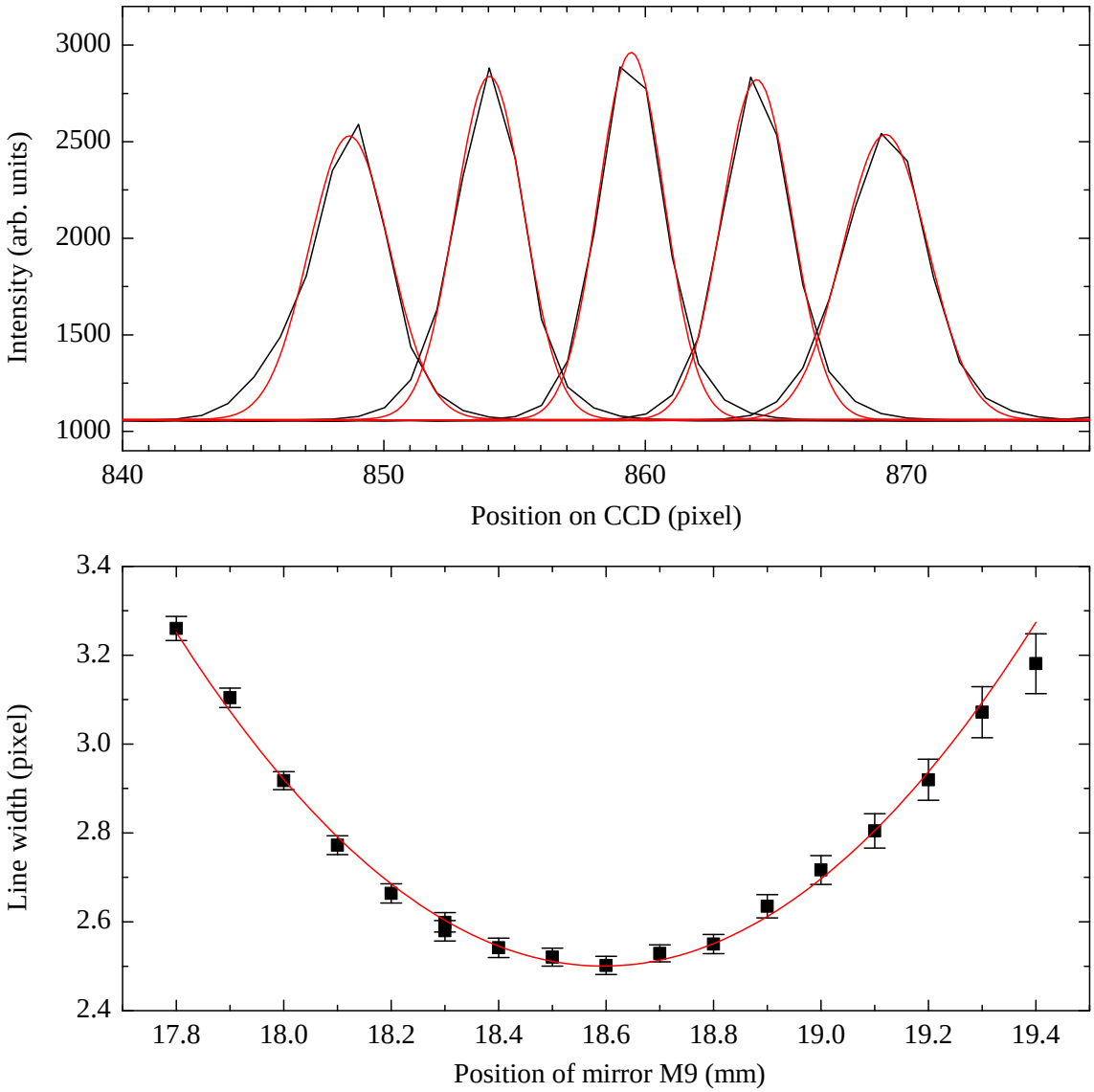

Figure 4.3: Top: Dependence of the spectrometer response on the distance between CCD chip and the parabolic mirror M9. The measured calibration lines are depicted by black lines and fitted by Gaussian functions (red lines). The highest amplitude and the lowest width were obtained for the center peak. Furthermore, a symmetric line shape could only be achieved for an optimal overlap between the focal surface, where the light wave front forms approximately a plane, and the surface of the CCD chip. Bottom: Determination of the ideal micrometer screw setting by finding the minimum of a parabola fitted to the measured Gaussian widths.

by maximizing the light intensity on the CCD. This adjustment also ascertained that the calibration light followed the same path as the ion cloud fluorescence.

Secondly, the ion cloud image was roughly horizontally aligned with the spectrometer entrance slit using M3, again by maximizing the signal intensity. The width of the ion cloud image on the CCD chip was minimized using the lens L7 to achieve optimal focusing of the ion cloud image onto the spectrometer entrance slit.

Thirdly, mirror M3 was used again to fine tune the ion cloud image alignment with the entrance slit. With the entrance slit fully open at a width of 2 mm, the full ion cloud image could be observed if focused correctly. The fluorescence maximum on the CCD marked the position of the ion cloud image. The center position of the entrance slit could be obtained by closing the slit to widths of 50 µm to 70 µm. The signal intensity maximum on the CCD chip then marked approximately the center of the entrance slit. The ion cloud image had to be moved for several iterations until the fluorescence maxima coincided for the opened and the closed slit. The CCD showed an approximate 1:1 image of the ion cloud and the alignment had to be performed with an 10 µm accuracy (approximately 1 pixel).

4.5 Calibration procedure

The spectra obtained from the FeAr hollow cathode lamp were used to calibrate the CCD chip. For that purpose the corrected projections of CCD images were produced as explained in section 4.2. The projection of the image shown in figure 4.2 is plotted in figure 4.4. The lines in these spectra were well represented by Gaussian functions. The brightest spectral lines, 20 to 30 if possible, were fitted for one spectral range. The National Institute of Standards and Technology (NIST) maintained a detailed data base [50] containing most Fe, Ar, and Ar^+ spectral lines abundant in the calibration spectra. By identifying these lines, their centroid positions in pixels could be assigned to their actual wavelengths. The two quantities showed a dependence that is well characterized by a second order polynomial, as motivated in section 3.2.4. This polynomial dispersion function was used for calibration with the linear and the quadratic dispersions D_1 and D_2, respectively.

In order to obtain the calibration function, a set of three lines was searched for that defined a parabola with a linear coefficient D_1 of approximately 0.008 nm/pixel and a quadratic coefficient D_2 less than 10^{-7} nm/pixel^2 for the 2400 lines/mm grating, 0.08 nm/pixel and similar quadratic coefficients and for the 300 lines/mm grating, respectively. Subsequently, as many reference points were added to the fit as possible if they were in agreement with the fit function.

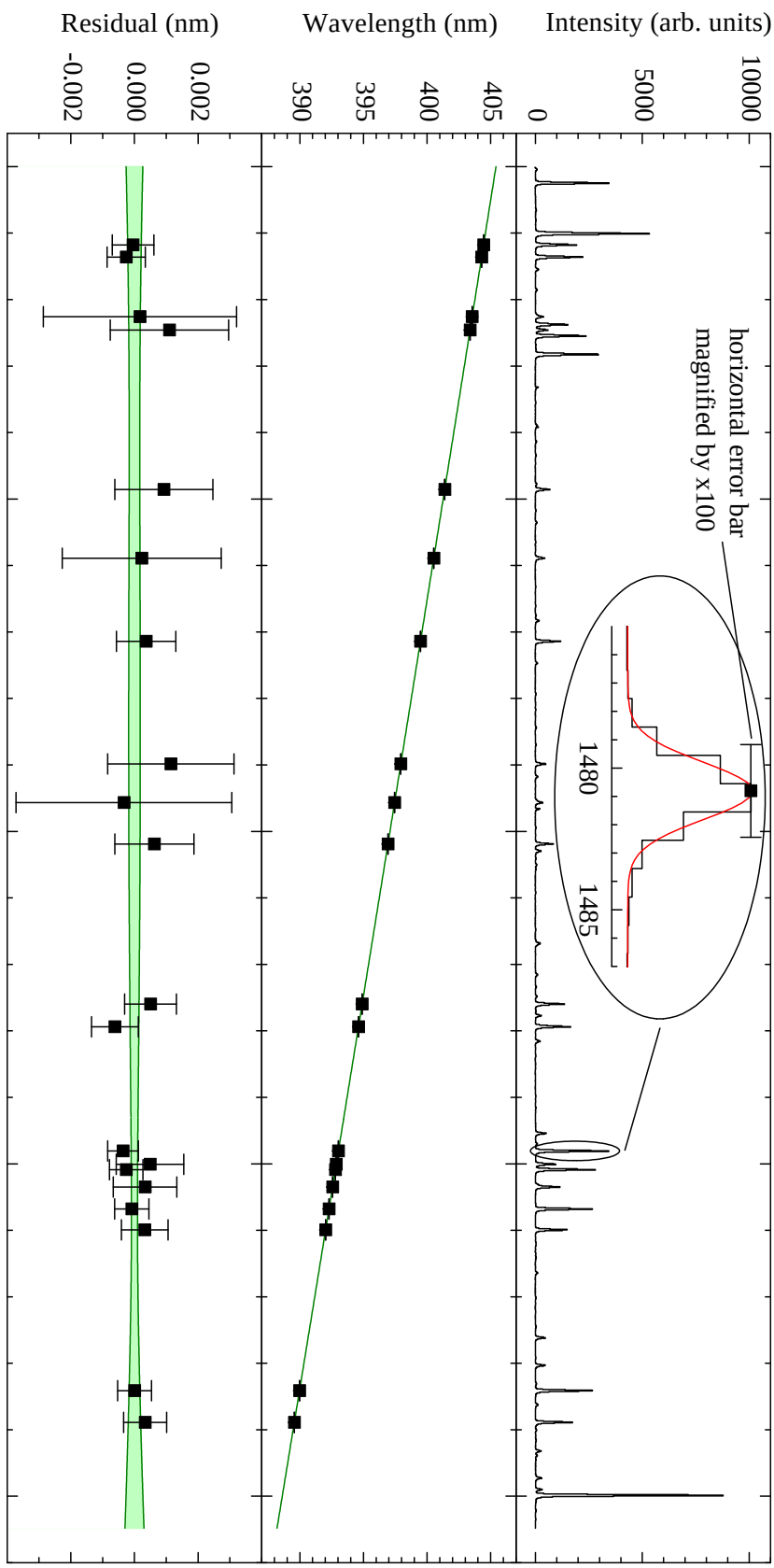

Figure 4.4: Top: Projection of the CCD acquisition shown in figure 4.2. The centroids of the major spectral lines were determined with uncertainties of 10^{-2} to 10^{-1} pixel by fitting Gaussian functions (red line). Middle: 20 of the fitted lines could be identified with the NIST data base (black squares). The calibration function (green line) in this example was determined as $\lambda = 405.4149(3) - 8.2651(7) \times 10^{-3} p - 6.71(3) \times 10^{-8} p^2$. Bottom: Fit residual of the calibration function. The converted fit uncertainties of the Gauss fits overestimate the statistical scatter in this case with a reduced $\chi^2 = 0.37$ with a width of 0.07 of its distribution. The width of the 1σ confidence band (green), between 3×10^{-4} and 1×10^{-4} nm, determines the systematic calibration uncertainty.

The agreement between the reference points and the quadratic model was determined through the statistical uncertainties of the fitted Gaussian centroids. Their pixel uncertainties were translated into wavelength uncertainties by multiplication with the linear dispersion coefficient D_1. Typically, uncertainties of the order of 10^{-4} nm to 10^{-3} nm were obtained. An additional uncertainty of the order of 10^{-5} nm originating from the measurement uncertainties of the reference wavelengths taken from [50] could be neglected. The final reduced χ^2 values of the calibration functions were around one and the residuals scattered statistically, which proved the assumed uncertainties to be correct.

Once the dispersion function for a particular setting is found, no changes were made when switching to ion cloud acquisitions. The calibration delicately depends on all mechanical parameters, such as grating angle, entrance slit width, coupling parameters, and so on. Since most mechanical elements in the spectrometer suffered from measurable hysteresis effects and uncertainties, settings were not fully reproducible. Every ion cloud acquisition needed thus an individual calibration.

The uncertainty of the calibration function added a systematic uncertainty to the wavelength measurement of transitions in the investigated HCI. The calibration uncertainty was estimated through the half width of the 1σ confidence band at the CCD position a HCI spectral line was observed. Usually calibration uncertainties below 10^{-3} nm could be achieved.

4.6 Unit conversions

The measured HCI wavelengths were measured and calibrated in air. For the identification methods applied in Chapter 6, it was required to convert the measured wavelengths to energies. To represent actual transition wavelengths λ_{vac}, the measured air wavelengths λ_{air} had to be corrected for the refractive index $n_{\mathrm{air}}(\lambda_{\mathrm{air}})$ of the ambient air

$$\lambda_{\mathrm{vac}} = n_{\mathrm{air}} \lambda_{\mathrm{air}}. \tag{4.1}$$

The refractive index n_{air} was determined through implementing a standardized formula derived by E. R. Peck and K. Reeder in [90] and recommended by NIST [50]

$$n_{\mathrm{air}} = 1 + 10^{-8} \left(8\,342.13 + \frac{2\,406\,030}{130 - S^2} + \frac{15\,997}{38.9 - S^2} \right) \text{ with} \tag{4.2}$$

$$S = \frac{1000}{\lambda_{\mathrm{air}}}. \tag{4.3}$$

The air wavelength λ_{air} enters the equation in units of nm. The refractive index n_{air} was defined with an atmospheric pressure of 101 325 Pa, a CO_2 content of 33% and an air temperature of 15 °C. Since the all experimental wavelengths were calibrated using air

wavelengths found in the NIST data base and the conversion formula is also used there, no additional uncertainty emerged from this defined unit conversion.

The transition energies E were obtained from the vacuum wavelengths by

$$E = \frac{hc}{\lambda_{\mathrm{vac}}}, \tag{4.4}$$

with the product of the vacuum speed of light c and Planck's constant h. The value of $hc = 1239.84193(3)\,\mathrm{eV\,nm}$ recommended by CODATA [4] is used. The unit conversion could be performed, without adding an uncertainty source since hc is determined at an accuracy of 2×10^{-8}, which was more than an order of magnitude better than the experimental accuracies in this work.

4.7 Data acquisition

A calibration curve was only as accurate as the width of its confidence band as long as it has been ensured that no wavelength drifts or other instabilities occurred between the calibration and the measurement. In order to obtain parts-per-million (ppm) accuracy or better, even small temperature or pressure fluctuations between measurements and calibrations could cause wavelength shifts due to a change of the refractive index of the ambient air (see section 4.6) or length contractions or expansions in the instruments. Moreover, the spectrometer grating could creep slightly after moving it to a new position. These effects are depicted in figure 4.5.

A temperature fluctuation of 1 K or an atmospheric pressure change of 400 Pa would cause a ppm shift of the wavelength [50], translating into a fluctuation of 0.05 pixel. The sinusoidal shape of the measured fluctuation with a period time of 24 h suggested a connection to atmospheric fluctuations, although the observed fluctuation with an amplitude of approximately 0.6 pixel was too high to be explained only by a change of the refractive index of air. Moreover, the different materials used in the optical setup can have large discrepancies in their thermal expansion coefficients, such as the aluminum the spectrometer housing consists of with a linear coefficient of $c = 23.1 \times 10^{-6}\,\mathrm{K}^{-1}$ compared to the fused silica glass of optical components with $c = 0.59 \times 10^{-6}\,\mathrm{K}^{-1}$ [91]. Another interesting effect could be observed in the fit residual of the calibration drift. It exhibited a modulation with a 12 h period which could point towards semidiurnal atmospheric tide cycles [92] but could as well coincide with the control period of the air conditioning system.

As it could be shown that the calibration spectra and ion spectra experienced the same drift, systematic effects could be compensated by frequent calibrations. Therefore, the ion cloud acquisition times were kept as small as possible, usually between 10 min to 20 min, with calibrations performed before and after each ion cloud acquisition. Every

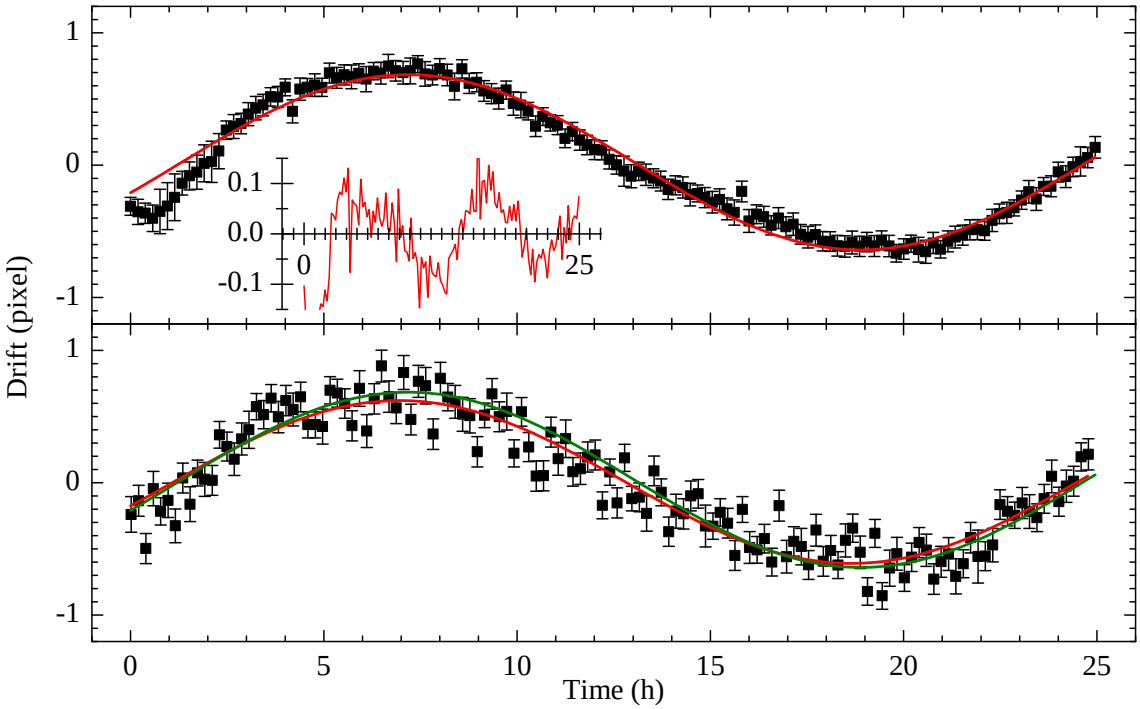

Figure 4.5: Top: Drift of the calibration offset parameter during measurements as a function of time. The measured curve is characterized by a sinus function (red curve) with a period of 23.4(2) h and an amplitude of 0.66(1) pixel. The inlay plot displays the fit residual which shows the presence of a significant contribution with a period half as long. Both graphs indicate a connection to laboratory room temperature changes during the day cycle. Bottom: The drift of a spectral line from trapped ions shows the same functional dependence (red line) as the calibration (green line). The fit yields a period of 23.4(3) h and an amplitude of 0.62(2). No significant phase shift between the curves is evident.

spectrum was calibrated with the average of the two calibrations functions. These cycles were repeated several times to improve the statistics. Even if certain wavelength drifts could not be prevented by this procedure, remaining drifts or outliers in the data could still be detected.

After several of these calibration-measurement-calibration cycles, the grating was rotated by a small angle to shift the spectral range by typically 0.1 nm. This shift prevented systematic effects due possible pixel errors or sensitivity fluctuations associated with certain regions of the CCD chip. The final wavelength value for a high accuracy measurement was determined by averaging over several ten such performed repetitions. Although the measurement procedure worked sufficiently well, it was still important to keep the experimental conditions as stable as possible. Several examples of the measurement procedure are given in the following Chapter 5.

Chapter 5

Results

In this Chapter, the acquired spectroscopic data are presented. Prior to the measurements of Nd-like ions, the instrumental setup as well as the data acquisition and analysis procedure were tested by obtaining the wavelength and the g-factors of the $2p\,^2P_{1/2}$ - $^2P_{3/2}$ transition in the B-like Ar^{13+} ion, as demonstrated with high accuracy in [86, 39, 89]. The investigated W, Re, Os, Ir, and Pt ions were injected into the EBIT as atoms bound in volatile organo-metallic compounds. To prove the successful injection, the transition $3d^4\,^5D_2$ - $^5D_3$ in Ti-like Ir was identified. Its wavelength has been measured in a variety of ions along the Ti-like isoelectronic sequence but for Ir^{55+} has only been interpolated [93]. In this work, the wavelength has been determined with an 100 fold improved accuracy in comparison with the interpolation. By combining this result with other measurements along this sequence, a systematic mismatch between experiment and semi-empirical calculations is confirmed [94]. In the optical wavelength regime and for the moderate charge states of the Nd-like species, neither transition nor ionization energies were known. As described in Chapter 2, theory is not accurate enough predicting these quantities. Consequently, large overview scans in electron beam energy and wavelength were performed, covering tens of charge states with hundreds of transitions, to identify the Nd-like spectra and discriminate spectral features belonging to residual gas elements and other charge states. The brightest spectral lines in Ir^{17+}, and the neighboring charge states, were additionally acquired using the high-resolution and high-accuracy scheme introduced before. A wavelength accuracy down to the sub-ppm level was achieved and the resolved Zeeman structure of these lines are used in Chapter 6 to identify their transitions for the first time.

5.1 The $2p\,^2P_{1/2}$ - $^2P_{3/2}$ transition in the B-like Ar^{13+} ion

The B-like ion Ar^{13+} forms an $1s^22s^22p$ electronic ground state configuration and the fine structure causes an energy splitting of the doublet states $^2P_{1/2}$ and $^2P_{3/2}$. The parity is

the same for both states and the total angular momentum changes by $\Delta J = 1$, hence, the transition is of M1-type. Since approximately half the excited electron population has to decay to the ground state via this transition, the fluorescence photon rate was sufficient to be observed in an EBIT despite a relatively long lifetime of 9.573(6) ms [95]. Its wavelength has been measured in [39] to be 441.2556(1) nm and in other works in good agreement with this value [38, 86, 39, 89, 75]. Sophisticated evaporative cooling combined with an optimized spectrometer resolution allowed to resolve single Zeeman components with a Gaussian line width of 0.023(1) nm [89].

The previous work made the $2p\,^2P_{1/2}$ - $^2P_{3/2}$ transition in the Ar^{13+} ion one of the best characterized HCI transitions, and thus an ideal testing ground for the setup and procedures employed in this work. Since quantities as accuracy and spectral resolution were main figures of merit, the 2400 lines/mm grating was used. The experiments performed by Soria Orts and co-workers were closest to the ones performed in this work and although there are slight differences between this measurement and the one in [89], as expanded upon below, they could be directly compared. A list of comparable quantities is given in table 5.1.

After the initial alignment procedure, as described in Chapter 4, the grating angle was chosen such that the $2p\,^2P_{1/2}$ - $^2P_{3/2}$ spectral line was imaged onto the center of the CCD chip. Figure 5.1 depicts an example calibration spectrum at this grating angle with an Fe-Ar hollow cathode lamp. The CCD image has been corrected for aberrations and projected onto the dispersive CCD chip axis (see Chapter 4). Typically, 20 reference lines were used for the second order polynomial fit, yielding the dispersion function, including most bright spectral lines. All used reference wavelengths taken from [50] were listed with at least an order of magnitude higher accuracy than the line position on the CCD. Hence, the uncertainties of the line positions, as inferred from the uncertainties of their Gauss fits, explained the statistical scatter sufficiently well with a reduced $\chi^2 = 1.0(3)$. The numbers in brackets next to the reduced χ^2-values indicate the standard deviation of their

Table 5.1: Comparison of parameters of the $2p\,^2P_{1/2}$ - $^2P_{3/2}$ transition in B-like Ar measured in [89] to this work.

	Orts *et al.* [89]	This work
Electron beam current	50 mA	40 mA
Magnetic field strength	6.820 T	8.000 T
Entrance slit width	50 µm	70 µm
Spectrometer response	3.2 pixel	3.0(1) pixel
Wavelength	441.2556(1) nm	441.2552(7) nm
Spectral line width w	0.331(1) nm	0.331(1) nm
$^2P_{1/2}$ g-factor	0.663(7)	0.643(7)
$^2P_{3/2}$ g'-factor	1.333(2)	1.305(6)

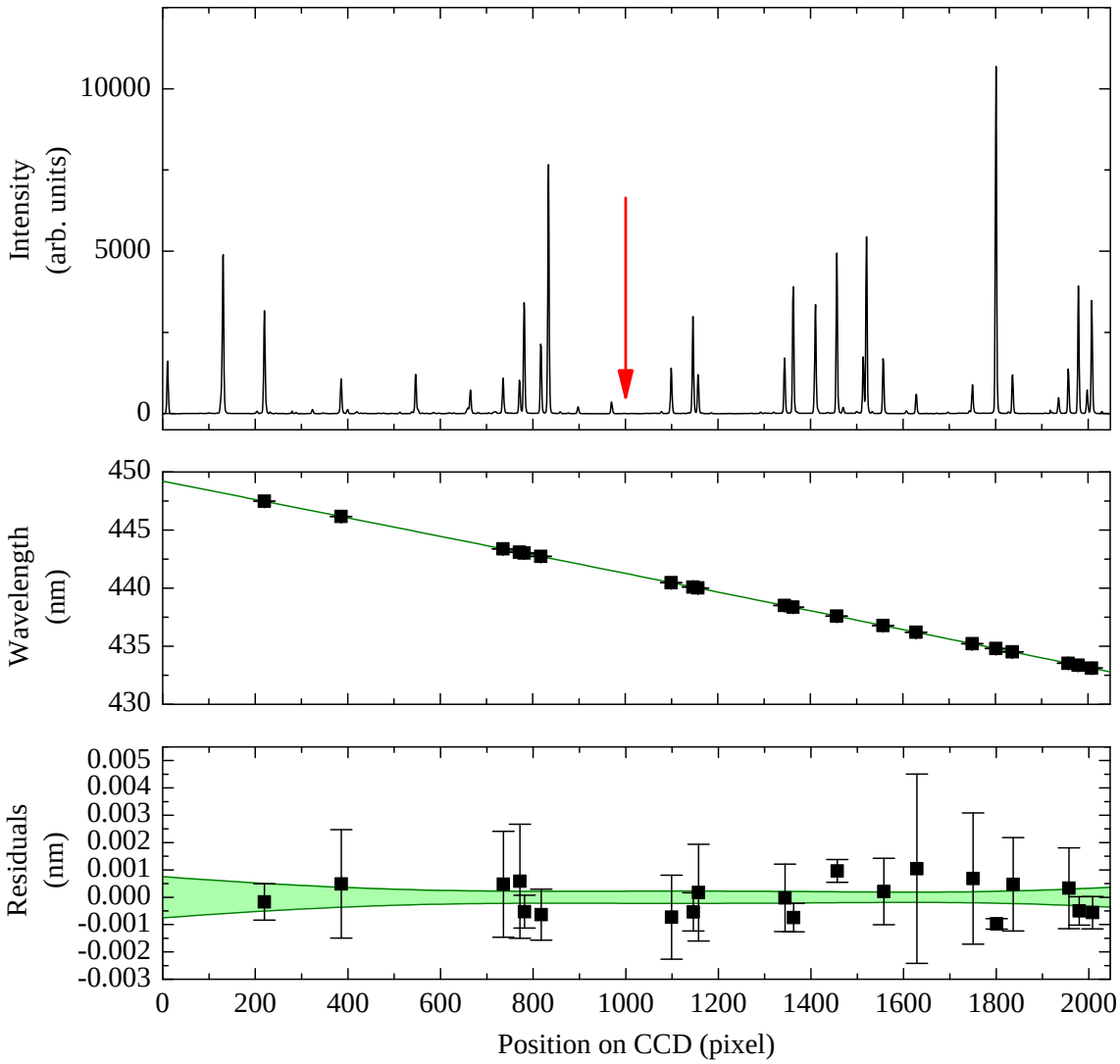

Figure 5.1: Calibration used for the $2p\,^2P_{1/2}$ - $^2P_{3/2}$ transition in B-like Ar. Top: Calibration spectrum generated by a Fe-Ar hollow cathode lamp around the expected pixel position of the $2p\,^2P_{1/2}$ - $^2P_{3/2}$ transition corresponding to 441.3 nm (red arrow). Middle: Quadratic dispersion function (green line) fitted to the identified FeI and ArI-II transitions (black squares). The assigned wavelength references are taken from [50]. Bottom: Fit residuals (black squares) and uncertainties in the centroids of the calibration lines (error bars)($\chi^2 = 1.0(3)$). The 1σ confidence band for the fit function is shown in green.

distribution. As can be seen in the residual plot (figure 5.1), the width of the 1σ confidence band of the calibration function contributed a systematic uncertainty of 2×10^{-4} nm to the final wavelength uncertainty of the $2p\,^2P_{1/2}$ - $^2P_{3/2}$ transition.

Pure ^{40}Ar was injected by connecting a pressurized gas bottle to the injection system. The injection pressure in the first differential pumping stage was controlled by a variable

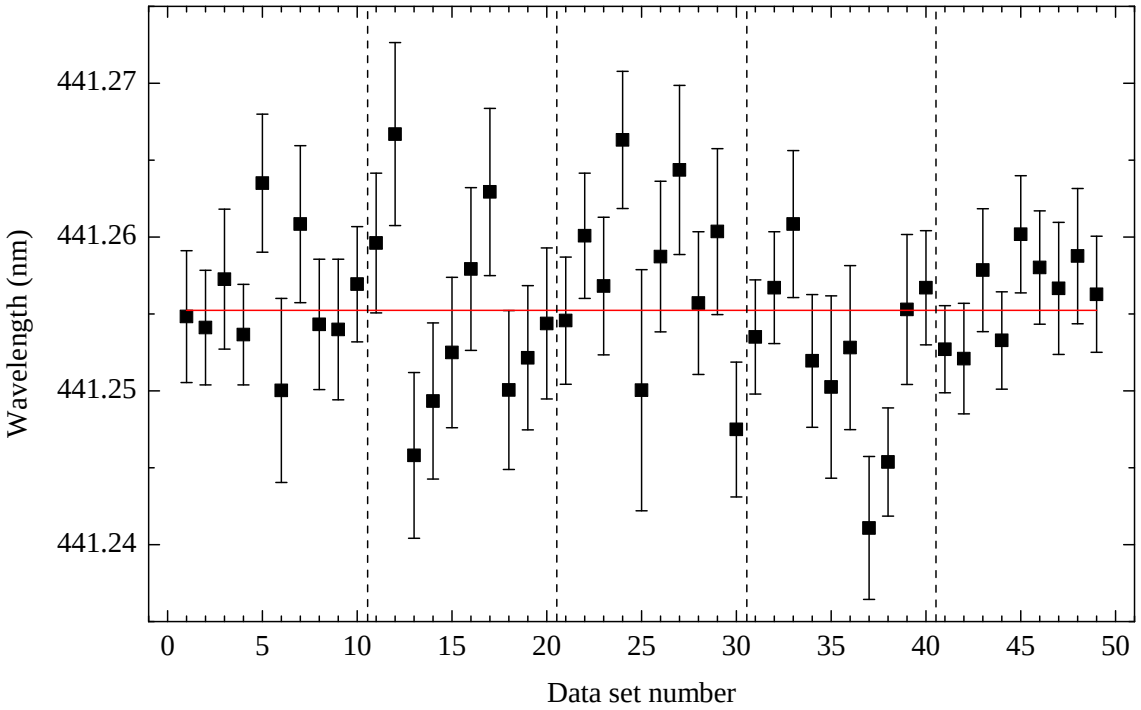

Figure 5.2: Average over 50 acquisitions of the $2p\,^2P_{1/2}$ - $^2P_{3/2}$ transition in B-like Ar. After ten acquisitions, (dashed line) the grating is slightly rotated such that the spectral line is imaged onto different areas of the CCD chip to avoid systematic uncertainties due to sensitivity fluctuations of pixels. The fit uncertainty (error bars) seems sufficient to explain the statistical scatter of data points ($\chi^2 = 1.27(20)$).

leak valve to approximately 1×10^{-8} mbar. A strong $2p\,^2P_{1/2}$ - $^2P_{3/2}$ fluorescence signal was achieved by setting the EBIT acceleration potential to 820 V, well above the Ar^{13+} ionization potential of 755 eV [50], at an electron beam current of 40 mA. As described in Chapter 4, calibration spectra were taken before and after each ion cloud acquisition and their average dispersion function was used to calibrate one Ar^{13+} spectrum. After ten calibration-measurement-calibration cycles, the grating was rotated to shift the spectral range by 0.02 nm, which translated approximately to 2-3 pixel, and another ten repetitions were performed. By this measurement procedure (see section 4.7), systematic wavelength drifts could be avoided as well as uncertainties due intensity fluctuations on certain CCD areas. For the wavelength determination, the mean and standard deviation of 40 centroids at five different grating angles were used, as presented in figure 5.2. The centroid uncertainties characterized the statistical scatter sufficiently well ($\chi^2 = 1.27(20)$) and neither systematic shifts nor discontinuities were evident. The mean value was 441.2552(7) nm, in perfect agreement with 441.2556(1) nm [89]. The main uncertainty contribution was the statistical uncertainty of the mean, which could be reduced further by performing more repetitions, as much as several hundreds more to approach an accuracy as reported in [89].

In figure 5.3, the average of all individually calibrated Ar^{13+} spectra is plotted. The Zeeman splitting of the $2p\,^2P_{1/2}$ - $^2P_{3/2}$ transition could be observed with a line width of 0.031(1) nm which is identical to the one in [89] obtained with an electron beam current of 50 mA. Although the reduced current used here results in a reduced Doppler width due to less electron collisions and thus heating of the trapped ions, this effect was too small to be observed. Because transitions could be significantly weaker in the aimed-for Nd-like HCI compared to the Ar^{13+} test ion, a spectrometer entrance slit width of 70 µm was chosen, instead of 50 µm as in [89]. By increasing the slit width by this amount, the detection efficiency, important for the weaker spectral lines, could be enhanced without significantly impairing the spectrometer response defined by the mean FWHM of the calibration lines (see table 5.1).

A further important test was performed using the Zeeman pattern of the $2p\,^2P_{1/2}$ - $^2P_{3/2}$ transition caused by the magnetic field at the trap center in the EBIT. The g-factors of the involved levels could be extracted through the energy separation between the different Zeeman components. In [89], an accuracy of parts-per-thousand has been achieved by an optimized the linewidth of 0.023(1) nm at a reduced electron beam current of 20 mA. Moreover, the σ and π polarizations could be imaged separately by using a polarizer in front of the spectrometer entrance. Due to the reduction in signal strength, a lower beam current was not feasible for measurements of Nd-like ions, but instead an increased magnetic field strength of 8.000 T (compared to 6.820 T) led to a similar separation of the Zeeman components. For Nd-like ions much higher total angular momenta, up to $J = 6$, could be observed and thus a larger and denser manifold of Zeeman components, which generally could not be resolved individually (see Chapter 6). In these cases, the use of a polarizer would not have had a large impact on the accuracy of the g-factors, but had cost additional measurement time which could not be afforded because of the large number of measurements that had to be performed. Rather, the applicability of the model introduced in equation 2.52 is demonstrated, which fits any number of Zeeman components. The resultant g, g'-factors had a similar statistical uncertainty as compared to [89] but seemed systematically lower. This could be explained by a marginal loss of electric current in the superconducting magnet coils over time on the order of 1 % per week.

The Ar^{13+} measurements presented above validated the experimental setup, the data acquisition scheme, and the analysis method. With an emphasis on the capability to measure large numbers of weakly fluorescing transitions as accurately as possible in the given time, minor compromises on the spectral resolution had to be made. However, ppm accuracies were achieved and systematic effects were understood and neutralized. The g-factor model recreated the shape of the $2p\,^2P_{1/2}$ - $^2P_{3/2}$ transition and yielded correct g-factors. By inverting the process and inserting calculated g-factors into the

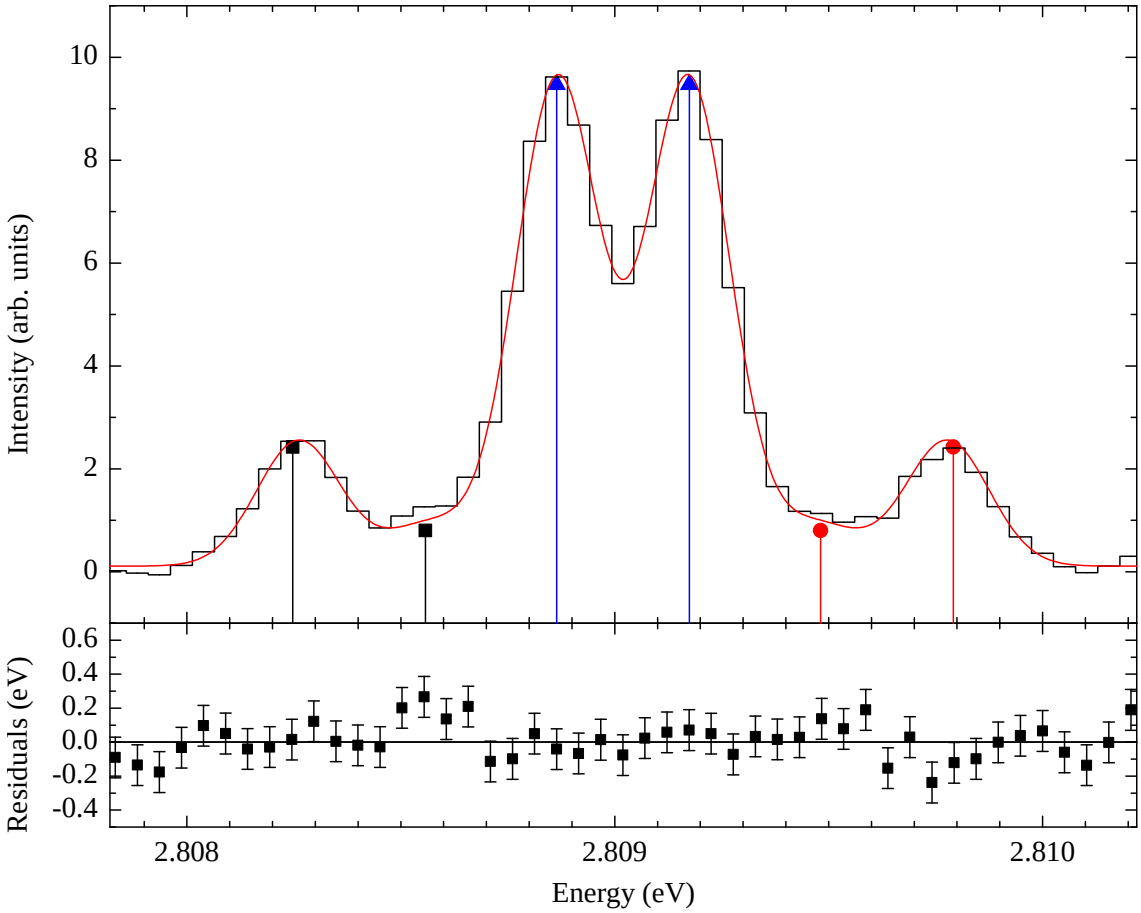

Figure 5.3: Top: Averaged Ar^{13+} spectrum (black) around the energy of the $2p\,^2P_{1/2}$ - $^2P_{3/2}$ transition at 2.80902 eV (corresponding to an air wavelength of 441.2552 nm). The data is fitted with the g-factor model (red) (see equation 2.52). The calculated energies of the Zeeman components are depicted by symbols (black squares $\Delta m = -1$, blue triangles $\Delta m = 0$, red circles $\Delta m = +1$). Bottom: Fit residuals (squares) with the standard deviation of the noise histogram as error bars which characterize the model deviation ($\chi^2 = 0.94(13)$).

model, a powerful tool for the identification of unknown transitions could be obtained as demonstrated in Chapter 6.

5.2 The $3d^4\,^5D_2$ - $^5D_3$ transition in the Ti-like Ir^{55+} ion

Unlike the $2p\,^2P_{1/2}$ - $^2P_{3/2}$ transition in B-like Ar, Nd-like W, Re, Os, Ir, and Pt were completely uncharted. Without experimentally verified knowledge of transition energies or ionization potentials, no orientation points were given. Hence, as a first step it had to be assured that the elements of interest were successfully injected and their desired charge states produced and trapped in the EBIT, as described in Chapter 3. To this

end, advantage was taken of the fact that a wide Z-range of Ti-like ions, including Ir^{55+}, exhibit the optical transition $3d^4\,{}^5D_2$ - ${}^5D_3$, which is of particular interest regarding the fine-structure scaling with Z discussed in Chapter 2. For this reason, the $3d^4\,{}^5D_2$ - ${}^5D_3$ can potentially be important for plasma diagnostics and it has been measured for example in Ti-like W, Yb, and Bi in [93]. Although Ir^{55+} was not covered by this survey, an interpolation gave an estimate of the $3d^4\,{}^5D_2$ - ${}^5D_3$ transition wavelength of 357.4(8) nm [93]. This estimate was accurate enough to identify this transition once it was observed.

The measurement was performed analogously to the previous one in B-like Ar (see figure 5.4). In this case, the main challenge was to produce Ir^{55+} at high quantities in order order to obtain a sufficiently strong fluorescence signal. The ionization potential was calculated to be 5229 eV [50], so the electron beam acceleration potential was set approximately 1 keV higher. At these high energies an electron beam current of 168 mA could be reached. Nevertheless, the received signal was extremely weak (see figure 5.5) so that single acquisitions had to be set up for 2 h illumination times and the spectrometer entrance slit was opened to 100 µm to increase the SNR. Thereby, the spectrometer response diminished to a value of 5.9(7) pixel, too high to resolve Zeeman splitting. For the average of 14×2 h acquisitions, a wavelength value of 357.432(3) nm was obtained (see figure 5.6). The fit uncertainties for the single acquisitions underestimated the total scatter of the data quantified by a reduced $\chi^2 = 2.1(4)$. This was most likely because of the long illumination times and therefore a lack of intermediate calibrations. However, the data points did not deviate from a random distribution around the mean, thus, the full scatter was characterized by the standard deviation of the mean of 0.003 nm. Compared to this, other sources of uncertainty were negligible as for example the calibration uncertainty with a value of 5×10^{-5} nm.

With this observation, not only the successful injection could be verified but another data point for the $3d^4\,{}^5D_2$ - ${}^5D_3$ transition wavelength in the Ti-like isoelectronic sequence has been added with a high accuracy compared to similar experiments. Thereby, a trend could be confirmed suggesting a linearly increasing mismatch between *ab initio* calculations and experiments above $Z = 72$ [94].

5.3 Broad-band spectra of W, Re, Os, Ir, and Pt around the Nd-like isoelectronic sequence

For the moderate charge states like Nd-like W, Re, Os, Ir, and Pt, the differences in ionization energies between neighboring charge states amount to approximately 20-60 eV. The complex space charge effects, as explained in Chapter 3, impeded a determination of the electron beam energy on that level of accuracy. This posed the risk of missing the desired charge state. Moreover, the ionization potentials were only known from calcula-

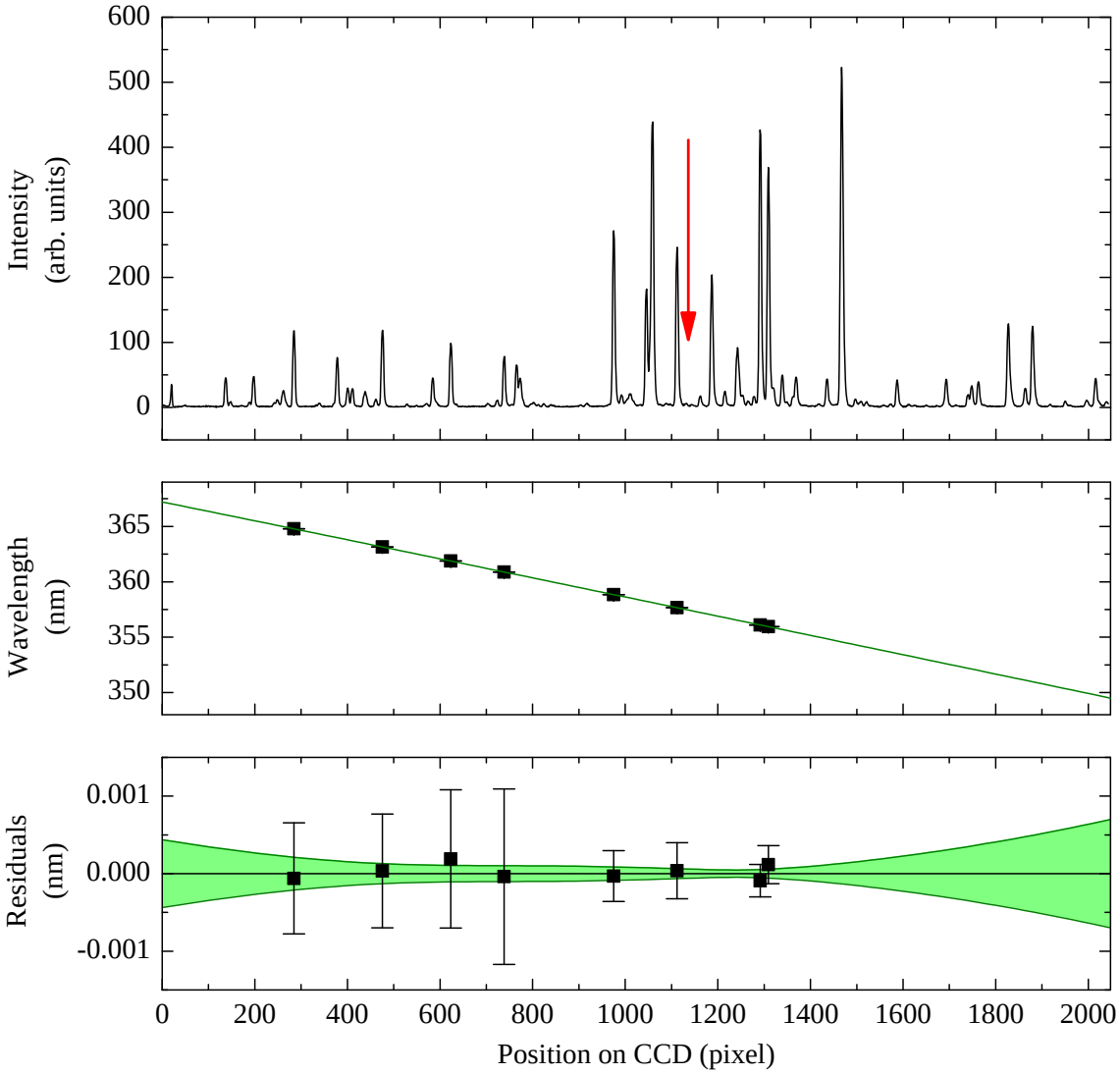

Figure 5.4: Calibration used for the $3d^4\,{}^5D_2$ - ${}^5D_3$ transition in Ti-like Ir. Top: Calibration spectrum generated by a Fe-Ar hollow cathode lamp around the expected pixel position of the $3d^4\,{}^5D_2$ - ${}^5D_3$ transition corresponding to 357.4 nm (red arrow). Middle: Quadratic dispersion function (green line) fitted to the identified FeI and ArI-II transitions (black squares). The assigned wavelength references are taken from [50]. Bottom: Fit residuals (black squares) and uncertainty in the centroid of the calibration lines (error bars). The 1σ confidence band for the fit function is shown in green ($\chi^2 = 0.1(6)$).

tions, hence, their uncertainties could only be estimated to be at a level of several eV. As explained in section 2.4.1, due to the constant injection of neutrals, HCI could not be prepared in a single charge state in an EBIT but rather as a distribution of charge states. Once the population of ions in a certain charge state was optimized, there was still a significant contribution to the fluorescence signal from ions of neighboring charge states. In order to identify the desired charge state, to optimize the electron beam energy

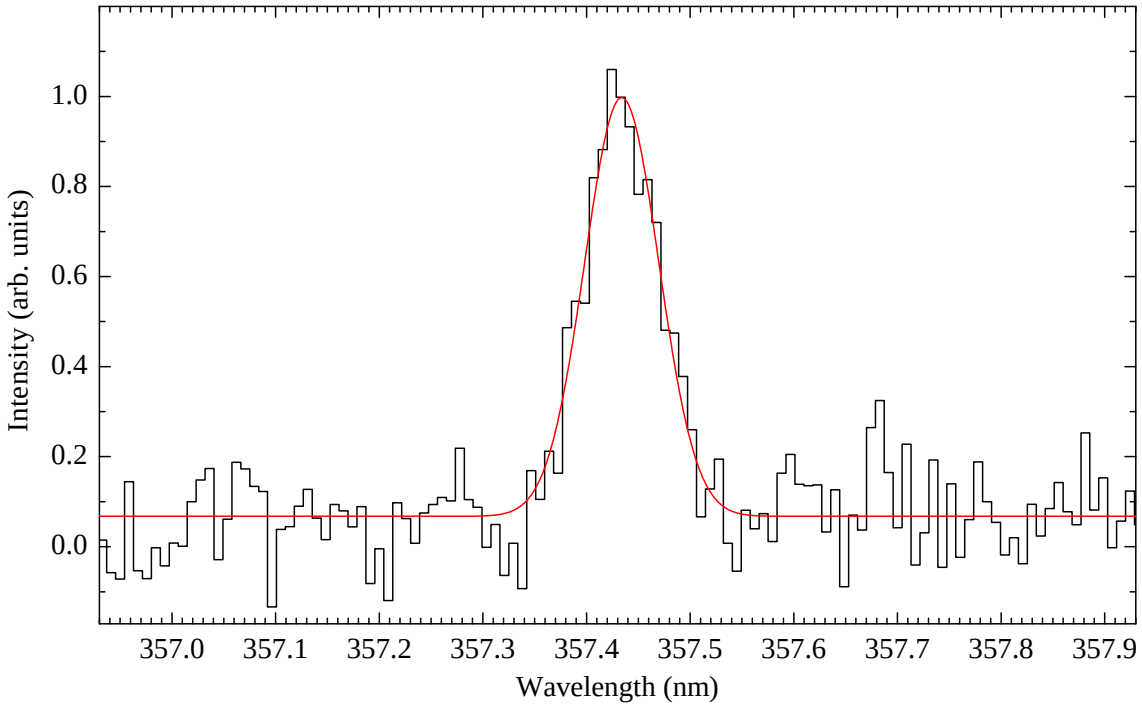

Figure 5.5: Average spectrum composed of 14 individually calibrated (see figure 5.4) ion cloud acquisitions. The displayed $3d^4\,{}^5D_2$ - ${}^5D_3$ line (black) is fitted with a Gaussian curve (red). For the actual wavelength determination, the centroids in the individual acquisitions are weighted by their fit uncertainties and averaged (see figure 5.6).

for the maximum fluorescence yield, and to discriminate spectral features emerging from other charge states, broad scans of both the electron beam energy and spectral range have been performed.

By exchanging the 2400 lines/mm grating with a 300 lines/mm grating, the spectral range imaged onto the CCD chip at one grating angle could be increased by a factor of eight, from linear dispersions of typically 0.008 nm/pixel to 0.08 nm/pixel, which allowed to cover the relevant wavelength band in a reasonable amount of measurement time. The calibration procedure worked analogously to the measurements with the 2400 lines/mm grating. For the 300 lines/mm grating, typically larger entrance slit widths of 200 µm were used to optimize on the fluorescence detection efficiency, leading to a wavelength uncertainty of 0.02 nm. After one exposure for a typical duration 15 min to 30 min at one electron beam energy, the acceleration potential was increased by 10 V. In case of W, for which the expected separation between neighboring charge states was smallest, the steps were reduced to 5 V. By plotting the acquired spectra against their acceleration potential, a 2D map as in figure 5.7, could be assembled. Through projecting the fluorescence intensity of the mapped spectral lines onto the acceleration potential axis, they could be pooled in groups exhibiting the same energy behavior. They, thus, belong to the same charge

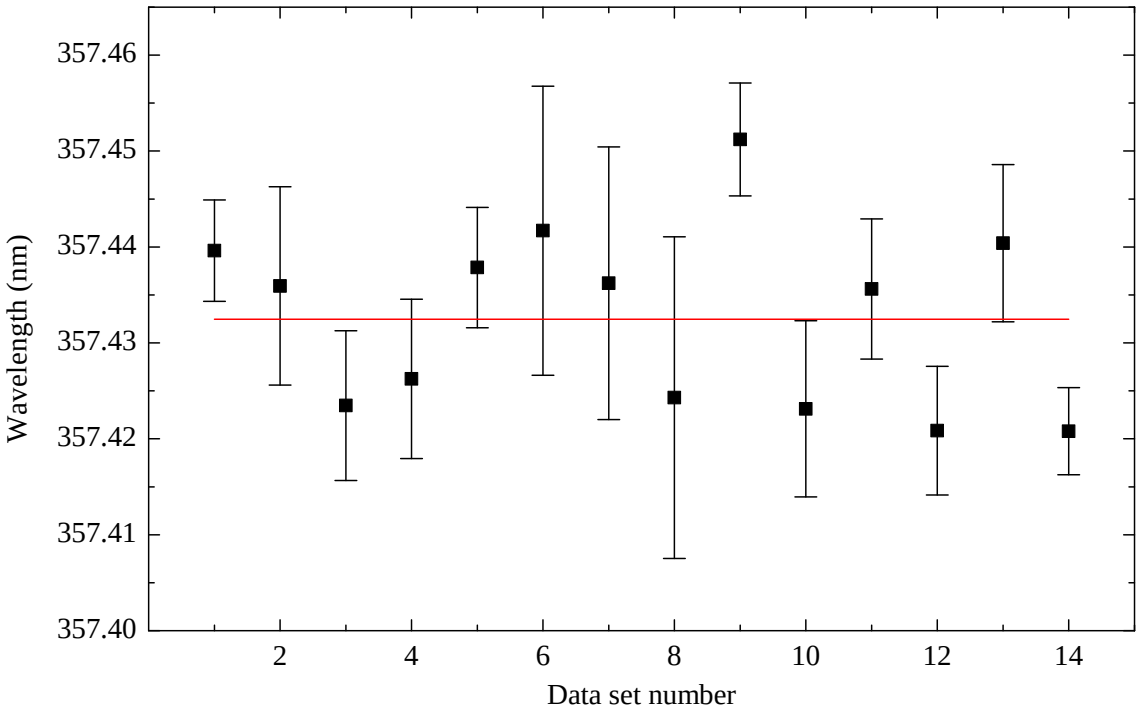

Figure 5.6: Individually evaluated wavelengths of the $3d^4\,{}^5D_2$ - ${}^5D_3$ transition in Ti-like Ir (black squares). The weighted average (red line) of all 14 values yields a wavelength of 357.432(3) nm ($\chi^2 = 2.1(4)$)

state. The optimum spectrum for a certain charge state was obtained at the acceleration potential corresponding to the maximum of its intensity curve (see right hand side of figure 5.7). It is notable that all such spectra contained a significant amount of spectral lines at least from the next neighboring charge states, but these could easily be distinguished with the produced 2D maps.

Each intensity curve in figure 5.7 represents one charge state in Ir preliminary labeled with place holders for the charge number from (A-5) to G. The shape of these curves could be understood by considering three consecutive charge states, for example A, B, and C. The intensity curve B typically started to raise steeply as soon as the electron beam energy exceeded the ionization energy of A. Due to an increasing ionization cross section (see equation 2.31), the population grew until the electron beam energy reached the ionization energy of B. At this point the intensity curve B maximized and started to drop again since population was transferred from B to C. Indeed, each curve maximum in figure 5.7 marks the beginning of the succeeding charge state. This fact ensured that each charge state is represented by at least one spectral line and no intermediate states have been missed out.

As expanded upon in section 3.1.5, to determine the electron beam energy $E_\mathrm{e} = U_\mathrm{acc} - U_\mathrm{c}$, the acceleration potential U_acc needed to be corrected by the space charge

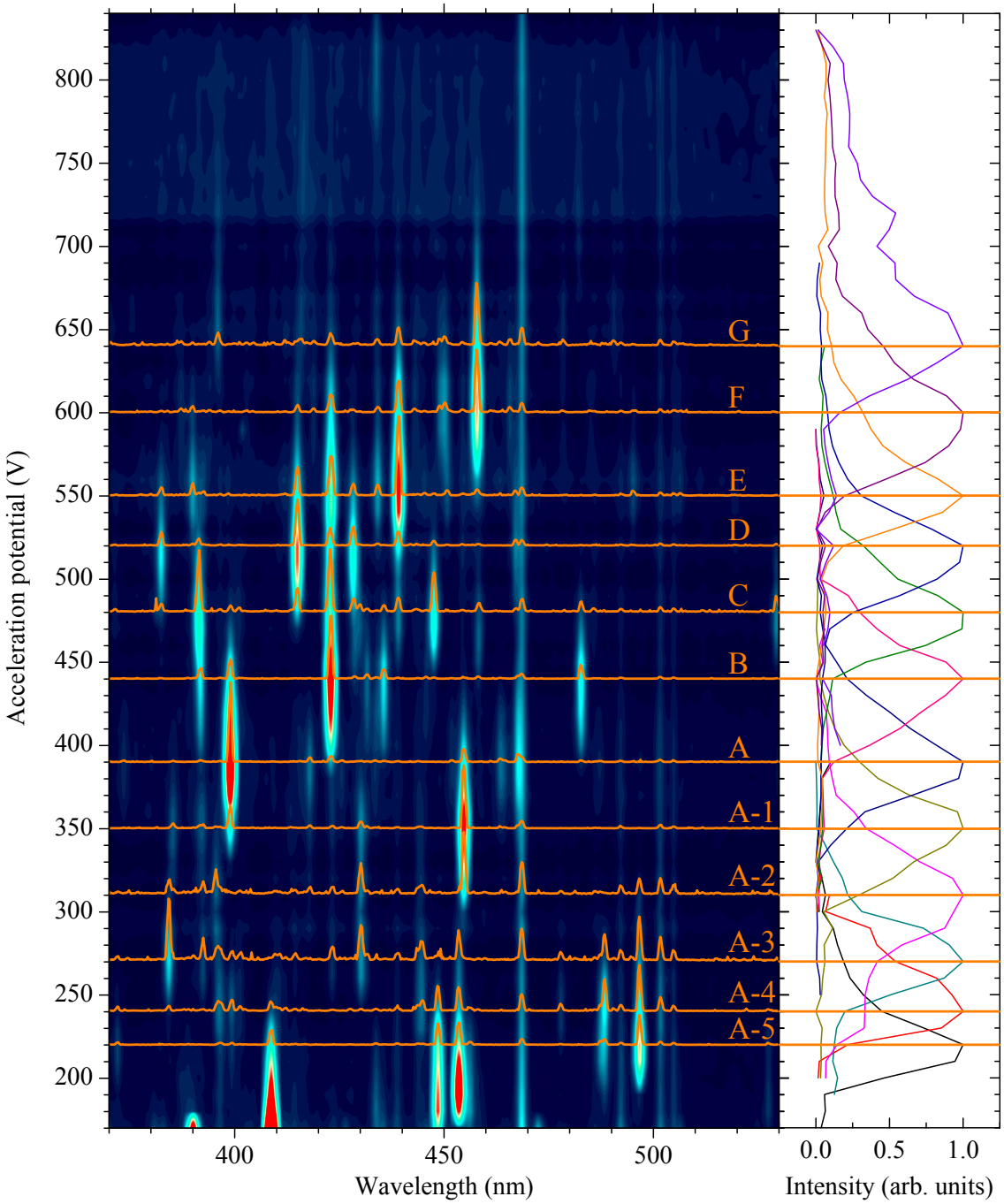

Figure 5.7: Left: Spectral map of Ir charge states as a function of the uncorrected acceleration potential. Spectra are acquired while the acceleration potential is raised in steps. Groups of spectral lines that show the same energy dependence belong to the same charge states preliminarily labeled with letters. The orange lines mark the spectra at the fluorescence maximum for each charge state. The constant features (as at 469 nm) stem from residual gas ions. Right: By projecting the intensity of all lines onto the acceleration potential axis, the energy dependent intensity curves are obtained. These curves are used for the charge state identification in figure 5.8.

potential U_c of the electron beam and stored ions in the EBIT. As a valid first order order approximation, it could be assumed that $U_c \approx CI_e$, where I_e is the electron beam current, which was kept constant during a measurement. To determine C, Fe was injected as a reference simultaneously with Ir, setting $I_e = 10\,\mathrm{mA}$ as for the measurement presented in figure 5.7. The ionization energies of multiply charged Fe have been accurately calculated and its transitions are relatively well known [50, 96]. In figure 5.8 for example the green coronal line in Fe^{13+} [97] was imaged together with an IrC transition. The start of the Fe^{13+} intensity curve already coincided with the calculated ionization energy of Fe^{12+} at 361 eV [50], so $C = 0$ which means the negative electron beam space charge potential was nearly completely compensated by the positive potential of trapped Fe and Ir ions. Since the cross sections of electron impact ionization of the various charge states in this range increased in equal measures with energy, the width of the rising flanks (see figure 5.7) was taken to be a constant established to be 31 eV as in case of Fe^{13+}. The maxima could be obtained more accurately than the starting points. Therefore, the ionization energies were defined by the energy at the maximum minus 31 eV. The ionization energy of IrC was determined and the intensity curves arising from figure 5.7 could be offset to fit with it. In table 5.2, the obtained experimental ionization energies were compared with FSCC [59] and CIDFS [62] calculations (see Chapter 2).

The best agreement between prediction and measurement was achieved by assigning IrA to Ir^{16+}, IrB to Ir^{17+}, IrC to Ir^{18+}, and so on, with a mean deviation of 8 eV. By shifting this assignment such that IrC is Ir^{17+}, the mean deviation would amount to −33 eV. While the calculations agreed well with each other, there were strong discrepancies between data

Table 5.2: Comparison of experimentally determined and calculated ionization energies in eV. The ionization energies are derived by subtracting 31 eV from the energy at the peak position of the intensity curves. Uncertainties in the determination of the experimental ionization energies are conservatively estimated at 5 eV.

Ir charge state	Ionization energy		
	Experiment	FSCC [59]	CIDFS [62]
11+	–	–	233.5
12+	228	–	254.8
13+	270	295.4	293.5
14+	313	320.0	317.5
15+	346	373.7	371.4
16+	400	408.3	405.7
17+	433	434.8	432.2
18+	475	471.5	469.4
19+	509	512.1	510.1
20+	557	558.2	554.9
21+	601	603.1	–

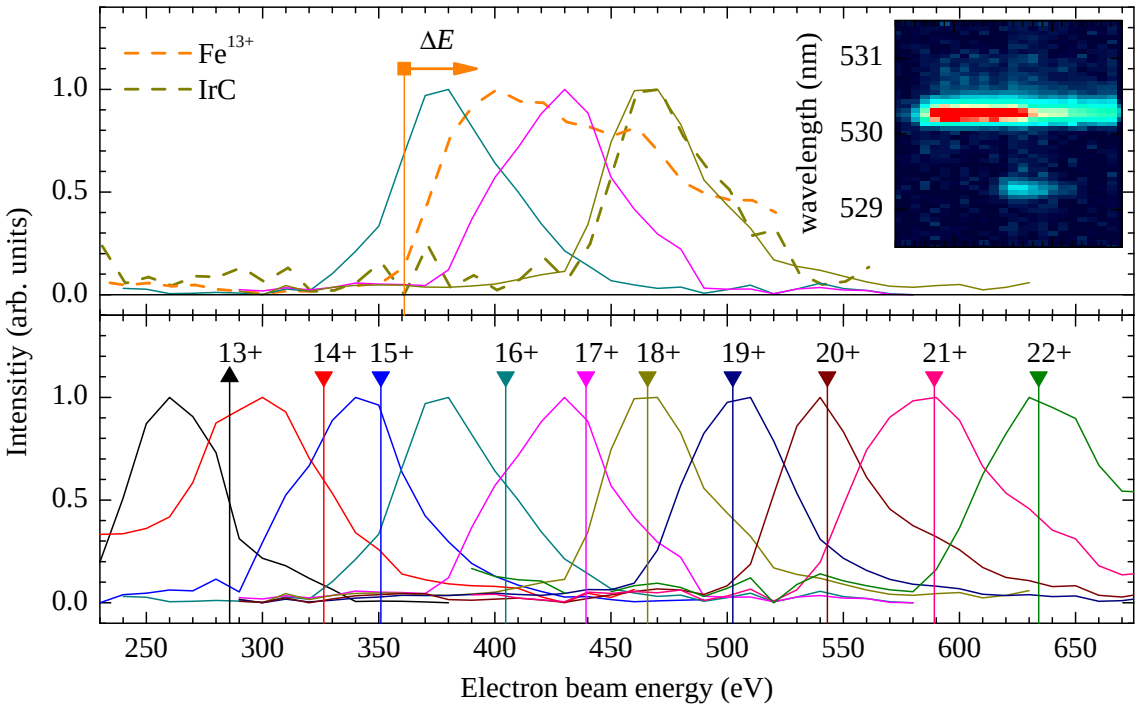

Figure 5.8: Charge state determination with electron beam energy dependent intensity curves. Top: Intensity curves of simultaneously trapped Ir and Fe ions (dashed lines) from the projected Fe^{13+} transition at 530.3 nm and the IrC transition at 529.3 nm (inlay plot). The predicted Fe^{12+} ionization energy (square) coincides with the beginning of the Fe^{13+} intensity curve meaning that the acceleration potential approximately equals the actual electron beam energy. By offsetting other projections (solid lines) with the calibrated IrC ionization curve depicted in the top graph, their ionization energies can be obtained. Bottom: Comparison between FSCC (downwards triangles) [59], CIDFS [62] (upwards triangles), and the projections extracted from figure 5.7. Note that the calculation values are shifted by $\Delta E = 31$ eV in the bottom panel (see main text for explanation) to coincide with the maxima instead of the beginning of the intensity curves for visibility purposes. The displayed data is listed in table 5.2.

and calculations at the lower energy values. Possible reasons were theoretical uncertainties, which could be especially large around the level crossing at Ir^{17+}, or metastable states, which were likely to exist in near-closed shell systems around Ir^{15+}. The latter are long-lived excited states that can have lower radiative decay rates than the electron collision rate in the EBIT. These metastable states are closer to the ionization threshold than the ground state, and thus, they can be ionized at lower electron beam energies. If a significant population accumulated in such a state, the fluorescence of the next higher charge state appeared earlier and the intensity curve was shifted towards lower energies. In particular, this effect could explain the misplacement of the Ir^{16+} fluorescence maximum with respect to the calculations. However, one would expect this effect to become apparent in the

intensity curves as deviations from their typical shape, but the resolution of 10 eV in the electron beam energy might have been too poor to register them.

These effects diminished the reliability of the comparison at lower energies. On the other hand, there was a good agreement between calculations and data for charge states above IrB. This led to the hypothesis that IrB indeed is the Nd-like charge state Ir^{17+}. With the help of VUV spectra, which were always acquired simultaneously with the optical ones, this charge state could be identified for the other elements as well. The VUV intensity curves coincided with the optical ones. However, in contrast to the optical spectra, the VUV data exhibited smoother characteristic spectral line groups that were shifted along the isoelectronic sequence. These spectra are outside the scope of this work and deal with the identification of VUV transitions in Pm-like ions [98].

In figures 5.9, 5.10, 5.11, and 5.12 the 2D maps analogue to figure 5.7 are depicted. For each element the Nd-like charge state was identified and the wavelengths and amplitudes of spectral lines were extracted (see table 5.3). A total of 84 Nd-like transitions have been found this way. At an electron beam energy optimized for W^{14+}, for instance, the spectrum contains 140 spectral features from different W ions in the investigated range resulting in an average separation of 3.8 nm or 0.02 eV. Considering the theoretical uncertainty on the order of 0.1 eV, it becomes clear that an identification of these spectral lines based on a direct comparison with calculated transition energies is futile. Using the above 2D plots, the complexity of the problem could be brought back to 20 spectral lines that were actually emerging from transitions in W^{14+}. This provided a vital first step towards their identification. For such identification, a general method based on the isoelectronic sequences presented here is introduced and demonstrated in Chapter 6.

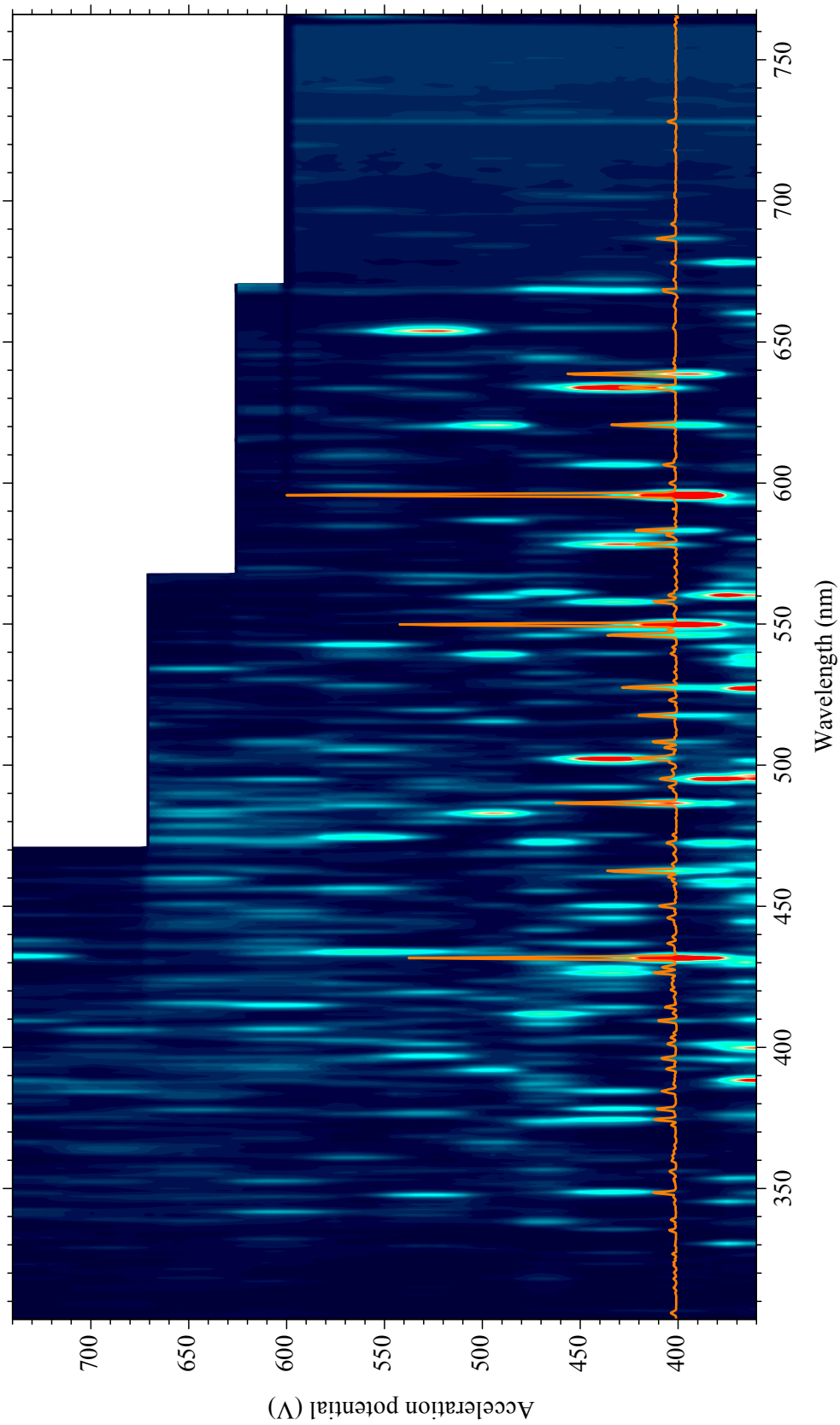

Figure 5.9: 2D map of W charge states and spectral lines composed of energy scans at four grating angles covering the spectral ranges 304-469 nm, 400-566 nm, 503-669 nm, and 601-766 nm. In the overlap regions, the spectra are averaged. The Nd-like W spectrum is overlayed in orange.

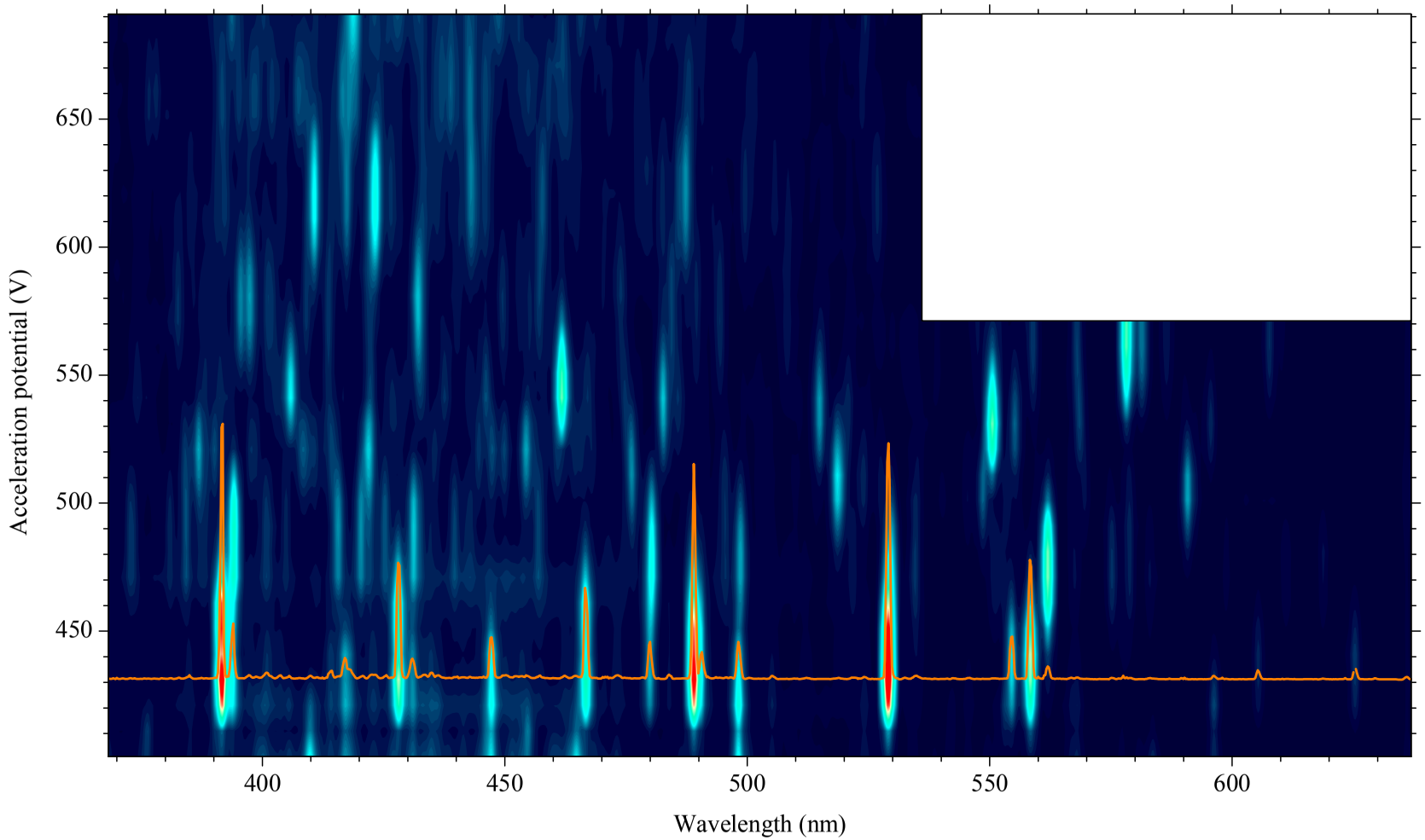

Figure 5.10: 2D map of Re charge states and spectral lines composed of energy scans at two grating angles covering the spectral ranges 368-534 nm and 471-637 nm. In the overlap regions, the spectra are averaged. The Nd-like Re spectrum is overlayed in orange.

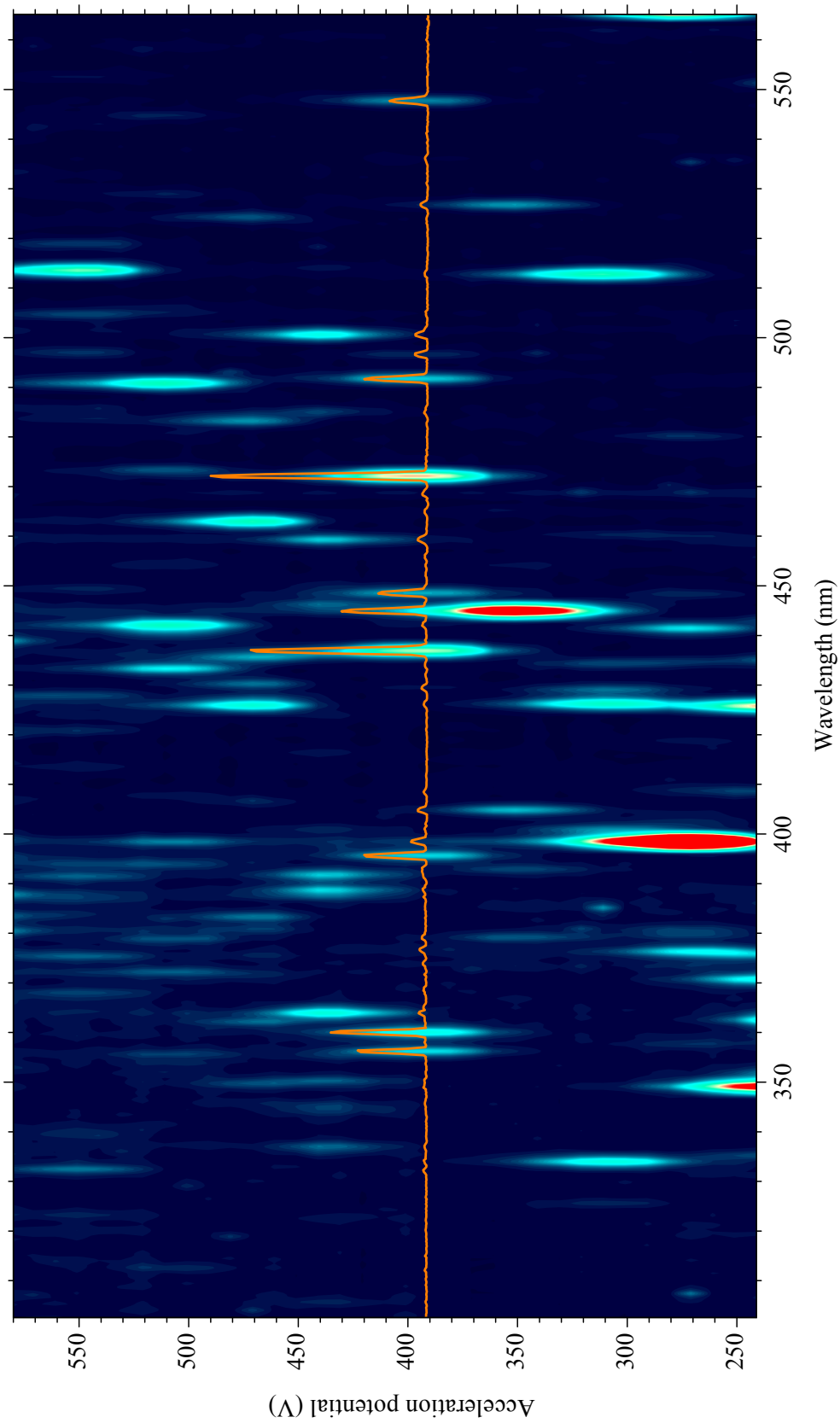

Figure 5.11: 2D map of Os charge states and spectral lines composed of energy scans at two grating angles covering the spectral ranges 303-469 nm and 400-566 nm. In the overlap regions, the spectra are averaged. The Nd-like Os spectrum is overlayed in orange.

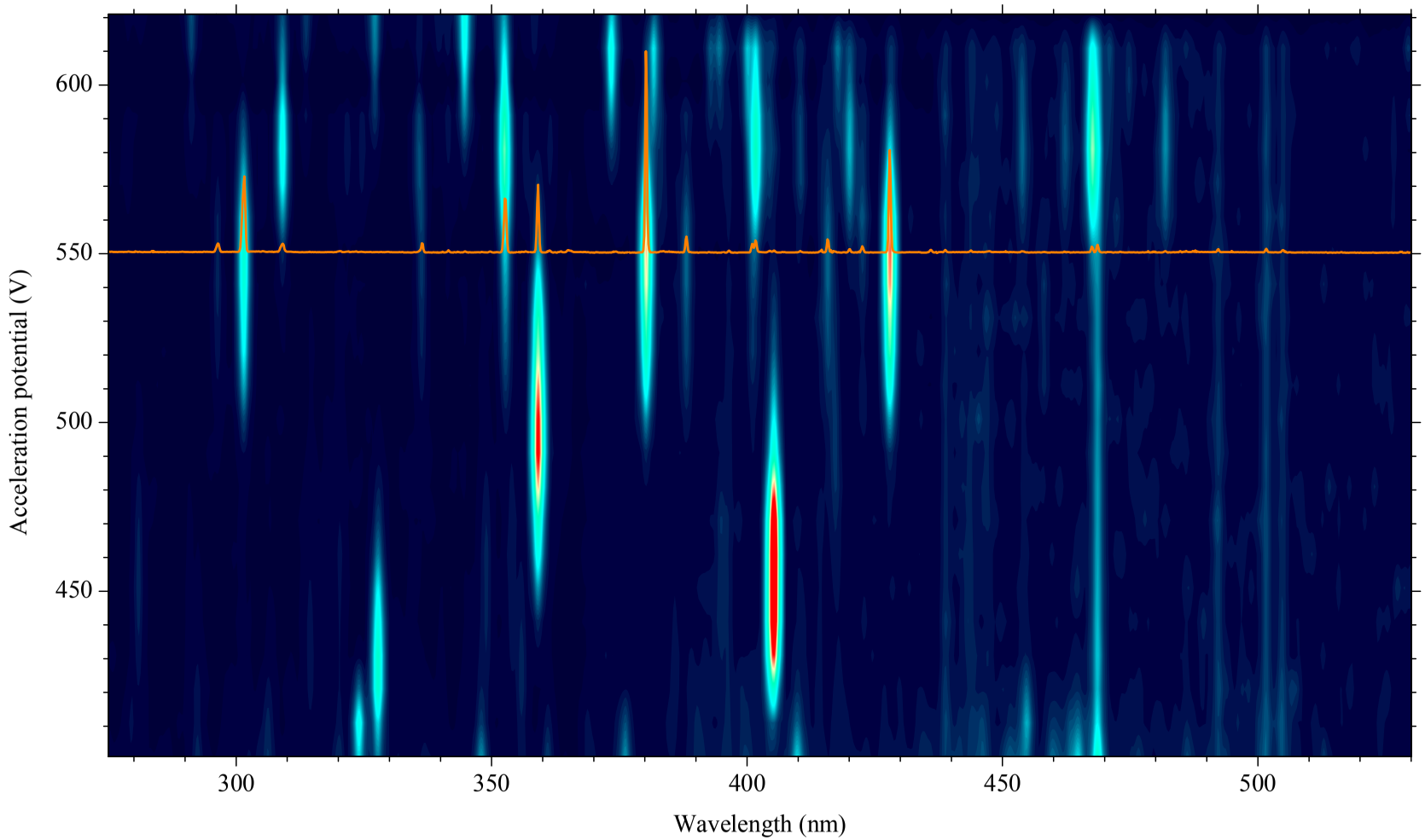

Figure 5.12: 2D map of Pt charge states and spectral lines composed of energy scans at two grating angles covering the spectral ranges 271-437 nm and 368-534 nm. In the overlap regions, the spectra are averaged. The Nd-like Pt spectrum is overlayed in orange.

Table 5.3: Overview of W^{14+}, Re^{15+}, Os^{16+}, Ir^{17+}, and Pt^{18+} spectral lines extracted from 2D spectra. For the W^{14+}, Re^{15+}, Os^{16+}, and Pt^{18+} spectra a 300 lines/mm grating was used covering a range of approximately 160 nm at one angular setting. For Ir^{17+}, a 2400 lines/mm grating was used, before the 300 lines/mm became available, covering a range of 18 nm at each grating angle. The settings were optimized for a fast wavelength scan. The uncertainty is 0.02 nm, resulting from a large slit width of 200 µm. The most intense Ir^{17+} transitions were additionally acquired with high resolution and accuracy as listed in table 5.4.

W^{14+} (nm)	Amp. (norm.)	Re^{15+} (nm)	Amp. (norm.)	Os^{16+} (nm)	Amp. (norm.)	Ir^{17+} (nm)	Amp. (norm.)	Pt^{18+} (nm)	Amp. (norm.)
392.36	0.023	391.66	1.000	356.22	0.326	226.63	0.003	296.41	0.042
396.12	0.036	393.89	0.188	360.05	0.442	238.54	0.003	301.50	0.355
409.43	0.047	414.10	0.027	395.63	0.290	240.10	0.003	336.40	0.045
431.68	0.659	417.20	0.058	436.92	0.807	248.19	0.002	352.66	0.269
462.52	0.178	428.10	0.440	448.55	0.221	255.87	0.003	380.23	1.000
486.55	0.312	430.94	0.070	472.11	1.000	271.70	0.005	388.12	0.077
506.27	0.029	447.24	0.154	491.72	0.279	280.87	0.003	401.06	0.042
508.27	0.061	466.70	0.325	496.63	0.055	289.51	0.005	415.81	0.064
517.64	0.100	479.91	0.130	547.73	0.166	292.65	0.014	427.95	0.489
527.59	0.136	489.01	0.751			298.16	0.007		
546.12	0.178	490.59	0.086			301.07	0.002		
549.86	0.710	505.21	0.011			304.24	0.008		
583.22	0.107	529.09	0.874			314.95	0.006		
595.71	1.000	554.54	0.158			321.91	0.008		
620.61	0.164	558.39	0.439			323.04	0.006		
638.63	0.283	605.35	0.029			324.60	0.126		
686.64	0.047	625.36	0.037			329.29	0.299		
691.76	0.011					365.03	0.053		
717.97	0.004					388.83	0.018		
735.96	0.004					391.83	0.381		
						399.35	0.065		
						401.69	0.013		
						422.89	1.000		
						431.60	0.101		
						435.63	0.191		
						445.69	0.052		
						482.69	0.222		
						545.83	0.006		
						577.57	0.006		
						597.65	0.010		

5.4 High-resolution spectra of Ir^{17+} transitions

The $4f$-$5s$ level crossing is expected to occur in Ir^{17+}. This is why the most interesting of the mapped ion spectra is Ir^{17+}, as it offers narrow optical E1 transitions with an extremely high sensitivity to a possible α variation (see Chapter 2). Therefore, the brightest lines assigned to this ion were remeasured at high accuracy and high resolution using the scheme demonstrated in section 5.1. The obtained spectra presented in figure 5.13 were typically averaged over 30 calibration-acquisition-calibration cycles, similar to those presented in figure 5.3. The EBIT was operated with an electron beam current of 40 mA and an acceleration potential of 590 V. These settings were chosen before the charge state identification was certain, and unfortunately the acceleration potential was 40 V too high for this electron beam current to obtain an optimal intensity for Ir^{17+} transitions. Fortunately, the brightest Ir^{17+} transitions could still be obtained with sufficient intensity for the following analysis.

The wavelengths have been provided by the weighted mean of the fitted line centroids of all individually calibrated acquisitions. The results for the Ir^{17+} transitions can be found in figure 5.14. The brightest lines showed the lowest statistical scatter, such as the transition at 422.9 nm. For these lines, a so far unobserved systematic effect became evident: During these measurements, the grating angle is fixed for five acquisitions and then rotated to shift the spectral range by 0.1 nm, five times more as in section 5.1. The data points taken immediately after a rotation are systematically shifted to higher wavelengths by approximately 0.003-0.004 nm. This can be explained through a mechanical instability of the grating which drifts after setting a new rotation angle. The effect could be prevented by rotating the grating by smaller amounts or waiting 5-10 min before starting the first calibration acquisition. For the second acquisition within a set the grating has already come to rest. After eliminating the flawed first data point, the statistical scatter was again represented well by the fit uncertainties of the individual centroids, as it was verified by the reduced χ^2-values of the mean.

The results for the wavelengths and their uncertainty budgets are given in table 5.4. In most cases, the accuracy was limited by the statistical uncertainty. A total uncertainty in the sub-ppm region is frequently achieved and could be as low as 0.2 ppm. An accurate knowledge of wavelengths is an important prerequisite for follow-up laser spectroscopy in a Paul trap, and was also needed to infer unobserved or unidentified transitions from Rydberg-Ritz combinations, as explained in Chapter 6. Moreover, the high resolution spectroscopic data could be used to identify transitions by their Zeeman splitting of which a detailed analysis can be found in section 6.2.

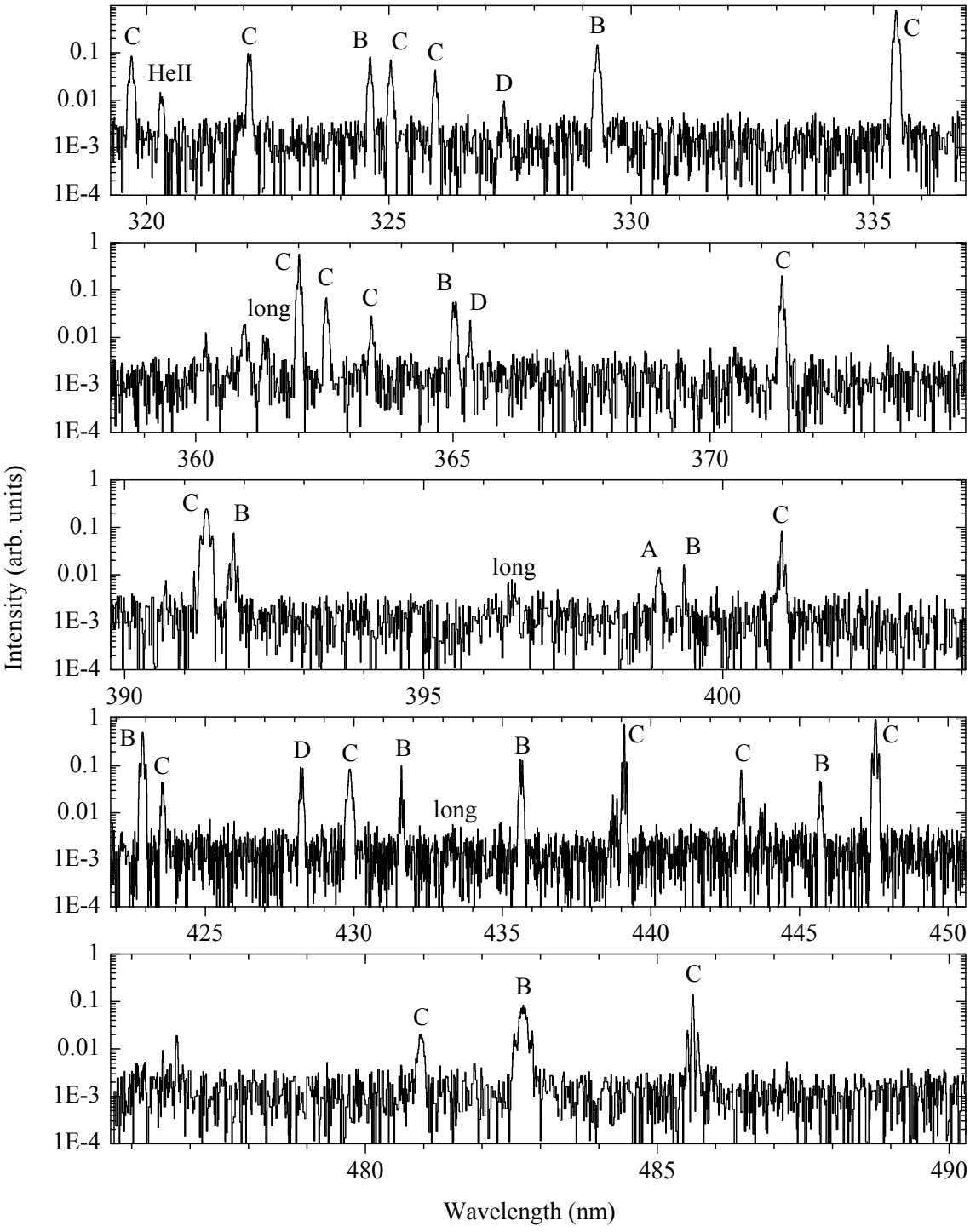

Figure 5.13: High resolution and accuracy spectra of Ir ions. Spectral lines that could be identified are labeled with A for Ir^{16+}, B for Ir^{17+}, C for Ir^{18+}, and D for Ir^{19+}. Energy independent features are labeled as "long". One of these could be identified as HeII transition. The others could belong to residuals of highly ionized carbon or oxygen injected as part of the organo-metals together with Ir. A detailed analysis of the spectral line shapes is given in section 6.2.

Table 5.4: Table of measured wavelengths in Ir^{16+}, Ir^{17+}, Ir^{18+}, and Ir^{19+} with amplitudes. The total uncertainty is the squared sum of the statistical uncertainty, represented by the scatter of single-acquisition wavelengths, and the systematic uncertainty, given by the 1σ width of the confidence band of the calibration function.

Charge state	Wavelength (nm)	Scatter (10^{-4} nm)	Calibration (10^{-4} nm)	Amplitude (arb. units)
18+	319.6844(6)	4.8	2.8	11.5(2)
18+	322.1156(5)	5.1	1.7	13.8(2)
17+	324.6113(4)	3.7	2.0	11.3(2)
18+	325.0363(6)	5.6	2.0	9.2(2)
18+	325.9571(6)	6.0	2.2	5.5(2)
17+	329.3025(4)	3.7	2.4	20.0(3)
18+	335.4725(4)	1.6	4.0	110.4(7)
18+	362.0098(2)	1.0	1.3	88.0(6)
18+	362.5368(7)	6.4	1.2	9.5(2)
18+	363.4171(10)	9.7	1.3	3.8(2)
17+	365.0318(10)	10	1.4	7.5(1)
19+	365.3359(12)	12	1.5	3.5(2)
18+	371.3990(2)	1.6	1.2	31.4(4)
18+	391.3694(3)	2.7	1.1	36.7(3)
17+	391.8220(3)	2.7	1.0	11.9(3)
17+	399.3556(10)	10	1.8	2.5(3)
16+	398.9306(21)	21	1.8	1.9(1)
18+	400.9860(3)	2.6	1.7	12.9(3)
17+	422.8950(3)	1.9	1.9	80(1)
18+	423.5667(15)	15	1.7	5.8(2)
19+	428.2449(8)	8.2	0.9	9.3(3)
18+	429.8646(8)	8.5	0.9	12.4(2)
17+	431.6044(3)	2.8	0.8	16.1(4)
17+	435.6348(5)	4.7	1.1	13.6(2)
18+	439.1032(1)	0.6	0.7	128.5(8)
18+	443.0385(4)	4.1	0.7	13.3(2)
17+	445.7057(9)	9.0	1.2	6.4(2)
18+	447.5607(2)	0.9	2.1	159.2(6)
18+	480.9537(16)	16	0.7	3.0(1)
17+	482.7039(7)	7.3	0.8	11.0(1)
18+	485.6083(2)	1.7	0.7	22.4(4)

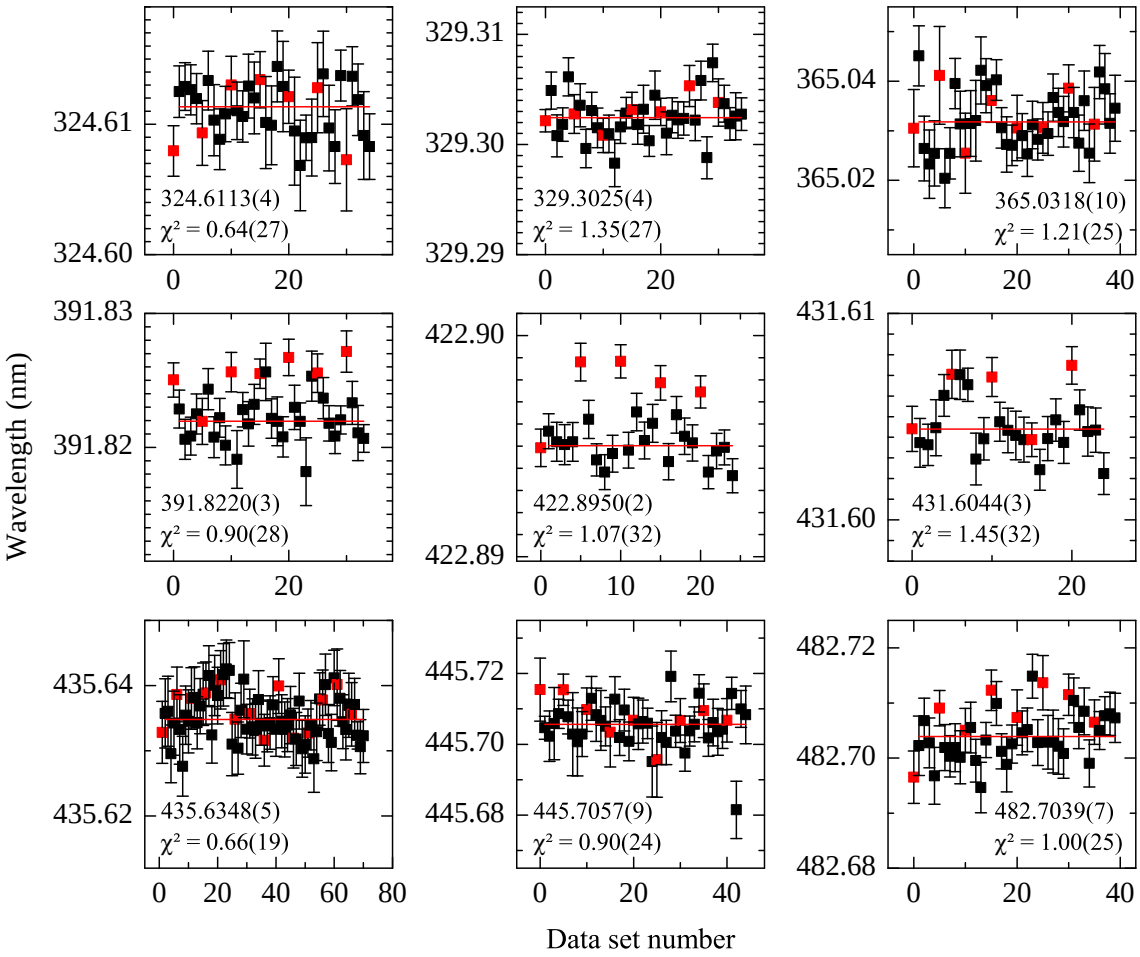

Figure 5.14: Averaging of single-acquisition spectral line centroids. The first data point (red squares) in every set of five acquisitions is discarded because of a drift of the grating immediately after rotating to a new angle. The other data points (black squares) are randomly distributed around the mean (red line) with a standard deviation characterized by the single-acquisition fit uncertainties (error bars).

Chapter 6

Analysis and discussion

With the estimated uncertainty of atomic structure codes being at least of the same order as the average separation between spectral lines measured, alternative methods had to be found in order to identify transitions in the obtained spectra. Three distinct methods were applied, leading to the identification of 47 lines in the Nd-like spectra. First, a novel technique is introduced, which exploits the characteristic scaling of fine structure transitions along an isoelectronic sequence. By these means, isoelectronic transitions could be identified even in the low-resolution spectra, which proved this scheme efficient and generally applicable. For W^{14+}, all level energies of the ground state configuration could be fully determined and the energy of the forbidden $4f^{12}5s^2\,{}^3F_4$-$4f^{12}5s^2\,{}^3H_6$ transition (see section 2.3.2) energy inferred. By following the obtained scaling laws, this transition energy could be interpolated to Hf^{12+}. Furthermore, the high-resolution spectra were analyzed using the g-factor model for Zeeman-split spectral lines. By inserting calculated g-factors into the model, the spectral lines could be identified based on their profiles. Thereby, the M1 scaling identification was independently confirmed. For the identification of E1 transitions in Ir^{17+}, the measured transition energies were searched for Rydberg-Ritz combinations, supported by the many spectral lines that had been identified before. Two more M1 transitions could be identified and three possible candidates for E1 transitions were found. With the identified transitions, theory could be tested experimentally for the first time in these atomic systems, which provides an important benchmark needed to improve calculations for further studies of optical transitions in complex HCI.

6.1 Identification of M1 transitions in isoelectronic sequences

From the simplified considerations for H-like ions in section 2.1.1, a smooth scaling of the energy splitting in the fine structure $E_{\mathrm{FS}} \propto (Z \cdot Z_{\mathrm{eff}})^2$ could be expected. When applied to the Nd-like ions, this scaling would affect M1 transitions within the configurations

$4f^{12}5s^2$ and $4f^{13}5s^1$. The Grotrian diagram of the atomic structure illustrates this: For M1 transitions within these configurations, many optical transitions are possible along the whole measured isoelectronic sequence. In contrast to this, E1 transitions in the optical range only occur for Ir^{17+}. For a realistic model of the M1 energy-scaling, the exact electron screening of the nuclear potential, angular momentum couplings, and other effects of electron correlations had to be included, and a simple analytical expression did not hold. Transition energies that were extracted from FSCC and FAC atomic structure calculations (see table 2.1 and 2.2) nevertheless exhibited the anticipated scaling with Z.

For the small range of $74 \leq Z \leq 78$, a quadratic Taylor expansion around $Z_{\mathrm{mean}} = 76$ described this behavior sufficiently well. The energy E_{i} was fitted for 13 observable isoelectronic transitions as a quadratic function of Z

$$E_{\mathrm{i}}(Z) = A_{\mathrm{i}} + B_{\mathrm{i}}(Z - Z_{\mathrm{mean}}) + C_{\mathrm{i}}(Z - Z_{\mathrm{mean}})^2, \tag{6.1}$$

where A_{i}, B_{i}, and C_{i} are fit parameters. Since no error estimate for the theoretical values was made, the fit quality was characterized by standard deviation σ or the variance σ^2 of the transition energies with respect to the fit. Values of the order of $\sigma^2 \approx 10^{-8}$-$10^{-7}\,\mathrm{eV}^2$ or $\sigma \approx 10^{-4}\,\mathrm{eV}$ were reached, and the fit parameters showed values in the ranges:

$$2.2388(1)\,\mathrm{eV} \leq A_{\mathrm{i}} \leq 3.4897(2)\,\mathrm{eV}, \tag{6.2}$$

$$0.1083(1)\,\mathrm{eV} \leq B_{\mathrm{i}} \leq 0.3275(2)\,\mathrm{eV}, \tag{6.3}$$

$$0.00032(8)\,\mathrm{eV} \leq C_{\mathrm{i}} \leq 0.01231(6)\,\mathrm{eV}. \tag{6.4}$$

The numbers in brackets indicate the standard fit uncertainty for the parameters.

To verify if the theoretically expected scalings could be found in the data acquired using the 300 lines/mm grating, a search algorithm was developed. First, all possible combinations of transition energies in three of the Nd-like ions were fitted by a function (6.1). Subsequently, all combinations of transition energies in the remaining two spectra were added to the fit, and its quality was determined by the value of the variance σ^2. When a quintuple of transition energies within sufficient agreement with the model was found, it was checked positive and the corresponding $(A_{\mathrm{i}}, B_{\mathrm{i}}, C_{\mathrm{i}})$-parameters were recorded. For such a large number of transitions, the figure of merit for the fit σ^2 had to be chosen as low as possible in order to discriminate spectral lines randomly agreeing with the fit. On the other side, no real scaling in the data should be missed out due to too strict discrimination criteria. In figure 6.1, experimental $(A_{\mathrm{i}}, B_{\mathrm{i}})$-pairs are shown for different σ^2-criteria. For $\sigma^2 \leq 10^{-1}\,\mathrm{eV}^2$, several 10 000 curves were found, but almost all of them were random false positives.

To estimate the number of expected false positives, the search algorithm was applied 100 times with the same filter settings to sets of randomly generated spectra, and a histogram of false positive results was recorded. The results are shown in figure 6.2. The number of real scalings found in the spectra started to exceed the anticipated number of false positives significantly at $\sigma^2 \leq 5 \times 10^{-6}\,\mathrm{eV}^2$. At $\sigma^2 \leq 1 \times 10^{-6}\,\mathrm{eV}^2$, the probability of finding no false positive scaling was at 0.2. This corresponded to a deviation of the fitted curve from the actual wavelength of typically 0.1 nm, much higher than the experimental uncertainty of approximately 0.02 nm. A final filtering step was applied to raise this probability to above 0.95. According to the scalings expected from the calculations, the $(B_\mathrm{i}, C_\mathrm{i})$-parameters were loosely restrained to values of B_i and C_i in the intervals (compare to equations (6.3),(6.4))

$$0.05\,\mathrm{eV} \leq B_\mathrm{i} \leq 0.35\,\mathrm{eV}, \tag{6.5}$$

$$0.0001\,\mathrm{eV} \leq C_\mathrm{i} \leq 0.02\,\mathrm{eV}. \tag{6.6}$$

This step means that transition energies always grow with Z, and that an excessive curvature can be excluded due to theoretical arguments. The spectral lines involved in the remaining eight scalings could all be assigned with 0.95 certainty to M1 transitions. As can be seen in figure 6.3, these are the most intense lines in each spectrum, particularly in the Ir^{17+} spectrum in which E1 transitions are expected as well. While in general, M1 transitions are suppressed by a factor of α^2 (see section 2.1.2) with respect to E1 transitions due to selection rules, we found here nonetheless M1 lines as the strongest ones. This counter-intuitive behavior can be explained by the poor overlap of the wavefunctions, as a $4f$ electron has to be promoted to a $5s$ orbital. The very small E1 matrix elements are solely due to the configuration interaction mixing of the states $4f$ and $5s$, which in the absence of the interaction would be perfectly orthogonal and thus equal to zero. Indeed, FAC calculations yielded Einstein A-coefficients on the order of 1 Hz for the E1 transitions, which is a factor of 100 weaker than for the M1 transitions.

By analyzing the spectra in figure 6.3, a ninth scaling could be discovered that was not found by the search algorithm due to a blend in the spectral line at 2.8714(1) eV in the W^{14+} spectrum. Hence, the W^{14+} spectrum had been excluded. After taking it into consideration, all spectral lines in the Nd-like Os and Pt spectra could be assigned to scalings and therefore identified as M1 transitions.

The final set of 9 experimental scaling functions was compared to the 11 theoretically expected ones in order to obtain definite assignments depicted in figures 6.3 and 6.4, and

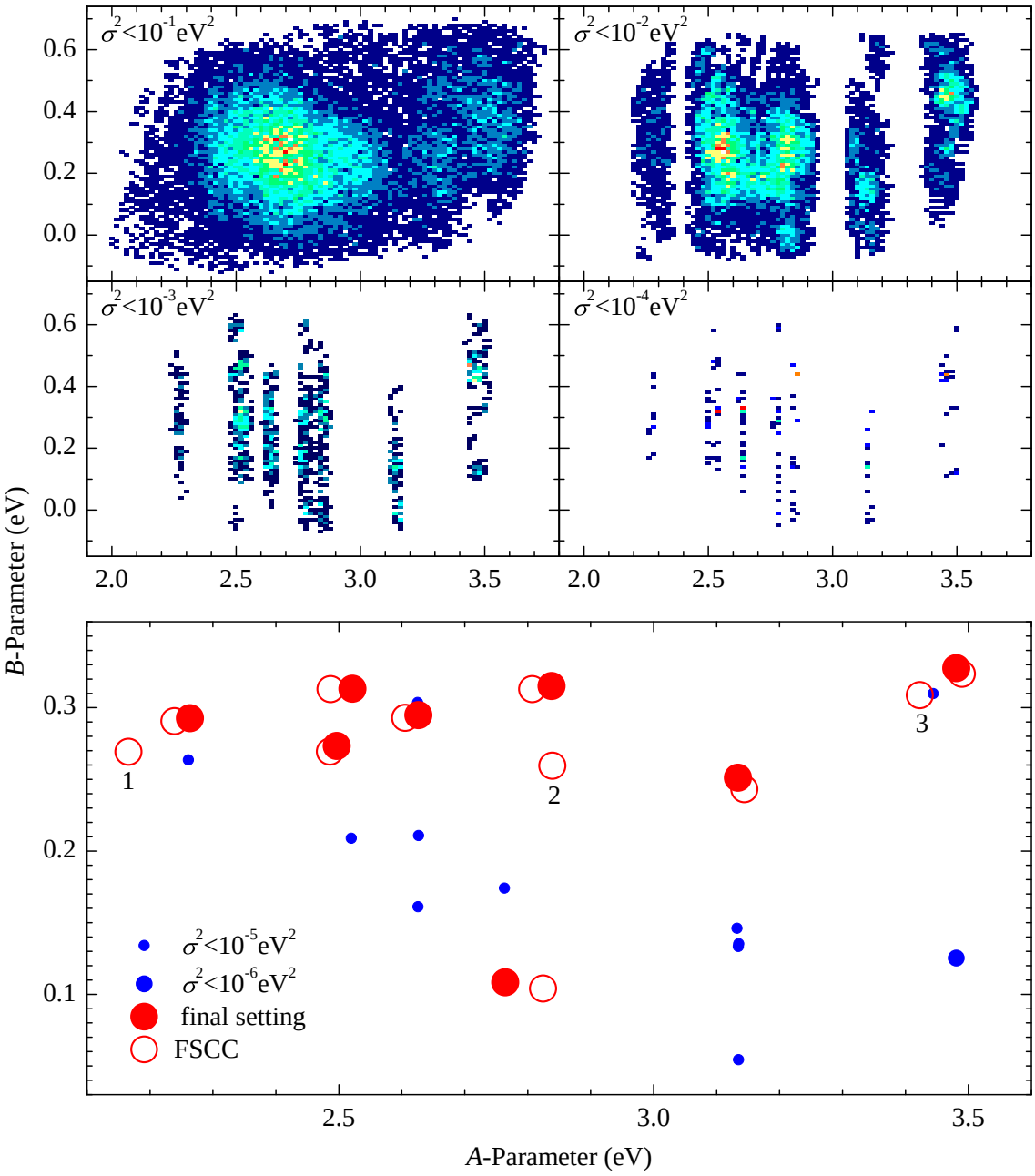

Figure 6.1: Top: Scaling functions found in the acquired spectra by a search algorithm. The density of $(A_\mathrm{i}, B_\mathrm{i})$-parameters is represented by the color scale. The large number of random scalings is reduced by limiting the allowed fit variance σ^2. Bottom: By applying the final setting (see figure 6.2), no false positive scaling is found with a probability of 0.95. FSCC calculations predict scalings with similar $(A_\mathrm{i}, B_\mathrm{i})$-parameters close to every experimental one. The open red circles marked by the numbers 1 and 2 are predicted scalings which could not be observed in the spectrum. Number 3 could be identified by a closer analysis of the measured spectra (see main text). The actual functions as well as an assignment of scaling parameters can be found in figures 6.3 and 6.4.

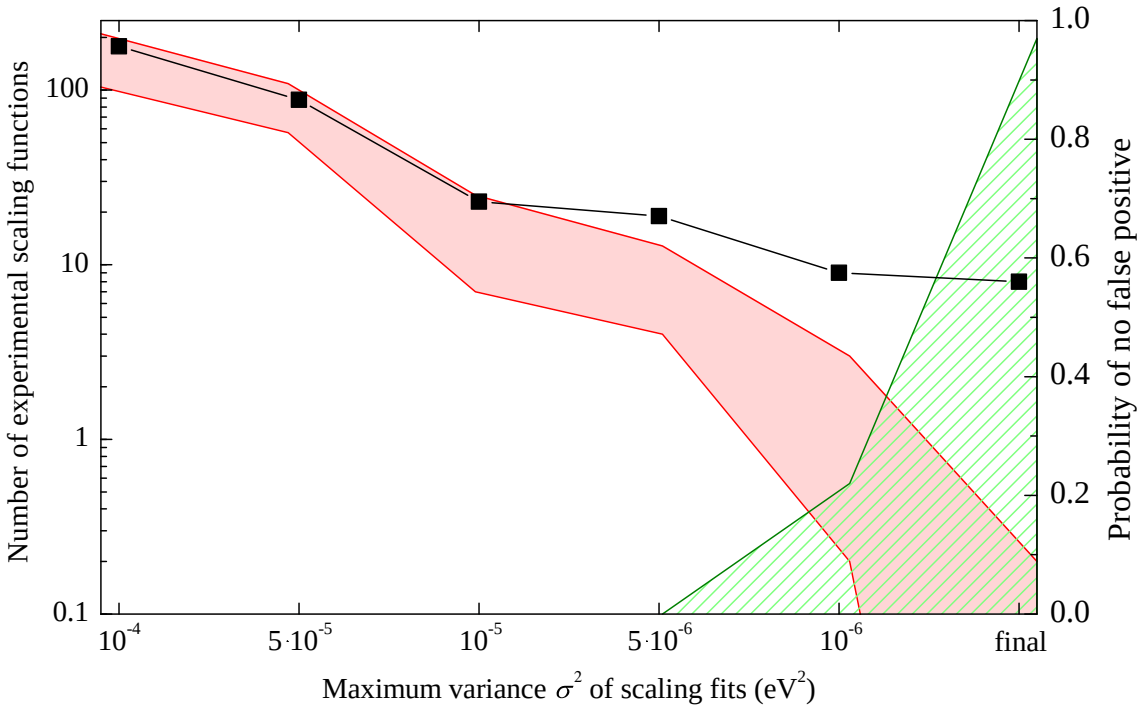

Figure 6.2: Significance test of found scaling functions. For each σ^2-limit, the number of scaling functions found in the data (black squares) is compared to the 1σ-band (red) of expected scalings in randomly generated spectra (left axis). For the final filtering settings, the probability of finding not a single false positive (green) is at a 0.95 level (right axis).

listed in table 6.1. This was achieved through minimizing the χ^2 value

$$\chi^2 = \sum_i \sqrt{\frac{(A_{\mathrm{exp,i}} - A_{\mathrm{theo,i}})^2}{\sigma^2_{\mathrm{A_{exp},i}} + \sigma^2_{\mathrm{A_{theo},i}}} + \frac{(B_{\mathrm{exp,i}} - B_{\mathrm{theo,i}})^2}{\sigma^2_{\mathrm{B_{exp},i}} + \sigma^2_{\mathrm{B_{theo},i}}} + \frac{(C_{\mathrm{exp,i}} - C_{\mathrm{theo,i}})^2}{\sigma^2_{\mathrm{C_{exp},i}} + \sigma^2_{\mathrm{C_{theo},i}}}} \tag{6.7}$$

for all possible $(A_\mathrm{i}, B_\mathrm{i}, C_\mathrm{i})$-parameter assignments. The theoretical and experimental fit uncertainties σ_i of the corresponding parameters were used for the weights. Due to the enormous number of possible combinations, experimental $(A_\mathrm{i}, B_\mathrm{i}, C_\mathrm{i})$-parameters had to be compared to theory in sets of four, but all sets gave the consistent identifications shown in table 6.2.

For every assigned scaling curve, five isoelectronic transitions were identified corresponding to the number of ion species under investigation. Moreover, transition energies can be predicted for the neighboring Nd-like ions, Ta^{11+} and Au^{19+} by following the scaling functions. The 1σ-confidence band of the functions yields a good estimate for the uncertainty of these predictions and amounts to few meV, which is orders of magnitude more accurate than *ab initio* calculations. This outcome, combined with the relatively low required experimental accuracy, makes this method very efficient. With some experience, the full optical spectral range for one ion could be covered in a week.

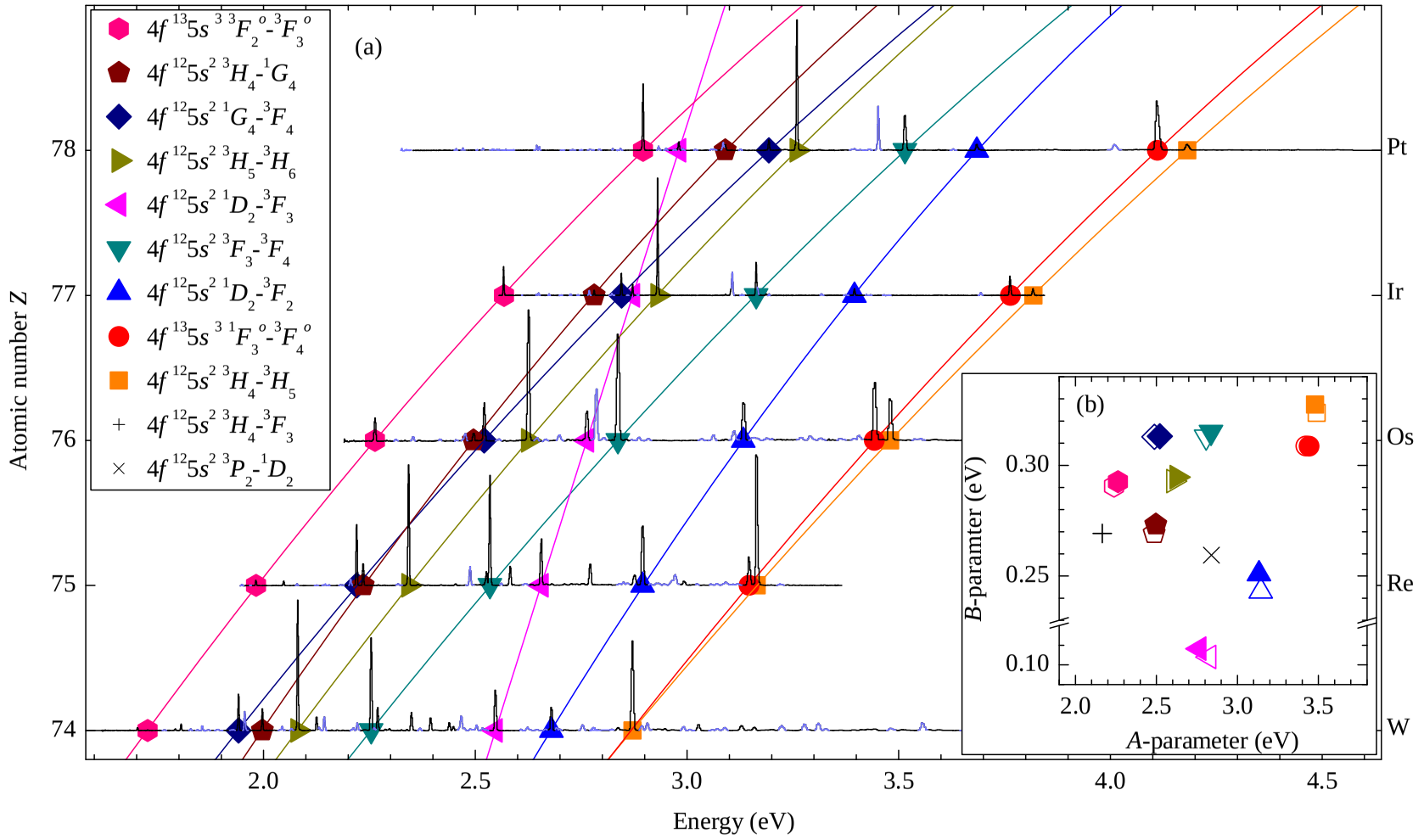

Figure 6.3: (a) Filtered scaling functions (colored lines) on top of the measured spectra (black lines). Transitions belonging to other charge states are grayed out. (b) Nine of the experimental scaling functions (full symbols) could be assigned to the calculated ones (open symbols) by minimizing the χ^2-value between their $(A_\mathrm{i}, B_\mathrm{i}, C_\mathrm{i})$-parameters. Two scalings could not be observed (crosses). The unit conversion from nm to eV was performed according to the description in section 4.6.

Table 6.1: Fit parameters of the experimental and theoretical scaling functions shown in figure 6.3. The parameters A_i, B_i, and C_i are the constant offset, the linear coefficient, and the quadratic coefficient from the fit function equation (6.1). Error bars are derived from the fit. They do not include the much larger uncertainty inherent to the *ab initio* calculations for such highly-correlated electron systems.

Tran-	A_i (eV)		B_i (eV)		C_i (eV)	
sition	Exp.	Theory	Exp.	Theory	Exp.	Theory
$^3F_2^o$-$^3F_3^o$	2.2629(2)	2.2388(1)	0.2926(1)	0.29058(5)	0.01213(9)	0.01193(4)
$^3H_4$-$^1G_4$	2.4960(3)	2.4859(2)	0.2732(1)	0.26929(9)	0.0120(1)	0.01219(7)
$^1G_4$-$^3F_4$	2.5209(3)	2.4870(2)	0.3131(1)	0.31289(7)	0.0116(1)	0.01153(6)
$^1D_2$-$^3F_3$	2.7635(3)	2.8245(2)	0.1083(1)	0.1041(1)	0.0002(1)	0.00032(8)
$^3H_5$-$^3H_6$	2.6256(4)	2.6054(3)	0.2947(2)	0.2929(1)	0.0112(2)	0.0112(1)
$^3F_3$-$^3F_4$	2.8371(5)	2.8071(2)	0.3150(2)	0.31291(8)	0.0119(2)	0.01171(7)
$^1D_2$-$^3F_2$	3.1331(7)	3.1442(6)	0.2510(3)	0.2431(2)	0.0123(3)	0.0127(2)
$^1F_3^o$-$^3F_4^o$	3.44256(3)	3.4229(2)	0.30861(2)	0.30867(7)	0.01282(2)	0.01231(6)
$^3H_4$-$^3H_5$	3.4798(4)	3.4897(2)	0.3274(2)	0.32366(9)	0.0117(2)	0.01181(7)
$^3H_4$-$^3F_3$	–	2.1658(2)	–	0.26927(8)	–	0.01201(7)
$^3P_2$-$^1D_2$	–	2.8394(4)	–	0.2595(2)	–	0.0092(2)

Table 6.2: Identified M1 transitions in W^{14+}, Re^{15+}, Os^{16+}, Ir^{17+}, and Pt^{18+} belonging to the scalings assigned in table 6.1. For W^{14+}, Re^{15+}, Os^{16+}, and Pt^{18+}, the data presented in table 5.3, and for Ir^{17+}, the high-resolution data from table 5.4 is used. The transitions marked with * are assigned to blended spectral lines. The unit conversion from nm to eV was performed using the CODATA recommended value for hc [4].

Transition	W^{14+}	Re^{15+}	Os^{16+}	Ir^{17+}	Pt^{18+}
$^3F_2^o$-$^3F_3^o$	1.72640(5)	1.98206(6)	2.26296(8)	2.567818(4)	2.8964(1)
$^3H_4$-$^1G_4$	1.99722(6)	2.23520(8)	2.4958(1)	2.780970(6)	3.0905(2)
$^1G_4$-$^3F_4$	1.94086(6)	2.21979(8)	2.5207(1)	2.845258(3)	3.1935(2)
$^1D_2$-$^3F_3$	2.5475(1)	2.6559(1)	2.7634(1)	2.871827(2)	2.9809(1)
$^3H_5$-$^3H_6$	2.08070(7)	2.34272(9)	2.6254(1)	2.930971(2)	3.2598(2)
$^3F_3$-$^3F_4$	2.25422(8)	2.5347(1)	2.8369(1)	3.163403(2)	3.5147(2)
$^1D_2$-$^3F_2$	2.6799(1)	2.8954(1)	3.1329(2)	3.395564(9)	3.6845(2)
$^1F_3^o$-$^3F_4^o$	2.8714(1)*	3.1468(2)	3.4426(2)	3.763971(5)	4.1111(3)
$^3H_4$-$^3H_5$	2.8714(1)*	3.1647(2)	3.4796(2)	3.818365(5)	4.1816(3)

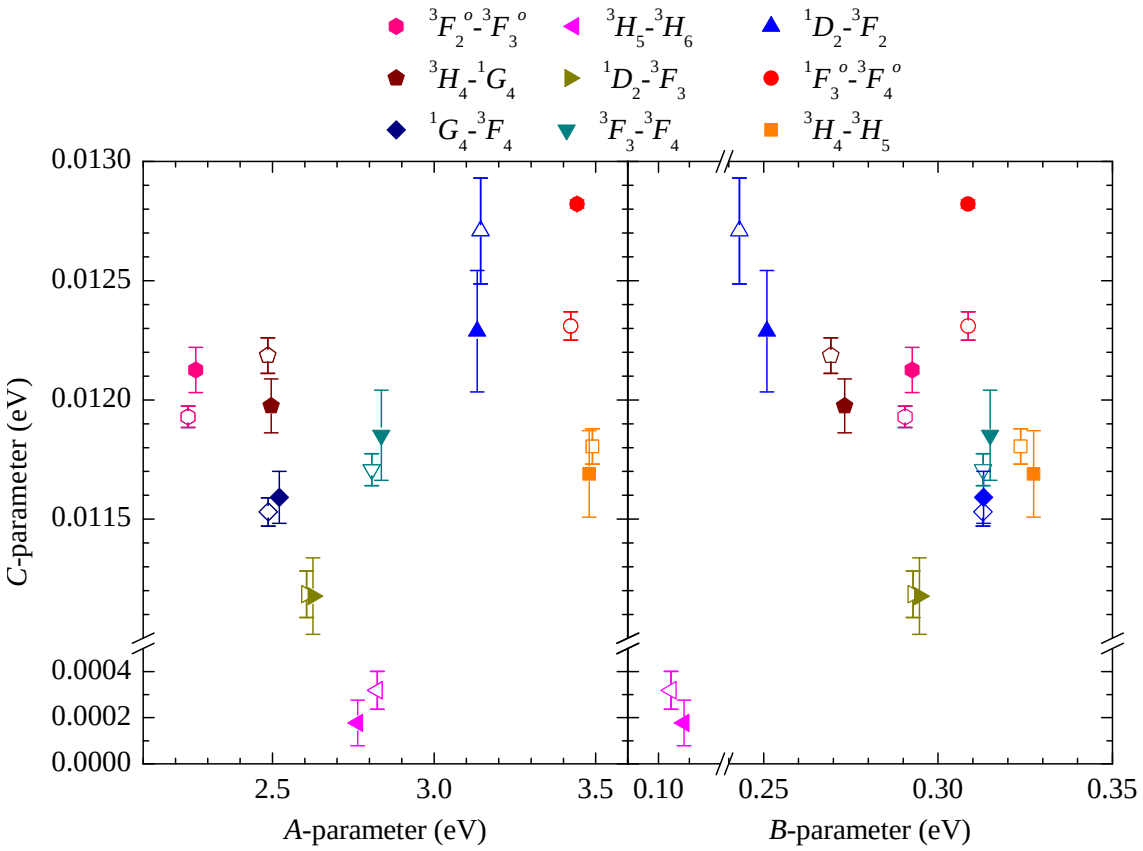

Figure 6.4: Comparison of (A,C) and (B,C)-parameters between experiment (full symbols) and FSCC calculations (open symbols), similar to figure 6.3. The values of the points can be found in table 6.1. Transition $^1F_3^o$-$^3F_4^o$ is blended with transition $^3H_4$-$^3H_5$ in the W^{14+} spectrum, which is why the data point $^1F_3^o$-$^3F_4^o$ shows a stronger deviation between experiment and theory than the others.

Another immediate result of these identifications, and a good example of the advantages of the method, is the identification of the $4f^{12}5s^2\,{}^3F_4$-$4f^{12}5s^2\,{}^3H_6$ transition in W^{14+} and Hf^{12+}. Since the surrounding M1 transition energies had been obtained, the transition energy of $4f^{12}5s^2\,{}^3F_4$-$^3H_6$ in W^{14+} could be inferred by

$$E(4f^{12}5s^2\,{}^3F_4 - {}^3H_6) = -\left(E({}^3F_4 - {}^1G_4) + E({}^1G_4 - {}^3H_4)\right) + E({}^3H_4 - {}^3H_5) + E({}^3H_5 - {}^3H_6) \tag{6.8}$$

Moreover, the same transition energy could be predicted for Hf^{12+} by extrapolating the energies in equation (6.8) with the scaling functions for $Z = 72$. For an uncertainty estimate, the extrapolated 1σ-confidence bands of all transition energies were added quadratically. The results are presented and compared to the theoretical predictions in table 6.3. The

Table 6.3: $4f^{12}5s^2\,{}^3F_4$-$^3H_6$ transition energy, determined by using the identified transitions from table 6.2 and the scaling functions from 6.1. Calculated values deviate by approximately 10%, a value which is typical for the theoretical uncertainties of the experimentally found transitions.

Ion	Experiment (eV)	Theory [30] (eV)	Wavelength (nm) Vacuum	Air
Hf^{12+}	0.934(6)	1.062	1327(9)	1327(9)
W^{14+}	1.0140(2)	1.141	1222.7(2)	1222.4(2)

uncertainty on the calculated value, presented in [30] could be reduced from more than 10% down to few parts-per-thousand.

6.2 Line identification by analysis of the resolved Zeeman splitting

The spectral line identification by the energy scaling of M1 transitions could be verified by independently comparing the line shapes in highly-resolved Ir^{17+} spectra (see section 5.4) to the g-factor model presented in section 2.4.4. All Ir^{17+} transitions identified in table 6.2 were studied at high resolution. Equation (2.52) was used to fit the identified transitions similar to the demonstration with the $2p\,{}^2P_{1/2}$ - $^2P_{3/2}$ transition in the B-like Ar in section 5.1. For the fits, the magnetic field strength of 8 T and the centroid energies inferred from the accurate measurements presented in section 5.4 were used. The g,g'-factors for all states were calculated using the CI-type AMBiT code [99], leaving only three independent free parameters for the fit: the amplitudes $a_{\Delta m=0}$ and $a_{-1} = a_{+1}$ accounting for the different detection efficiencies for the three polarizations and the common width of the Gaussian components w.

The fit results are shown in figure 6.5 and the parameters are given in table 6.4. The best agreement between model and data was achieved for the identifications obtained by the M1 scaling method, which thus confirmed it. For comparison, a second set of fits was performed, setting the g,g'-factors as free parameters. The fit residuals are plotted in figure 6.6. In most cases, the g,g'-factors had too large uncertainties in the fit due to the crossed terms of the covariance matrix to allow for a quantitative analysis. However, it appears they were generally underestimated similar to ones determined from the $2p\,{}^2P_{1/2}$ - $^2P_{3/2}$ transition in the B-like Ar. This effect could be due to a small decrease of the magnetic field strength over time, as mentioned in section 5.1, or due to calculation uncertainties of the g,g'-factors on the order of 10%. Nevertheless, the two different sets of fits agreed well with each other. The $^3F_2^o$-$^3F_3^o$ transition formed the prime example. Because of its large difference between the g- and the g'-factors, the Zeeman components were well separated and the enhanced dispersion at the low transition energy allowed single Zeeman

Table 6.4: Parameters used for the g-factor model fit in figure 6.5. The g-factors were calculated using the AMBiT code [99].

Transition	E_0 (eV)	g	g'	w (10^{-5} eV)	$a_{-1,1}$ (arb. units)	a_0 (arb. units)
$^3F^o_2$-$^3F^o_3$	2.567818(4)	0.667	1.051	6.27(7)	0.0201(6)	0.130(2)
$^3H_4$-$^1G_4$	2.780970(6)	0.917	0.995	7.7(2)	0.0049(4)	0.032(1)
$^1G_4$-$^3F_4$	2.845258(3)	0.995	1.138	8.6(2)	0.017(1)	0.101(2)
$^1D_2$-$^3F_3$	2.871827(2)	1.132	1.083	8.1(1)	0.0082(4)	0.0460(6)
$^3H_5$-$^3H_6$	2.930971(2)	1.033	1.164	8.4(1)	0.0481(9)	0.284(5)
$^3F_3$-$^3F_4$	3.163403(2)	1.083	1.138	9.6(2)	0.0056(3)	0.0277(5)
$^1D_2$-$^3F_2$	3.395564(9)	1.132	0.847	12.7(4)	0.018(2)	0.047(2)
$^1F^o_3$-$^3F^o_4$	3.763971(5)	1.032	1.250	16.3(3)	0.0181(4)	0.074(1)
$^3H_4$-$^3H_5$	3.818365(5)	0.917	1.033	17.0(4)	0.0063(3)	0.0271(5)

Table 6.5: Best fit parameters for the g-factor fit. This time the g and g' were optimized as well. In case of the $^3F_3$-$^3F_4$ g'-factor, the fit did not converge due to strong correlations between the parameters. Instead, the value determined from transition $^1G_4$-$^3F_4$ was used.

Transition	E_0 (eV)	g	g'	w (10^{-5} eV)	$a_{-1,1}$ (arb. units)	a_0 (arb. units)
$^3F^o_2$-$^3F^o_3$	2.567818(4)	0.668(9)	1.045(8)	6.19(7)	0.0205(6)	0.130(2)
$^3H_4$-$^1G_4$	2.780970(6)	0.77(2)	0.85(2)	7.0(2)	0.0040(5)	0.030(1)
$^1G_4$-$^3F_4$	2.845258(3)	0.84(2)	0.99(2)	8.4(1)	0.0171(7)	0.098(1)
$^1D_2$-$^3F_3$	2.871827(2)	0.92(14)	0.97(7)	8(1)	0.0085(1)	0.047(8)
$^3H_5$-$^3H_6$	2.930971(2)	1.031(4)	1.155(4)	9.6(1)	0.0427(6)	0.246(3)
$^3F_3$-$^3F_4$	3.163403(2)	0.90(3)	0.99(2)*	7.5(5)	0.0069(5)	0.035(2)
$^1D_2$-$^3F_2$	3.395564(9)	1.36(6)	1.09(6)	12.3(4)	0.014(2)	0.045(2)
$^1F^o_3$-$^3F^o_4$	3.763971(5)	1.03(2)	1.24(2)	16.7(7)	0.0179(8)	0.072(3)
$^3H_4$-$^3H_5$	3.818365(5)	0.82(5)	0.95(4)	15(1)	0.0072(6)	0.030(6)

components to be resolved. The fit values gained from this transition are in perfect agreement with the theoretical predictions.

6.3 Ritz combinations in Ir^{17+}

The energy of α-sensitive transitions in Ir^{17+} can only be determined if at least one inter-configuration E1 transition is identified. They do not contribute to a smooth energy scaling as M1 transitions and could not be observed in the high-resolution spectra at the current level of statistics as they are much weaker than M1 transitions. Therefore, the methods presented above could not be used to identify E1 transitions in the available spectra without additional dedicated measurements. A complementary approach was the search for closed transition cycles, called Ritz combinations [100]. These combinations could be

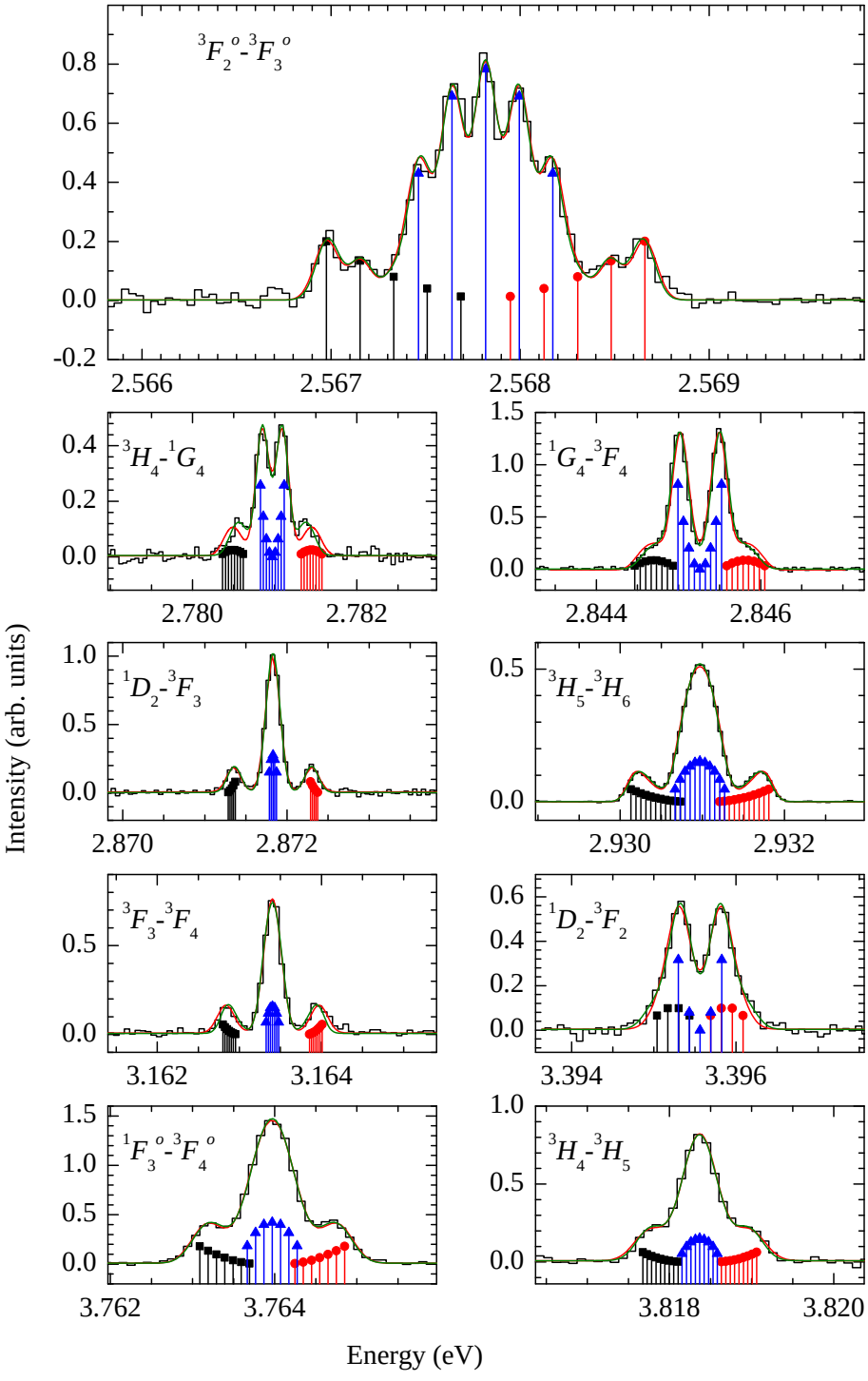

Figure 6.5: g-factor model fit to the spectral lines identified in section 6.1. To confirm the identification, calculated g,g'-factors have been used to predict the red line. The theoretical Zeeman pattern is represented by the symbols (black squares: $\Delta m = +1$, blue triangles: $\Delta m = 0$, red circles: $\Delta m = -1$). The best fitting assignment is depicted. For comparison, an additional fit using free g,g'-factors has been performed (green line). The fit residuals can be seen in figure 6.6.

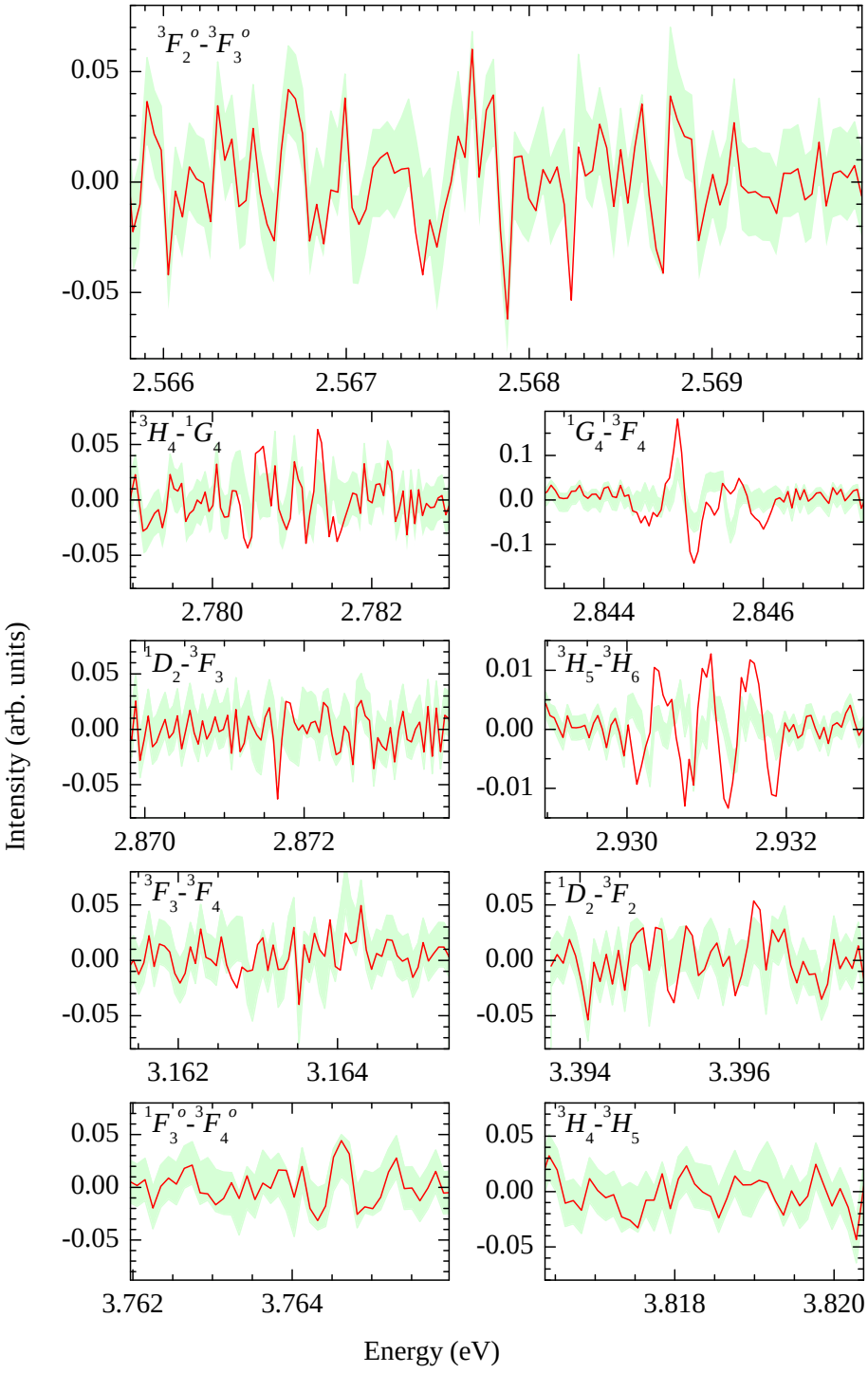

Figure 6.6: Fit residuals of the g-factor model fits. The green band represents the free g-factor fits with a width corresponding to the standard deviation of the noise. The model fits using the calculated g-factors are drawn in red. For most cases the two fits are in good agreement. The small deviations can be explained by uncertainties in the calculated g-factors or a slight decrease of the magnetic field strength over time.

Table 6.6: Transition energies following from identifications by Ritz combinations. It has to be distinguished between two mutually excluding cases: Either the Ritz-combination in equation (6.10) is correct or the one in equation (6.11). The two cases yield different energies for the α-sensitive $4f^{12}5s^2\,{}^3H_6$-$4f^{13}5s^1\,{}^3F_4^o$ transition in bold print. Theoretical predictions for these transition energies are listed for comparison. Transition energies are given in eV.

Transition	Case (6.10)	Case (6.11)	FSCC	CIDFS	COWAN	CI
${}^3P_1$-${}^3F_2$	5.4691(5)	5.4691(5)	5.51	5.66	5.47	5.93
${}^3P_1$-${}^1D_2$	2.07395(7)	2.07395(7)	2.11	2.12	1.99	2.27
${}^3F_4$-${}^3F_4^o$	5.1623(4)	–	4.16	4.75	5.25	5.61
${}^3F_3$-${}^1F_3^o$	4.5619(3)	5.1623(4)	3.55	4.13	4.76	5.01
${}^1G_4$-${}^1F_3^o$	–	4.8441(4)	3.23	3.77	4.44	4.64
${}^3H_6$-${}^3F_4^o$	**4.0392(4)**	**4.6397(4)**	**3.00**	**3.64**	**4.22**	**4.38**

found by adding up or subtracting the transition energies of observed lines in a way that the result is zero within the measurement uncertainty. Using the identified M1 transition energies with ppm accuracy in table 5.4, the remaining transitions were extracted from table 5.3 with uncertainties of 0.02 nm. The condition was that the sum of transition energies was closer to zero than the squared sum of their 2σ. If a Ritz-combination contained at least one of the identified transitions, other unknown, but connected transitions could be assigned.

The three Ritz combinations depicted in figure 6.7 were found in the measured spectra. The triple contained the $4f^{12}5s^2\,{}^1D_2$-${}^3F_2$ transition, therefore, the only possible arrangement was

$$E(4f^{12}5s^2\,{}^1D_2 - {}^3F_2) - E({}^3F_2 - {}^3P_1) + E({}^3P_1 - {}^1D_2) = 0.0004(12)\,\text{eV}, \tag{6.9}$$

containing only M1 transitions. The probability of a false positive result was estimated analogously to section 6.1 and amounted to approximately 0.16 for a combination including two unknown transitions. The established identifications were within the obtained uncertainty of the FSCC predictions for M1 transition energies as can be seen in table 6.6.

The other two Ritz combinations

$$\begin{aligned} &E(4f^{12}5s^2\,{}^3F_3 - {}^3F_4) + E(4f^{12}5s^2\,{}^3F_4 - 4f^{13}5s^1\,{}^3F_4^o) \\ -&E(4f^{13}5s^1\,{}^3F_4^o - {}^1F_3^o) - E(4f^{13}5s^1\,{}^1F_3^o - 4f^{12}5s^2\,{}^3F_3) = 0.0002(4)\,\text{eV}, \end{aligned} \tag{6.10}$$

and

$$\begin{aligned} E(4f^{12}5s^2\,{}^3F_3 - 4f^{13}5s^1\,{}^1F_3^o) - E(4f^{13}5s^1\,{}^1F_3^o - 4f^{12}5s^2\,{}^1G_4) \\ +E(4f^{12}5s^2\,{}^1G_4 - {}^3F_4) - E(4f^{12}5s^2\,{}^3F_4 - {}^3F_3) = 0.0000(4)\,\text{eV}, \end{aligned} \tag{6.11}$$

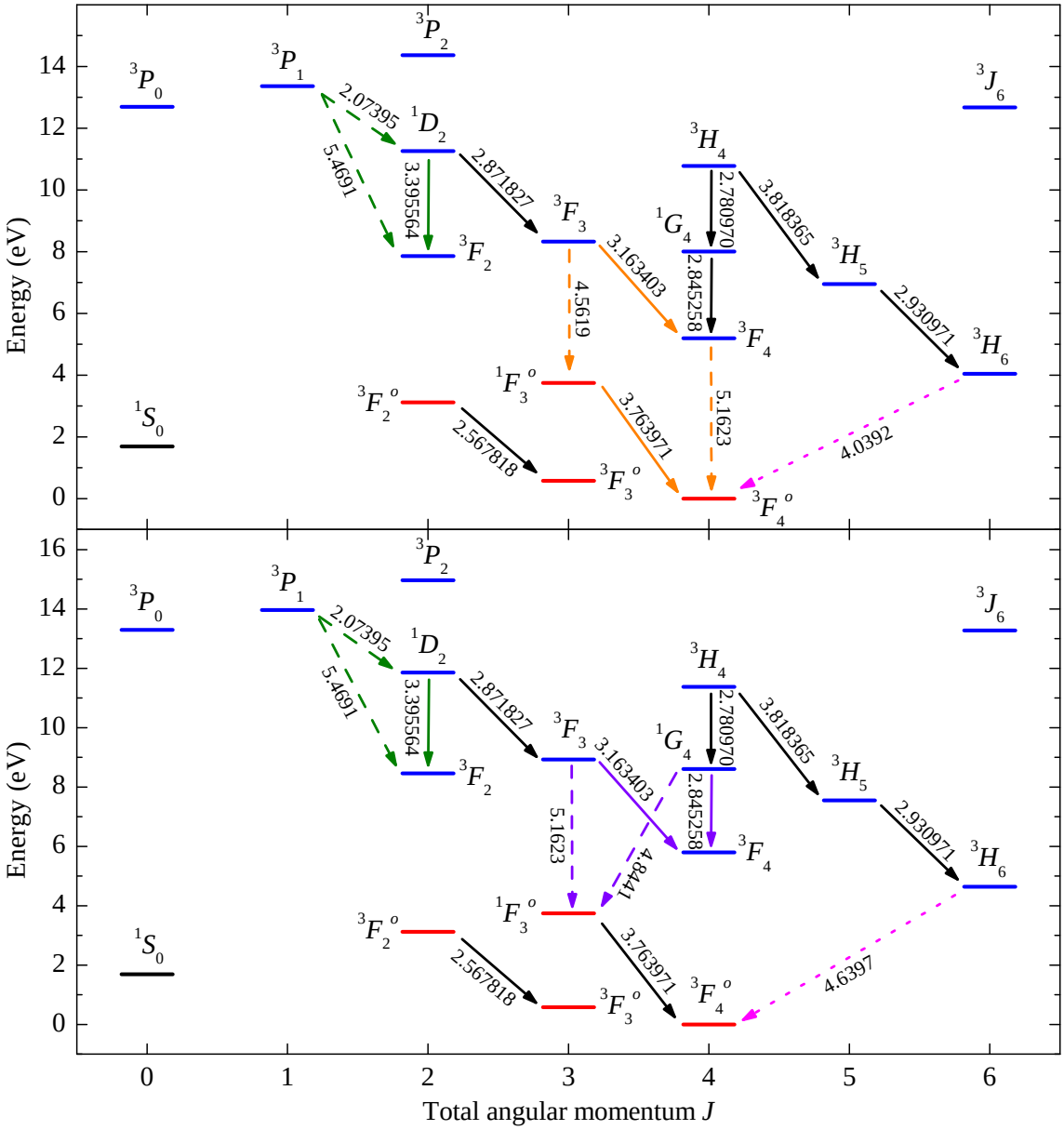

Figure 6.7: Grotrian diagrams of Ir^{17+}. Transitions identified in sections 6.1 and 6.2 are marked by solid arrows. Transition energies (in eV) are given next to the corresponding arrow, with the last digit being significant. Additional M1 transitions (dashed green) could be identified via a Ritz-combination consisting of three transitions. The orange and purple colored Ritz combinations contradict each other in the $4f^{12}5s^2\,{}^3F_3$-$4f^{13}5s^1\,{}^1F_3^o$ transition. If one of these two combinations is true, the sought-after α-sensitive clock transition $4f^{12}5s^2\,{}^3H_6$-$4f^{13}5s^1\,{}^3F_4^o$ (dotted magenta) can be inferred, although it could not be directly observed. The top and bottom diagrams show the two different cases.

contained E1 transitions. However, they excluded each other since the $4f^{12}5s^2\,{}^3F_3$-$4f^{13}5s^1\,{}^1F_3^o$ transition was assigned either to the spectral line at 4.5619(3) eV for equation (6.10) or to 5.1623(4) eV for equation (6.11). The *a priori* probability that both combinations came about randomly was only approximately 0.01. Most calculations, except for the CI results from [25], seemed to favor the first case. However, if the large discrepancy between the different calculations on the order of 1 eV is taken as theoretical uncertainty, no theory can be discriminated without further evidence. Since no definite decision on one of them could be made based on the available data, both scenarios are listed in table 6.6. In both cases, the established network of M1 transitions could be used for the tentative energy of the α-sensitive clock transition $4f^{12}5s^2\,{}^3H_6$-$4f^{13}5s^1\,{}^3F_4^o$. The inferred energy was blue shifted compared to its FSCC prediction, but in both cases stayed at the edge of the laser-accessible range, at vacuum wavelengths of 267.22(2) nm or 306.95(3) nm.

Additional measurements have to be performed to solve this ambiguity. A high-resolution measurement such as presented in section 5.4 can be performed to decide which of the two scenarios is true. The 5.1623(4) eV transition could for example be measured at the optimum electron beam energy to increase the accuracy and therefore reduce the probability for a false positive. Simultaneously, the Zeeman structure could be resolved, which allowed for an identification by the g-factor model. The remaining unidentified spectral lines could belong to E1 transitions which do not contribute to Ritz-combinations or to M1 transitions within higher energy configurations.

6.4 Evaluation of atomic structure calculations

Atomic structure calculations in complex many-electron HCI remain largely untested. An important benchmark could be provided by the presented transition identifications which will help to improve the accuracy for future calculations in these systems. This is of particular importance for the determination of the energy of the state $4f^{14}\,{}^1S_0$, since no optical transitions can be directly observed in an EBIT connecting to other configurations of the atomic structure. Moreover, it will simplify first identifications in the numerous proposed HCI where the atomic structure is unknown if the uncertainty of the different atomic structure codes is quantified.

A comparison between the identified transition energies and the various atomic structure codes which contributed to this work (for description see section 2.2) can be found in figure 6.8. The problem of identifying transition energies between theory and experiment can be highlighted with the example of the $4f^{12}5s^2\,{}^1D_2$-${}^3F_3$ transition, for which the scatter between theories amounts to 0.4 eV or 55 nm. The different codes could be evaluated by determining their average deviation compared to the data and the associated standard deviation. These quantities can be related to the average spectral separation of the tran-

sitions on the order of approximately 0.1 eV. It was notable that COWAN, FAC, and CI [25] predictions seem to be systematically blue shifted. For the evaluated codes, FSCC proved most suitable to predict fine structure transitions in the investigated HCI. A systematic shift could not be observed and the standard deviation of approximately 0.03 eV for the FSCC code was at least a factor of three better than for other methods. Even a comparison between data and FSCC calculation would not have yielded a completely correct spectral line assignment, but the FSCC method is certainly the best starting point when dealing with unknown and complex HCI. This could be due to the characteristic treatment of electron correlations as explained in section 2.2.2.

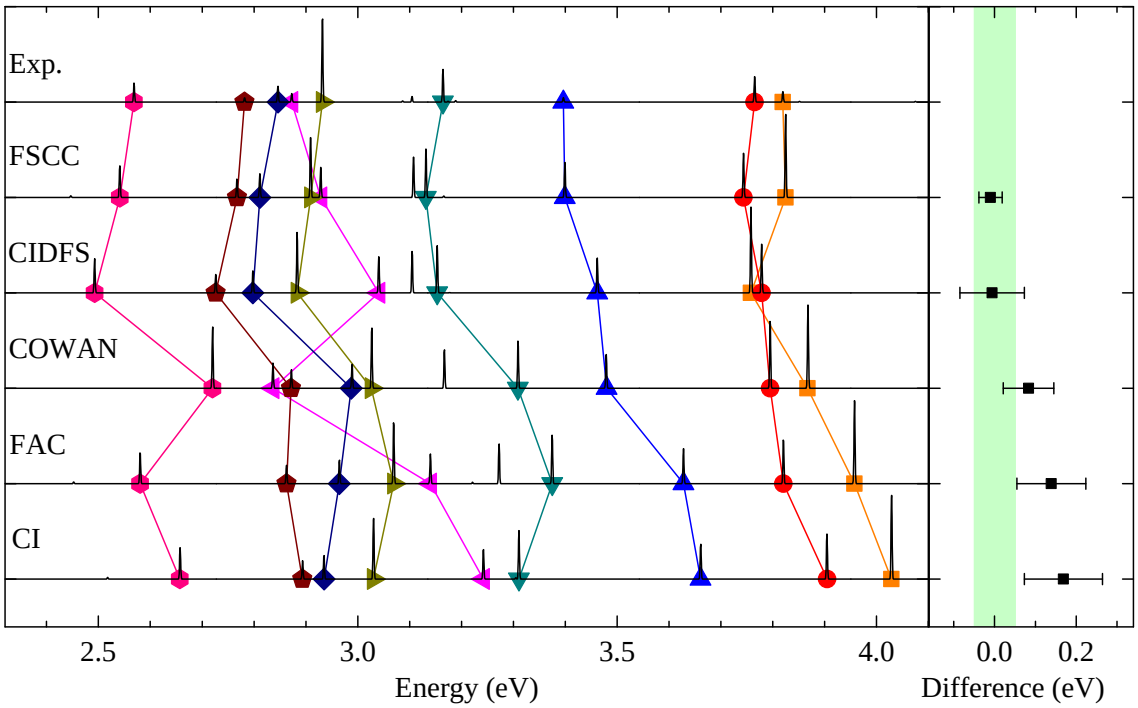

Figure 6.8: Left: Comparison between data and the different atomic structure codes contributed to this work. For the calculations, artificial spectra have been generated using Einstein A-coefficients as intensities. The same transitions are linked by colored lines. The symbols and colors correspond the ones used in figure 6.3. Right: Average deviation between experiment and theory (black squares) and their standard deviation (error bars). The average energy separation of spectral lines is indicated by the light green band.

Chapter 7

Conclusion and outlook

Highly charged ions (HCI) have recently become subject of a variety of theoretical studies investigating their advantages for frequency metrology. Due to their compact electronic wavefunctions and their correspondingly small polarizabilities, perturbations caused by external fields are strongly suppressed. Tens of forbidden optical transitions in different ions have been proposed in the past four years [24–34, 53] as frequency standards with predicted relative frequency uncertainties below 10^{-19}. This would represent an order of magnitude improvement compared to state of the art clocks [54, 55]. An interesting application is the comparison of two HCI frequency standards for testing a possible variation of the fine structure constant α. Electrons in HCI experience strong relativistic effects and thus have a strongly enhanced sensitivity to an α variation. Since there has been evidence claimed for an α variation based on astrophysical observations [15], complementary laboratory tests are imperative.

However, the most promising HCI candidates are experimentally unknown. Many of the proposed ions exhibit complex electronic structures featuring many electrons in open shells, which hampers accurate theoretical predictions. A prime example is the Nd-like Ir^{17+} ion, which offers a unique level crossing of the $4f$ and the $5s$ shells. This implies that between the lowest energy configurations $4f^{12}5s^2$, $4f^{13}5s^1$, and the $4f^{14}$ optical forbidden M2/E3 transitions are possible. The transition between $4f^{14}\,{}^1S_0$-$4f^{13}5s^1\,{}^3F_3^o$ and $4f^{12}5s^2\,{}^3H_6$-$4f^{13}5s^1\,{}^3F_4^o$ has the highest sensitivity to an α variation ever predicted for a stable atomic system [25]. Unfortunately, the uncertainty on the theoretical wavelengths of these transitions is estimated to be on the order of 10 nm. Hence, laser spectroscopy searches of this transition for metrology applications cannot be based solely on these predictions. Therefore, the aim of this work was the experimental exploration of the complex electronic structures of W, Re, Os, Ir, and Pt ions close to the predicted level crossing in order to provide crucial data for planned studies on the variation of α.

To that end, the isoelectronic Nd-like ions W, Re, Os, Ir, and Pt were produced and trapped in the Heidelberg electron beam ion trap (EBIT). The injected atoms were sequentially ionized to the desired charge state by a mono-energetic electron beam focused down to approximately 50 µm by a strong magnetic field. Ions in the EBIT were radially trapped by the electron beam space charge potential and axially by a potential well formed by a set of drift tubes. To produce and identify the Nd-like charge states, the electron beam energy was tuned in the range of 170-900 eV at currents of 10-40 mA. While trapped, the HCI are excited by electron collisions to states close to the continuum and spontaneously emit photons when cascading down to the ground state.

The fluorescence light emitted in the optical regime, between approximately 250-650 nm, was analyzed with a Czerny-Turner spectrometer. Two classes of spectra were acquired. First, overview spectra were taken, using a 300 lines/mm diffraction grating, while stepping up the electron beam energy of the EBIT. The resulting spectral maps covered several charge states and hundreds of transitions. In order to identify the Nd-like charge state and to discriminate spectral lines that emerged from neighboring charge states, ionization potentials of Ir^{13+} to Ir^{22+} were obtained experimentally and compared to theoretical predictions. In this manner, 85 formerly unobserved spectral lines could be assigned to Nd-like ions.

In a second measurement run, the brightest Ir^{17+} transitions were observed using a 2400 lines/mm grating. The employed measurement scheme allowed for accuracies as good as 0.2 ppm, which is an outstanding performance in the field of optical EBIT spectroscopy [89]. Aided by the enhanced resolution, the Zeeman splitting caused by the magnetic field of the EBIT could be observed with a maximum resolving power of 40 800.

This work was supported by highly advanced atomic structure calculations provided by collaborating theoreticians [59, 62, 68] and other sources [25], including those performed using Fock space coupled cluster, multiconfiguration interaction Dirac-Fock-Sturmian, the COWAN code, and the Flexible Atomic Code. The deviations predicted by the above theory models were on the same order as the average separation of observed spectral lines of approximately 0.1 eV for M1 transitions, and could be as high as 1 eV for E1 transitions. Hence, the straightforward approach of assigning spectral lines by comparison with theory could not be applied.

Over the course of the work presented in this thesis, an alternative approach through the analysis of the characteristic scaling of intra-configuration M1 transition energies with the atomic number Z was developed. From theoretical predictions, a smooth scaling of the M1 transition energies as a function of the atomic number Z was expected such that many of these isoelectronic transitions would stay in the observable optical range along the whole sequence. The theoretical scaling functions were well represented by second order polynomials. The same polynomial dependencies could be recovered in the measured

spectra. The nine brightest spectral lines of each observed ion contributed to these scalings, identifying them as M1 transitions. The theoretical scaling curves were compared with the experimental ones and by a χ^2-minimization procedure, each scaling function could be unambiguously identified and hence the 45 underlying isoelectronic transitions. The demonstrated method can be applied to many other of the proposed HCI and provides a reliable and efficient identification tool. The advantage of identifying transitions by their isoelectronic energy scaling can be demonstrated through the forbidden $4f^{12}5s^{2\,3}F_4$-$4f^{12}5s^{2\,3}H_6$ transition in W^{14+} and Hf^{12+} suggested as next generation frequency standard in [30]. Although its transition rate is too low to be directly observed in an EBIT, its energy could be inferred due to the acquired knowledge of the W^{14+} level structure. By following the obtained scaling functions, this transition energy could be extrapolated to that of the Hf^{12+} ion. The determined transition energies were more than two orders of magnitude more accurate than their theoretical predictions and thus open up these HCI for metrology applications.

An independent test of this method was performed using the high resolution spectra acquired of Ir^{17+} ions. Their Zeeman-split line shapes were modeled based on g-factors calculated using the AMBiT code [99]. The modeled results resembled the observed line shapes well. The resulting identifications were in perfect agreement with the previously assigned M1 transitions and thus validated the scaling method. This was an essential step to ensure that the assigned charge state was correct, since the small differences in production energies for the ions could still leave an uncertainty in the identifications. The stark changes in the Zeeman pattern between charge states removed this last ambiguity.

The now identified M1 transitions in the investigated ion species formed a basis which allowed for further identifications using Ritz's combination principle. If combinations of transition energies can be balanced out to zero, closed transition cycles are found. In positively tested combinations, unidentified spectral lines can be assigned through their connection to identified transitions. In this way, two more M1 transitions in Ir^{17+} were found. The Ritz combination method also had to be applied to find the α sensitive forbidden M2/E3 transitions by assigning E1 transitions, since they do not offer smooth energy scalings and are too weak for the performed high resolution measurements. Indeed, two possible combinations were uncovered, each with a likelihood of 84%: the E1 candidates $4f^{12}5s^{2\,3}F_4$-$4f^{13}5s^{1\,3}F_4^o$, $4f^{12}5s^{2\,3}F_3$-$4f^{13}5s^{1\,1}F_3^o$, and $4f^{12}5s^{2\,1}G_4$-$4f^{13}5s^{1\,1}F_3^o$. Although the two cases are mutually exclusive, the chance that both are wrong is on the order of few 1%. In both cases, two possible values for the transition energy of the sought after forbidden M2/E3 transition $4f^{12}5s^{2\,3}H_6$-$4f^{13}5s^{1\,3}F_4^o$ could be inferred. This result significantly reduces the complexity of the problem. The ambiguity in the determination of the E1 transition energy can be completely solved by performing dedicated measure-

ments of the three conjectured transitions using the high accuracy scheme presented in this work.

The specific and experimentally determined candidates for accurate or α sensitive frequency standards are of particular relevance in view of the recent breakthrough achieved by L. Schmöger [40] and co-workers. For the first time HCI could be trapped in a cryogenic Paul trap CryPTEx [41, 42]. By linking the HYPER EBIT [74] up to CryPTEx using an optimized beamline [101], HCI have been successfully decelerated and implanted in a laser cooled Be^+ ion crystals stored in CryPTEx. Temperatures of HCI on the order of 100 mK have been demonstrated in this setup [40] which is a leap of many orders of magnitude compared to typical temperatures in an EBIT. With the capability of trapping single HCI at rest in space at these low temperatures, an essential prerequisite for frequency metrology applications is met. The strongly forbidden transitions $4f^{12}5s^2\,{}^3F_4$-$4f^{12}5s^2\,{}^3H_6$ in W^{14+} and Hf^{12+}, and $4f^{12}5s^2\,{}^3H_6$-$4f^{13}5s^1\,{}^3F_4^o$ in Ir^{17+} inferred in this work can be determined with high accuracy by quantum logic spectroscopy methods similar to those already demonstrated in metrology applications [45, 23].

Table 7.1: Summary of the main results of this work. The transition energies and wavelengths of the two proposed E2 frequency standards in Hf^{12+} and W^{14+} were inferred (bold). For Ir^{17+}, two possible but mutually exclusive identifications of E1 transitions are listed. For both cases, transition energies for the unobserved α-sensitive M2/E3 transition were inferred (bold).

Ion	Transition	Type	Energy(eV)	Wavelength (nm)	
				Vacuum	Air
Hf^{12+}	$\boldsymbol{4f^{12}5s^2\,{}^3F_4}$-$\boldsymbol{{}^3H_6}$	**E2**	**0.934(6)**	**1327(9)**	**1327(9)**
W^{14+}	$\boldsymbol{4f^{12}5s^2\,{}^3F_4}$-$\boldsymbol{{}^3H_6}$	**E2**	**1.0140(2)**	**1222.7(2)**	**1222.4(2)**
	——— Case 1 ———				
Ir^{17+}	$4f^{12}5s^2\,{}^3F_4$-$4f^{13}5s^1\,{}^3F_4^o$	E1	5.1623(4)	240.17(2)	240.10(2)
	$4f^{12}5s^2\,{}^3F_3$-$4f^{13}5s^1\,{}^1F_3^o$	E1	4.5619(3)	271.78(2)	271.70(2)
	$\boldsymbol{4f^{12}5s^2\,{}^3H_6}$-$\boldsymbol{4f^{13}5s^1\,{}^3F_4^o}$	**M2/E3**	**4.0392(4)**	**306.95(3)**	**306.86(3)**
	——— Case 2 ———				
	$4f^{12}5s^2\,{}^3F_3$-$4f^{13}5s^1\,{}^1F_3^o$	E1	5.1623(4)	240.17(2)	240.10(2)
	$4f^{12}5s^2\,{}^1G_4$-$4f^{13}5s^1\,{}^1F_3^o$	E1	4.8441(4)	255.95(2)	255.87(2)
	$\boldsymbol{4f^{12}5s^2\,{}^3H_6}$-$\boldsymbol{4f^{13}5s^1\,{}^3F_4^o}$	**M2/E3**	**4.6397(4)**	**267.22(2)**	**267.15(2)**

Bibliography

[1] Wikipedia. Standard model of elementary particles (2006). URL http://commons.wikimedia.org/wiki/File:Standard_Model_of_Elementary_Particles.svg. [Online; accessed 15/12/2014].

[2] Sommerfeld, A. Zur Quantentheorie der Spektrallinien. *Annalen der Physik* **356**, 1–94 (1916). URL http://dx.doi.org/10.1002/andp.19163561702.

[3] Bohr, N. I. On the constitution of atoms and molecules. *Philosophical Magazine Series 6* **26**, 1–25 (1913). URL http://dx.doi.org/10.1080/14786441308634955.

[4] Mohr, P. J., Taylor, B. N. & Newell, D. B. (2011), "The 2010 CODATA Recommended Values of the Fundamental Physical Constants" (Web Version 6.3). This database was developed by J. Baker, M. Douma, and S. Kotochigova. Available: http://physics.nist.gov/constants. National Institute of Standards and Technology, Gaithersburg, MD 20899., [Online; accessed 17/12/2014].

[5] Hanneke, D., Fogwell, S. & Gabrielse, G. New measurement of the electron magnetic moment and the fine structure constant. *Phys. Rev. Lett.* **100**, 120801 (2008). URL http://link.aps.org/doi/10.1103/PhysRevLett.100.120801.

[6] Aoyama, T., Hayakawa, M., Kinoshita, T. & Nio, M. Tenth-order QED contribution to the electron $g-2$ and an improved value of the fine structure constant. *Phys. Rev. Lett.* **109**, 111807 (2012). URL http://link.aps.org/doi/10.1103/PhysRevLett.109.111807.

[7] Kolb, E., Perry, M. & Walker, T. Time variation of fundamental constants, primordial nucleosynthesis, and the size of extra dimensions. *Phys. Rev. D* **33**, 869–871 (1986). URL http://link.aps.org/doi/10.1103/PhysRevD.33.869.

[8] Uzan, J.-P. The fundamental constants and their variation: observational and theoretical status. *Rev. Mod. Phys.* **75**, 403–455 (2003). URL http://link.aps.org/doi/10.1103/RevModPhys.75.403.

[9] Ade, P. A. R. *et al.* Planck intermediate results. XXIV. Constraints on variation of fundamental constants. *ArXiv e-prints* (2014). URL http://adsabs.harvard.edu/abs/2014arXiv1406.7482A. 1406.7482.

[10] Dunbar, D. and Pixley, R. and Wenzel, W. and Whaling, W. The 7.68-Mev State in C^{12}. *Phys. Rev.* **92**, 649–650 (1953). URL http://link.aps.org/doi/10.1103/PhysRev.92.649.

[11] Oberhummer, H., Csótó, A. & Schlattl, H. Stellar production rates of carbon and its abundance in the universe. *Science* **289**, 88–90 (2000). URL http://www.sciencemag.org/content/289/5476/88.abstract. http://www.sciencemag.org/content/289/5476/88.full.pdf.

[12] Dirac, P. A. M. The Cosmological Constants. *Nature* **139**, 323 (1937). URL http://dx.doi.org/10.1038/139323a0.

[13] Dirac, P. A. M. Cosmological models and the large numbers hypothesis. *Proceedings of the Royal Society of London A: Mathematical, Physical and Engineering Sciences* **338**, 439–446 (1974).

[14] Gamow, G. Electricity, gravity, and cosmology. *Phys. Rev. Lett.* **19**, 759–761 (1967). URL http://link.aps.org/doi/10.1103/PhysRevLett.19.759.

[15] Webb, J. K. *et al.* Indications of a spatial variation of the fine structure constant. *Phys. Rev. Lett.* **107**, 191101 (2011). URL http://link.aps.org/doi/10.1103/PhysRevLett.107.191101.

[16] King, J. A. *et al.* Spatial variation in the fine-structure constant – new results from VLT/UVES. *Monthly Notices of the Royal Astronomical Society* **422**, 3370–3414 (2012). URL http://mnras.oxfordjournals.org/content/422/4/3370.abstract. http://mnras.oxfordjournals.org/content/422/4/3370.full.pdf+html.

[17] Webb, J., Flambaum, V., Churchill, C., Drinkwater, M. & Barrow, J. Search for time variation of the fine structure constant. *Phys. Rev. Lett.* **82**, 884–887 (1999). URL http://link.aps.org/doi/10.1103/PhysRevLett.82.884.

[18] Molaro, P. *et al.* The uves large program for testing fundamental physics i. bounds on a change in α towards quasar he 2217-2818. *A& A* **555**, A68 (2013). URL http://dx.doi.org/10.1051/0004-6361/201321351.

[19] Songaila, A. & Cowie, L. L. Constraining the variation of the fine-structure constant with observations of narrow quasar absorption lines. *The Astrophysical Journal* **793**, 103 (2014). URL http://stacks.iop.org/0004-637X/793/i=2/a=103.

[20] Berengut, J. C. & Flambaum, V. V. Manifestations of a spatial variation of fundamental constants in atomic and nuclear clocks, oklo, meteorites, and cosmological phenomena. *EPL (Europhysics Letters)* **97**, 20006 (2012). URL http://stacks.iop.org/0295-5075/97/i=2/a=20006.

[21] Huntemann, N. *et al.* Improved limit on a temporal variation of m_p/m_e from comparisons of Yb^+ and cs atomic clocks. *Phys. Rev. Lett.* **113**, 210802 (2014). URL http://link.aps.org/doi/10.1103/PhysRevLett.113.210802.

[22] Godun, R. M. *et al.* Frequency ratio of two optical clock transitions in $^{171}Yb^+$ and constraints on the time variation of fundamental constants. *Phys. Rev. Lett.* **113**, 210801 (2014). URL http://link.aps.org/doi/10.1103/PhysRevLett.113.210801.

[23] Rosenband, T. *et al.* Frequency Ratio of Al^+ and Hg^+ Single-Ion Optical Clocks; Metrology at the 17th Decimal Place. *Science* **319**, 1808–1812 (2008). URL http://dx.doi.org/10.1126/science.1154622.

[24] Berengut, J. C., Dzuba, V. A. & Flambaum, V. V. Enhanced laboratory sensitivity to variation of the fine-structure constant using highly charged ions. *Phys. Rev. Lett.* **105**, 120801 (2010). URL http://link.aps.org/doi/10.1103/PhysRevLett.105.120801.

[25] Berengut, J. C., Dzuba, V. A., Flambaum, V. V. & Ong, A. Electron-hole transitions in multiply charged ions for precision laser spectroscopy and searching for variations in α. *Phys. Rev. Lett.* **106**, 210802 (2011). URL http://link.aps.org/doi/10.1103/PhysRevLett.106.210802.

[26] Berengut, J. C., Dzuba, V. A., Flambaum, V. V. & Ong, A. Highly charged ions with E1, M1, and E2 transitions within laser range. *Phys. Rev. A* **86**, 022517 (2012). URL http://link.aps.org/doi/10.1103/PhysRevA.86.022517.

[27] Berengut, J. C., Dzuba, V. A., Flambaum, V. V. & Ong, A. Optical transitions in highly charged californium ions with high sensitivity to variation of the fine-structure constant. *Phys. Rev. Lett.* **109**, 070802 (2012). URL http://link.aps.org/doi/10.1103/PhysRevLett.109.070802.

[28] Derevianko, A., Dzuba, V. A. & Flambaum, V. V. Highly charged ions as a basis of optical atomic clockwork of exceptional accuracy. *Phys. Rev. Lett.* **109**, 180801 (2012). URL http://link.aps.org/doi/10.1103/PhysRevLett.109.180801.

[29] Safronova, M. S. *et al.* Highly charged Ag-like and In-like ions for the development of atomic clocks and the search for α variation. *Phys. Rev. A* **90**, 042513 (2014). URL http://link.aps.org/doi/10.1103/PhysRevA.90.042513.

[30] Dzuba, V. A., Derevianko, A. & Flambaum, V. V. High-precision atomic clocks with highly charged ions: Nuclear-spin-zero f^{12}-shell ions. *Phys. Rev. A* **86**, 054501 (2012). URL http://link.aps.org/doi/10.1103/PhysRevA.86.054501.

[31] Dzuba, V. A., Flambaum, V. V. & Katori, H. Optical clock sensitive to variation of the fine structure constant based on the Ho^{14+} ion (2014). URL http://arxiv.org/abs/1411.0775. 1411.0775.

[32] Safronova, M. S. *et al.* Atomic properties of Cd-like and Sn-like ions for the development of frequency standards and search for the variation of the fine-structure constant. *Phys. Rev. A* **90**, 052509 (2014). URL http://link.aps.org/doi/10.1103/PhysRevA.90.052509.

[33] Yudin, V. . I., Taichenachev, A. . V. & Derevianko, A. Magnetic-Dipole Transitions in Highly Charged Ions as a Basis of Ultraprecise Optical Clocks. *Physical Review Letters* **113** (2014). URL http://dx.doi.org/10.1103/physrevlett.113.233003.

[34] Schiller, S. Hydrogenlike Highly Charged Ions for Tests of the Time Independence of Fundamental Constants. *Physical Review Letters* **98**, 180801+ (2007). URL http://dx.doi.org/10.1103/physrevlett.98.180801.

[35] Crespo López-Urrutia, J. R., Dorn, A., Moshammer, R. & Ullrich, J. The Freiburg Electron Beam Ion Trap/Source Project FreEBIT. *Physica Scripta* **1999**, 502 (1999). URL http://stacks.iop.org/1402-4896/1999/i=T80B/a=135.

[36] Czerny, M. & Turner, A. F. Über den Astigmatismus bei Spiegelspektrometern. *Zeitschrift für Physik* **61**, 792–797 (1930). URL http://dx.doi.org/10.1007/BF01340206.

[37] Boyle, W. S. & Smith, G. E. Charge coupled semiconductor devices. *Bell System Technical Journal* **49**, 587–593 (1970). URL http://dx.doi.org/10.1002/j.1538-7305.1970.tb01790.x.

[38] Draganić, I. *et al.* High Precision Wavelength Measurements of QED-Sensitive Forbidden Transitions in Highly Charged Argon Ions. *Physical Review Letters* **91**, 183001+ (2003). URL http://dx.doi.org/10.1103/physrevlett.91.183001.

[39] Soria Orts, R. *et al.* Exploring Relativistic Many-Body Recoil Effects in Highly Charged Ions. *Phys. Rev. Lett.* **97**, 103002+ (2006). URL http://dx.doi.org/10.1103/physrevlett.97.103002.

[40] Schmöger, L. *et al. Science* (2015). 12/03/15.

[41] Schwarz, M. *et al.* Cryogenic linear paul trap for cold highly charged ion experiments. *Review of Scientific Instruments* **83**, 083115 (2012). URL http://link.aip.org/link/?RSI/83/083115/1.

[42] Schwarz, M. Lasermanipulation von rotationsgekuhlten Molekülionen in einer neuen kryogenen Paul-Falle (2012). Ph.D. Thesis. Ruprecht-Karls-Universität, Heidelberg.

[43] Versolato, O. O. *et al.* Cold highly charged ions in a cryogenic Paul trap. *Hyperfine Interactions* **214**, 189–194 (2013). URL http://dx.doi.org/10.1007/s10751-013-0806-9.

[44] Windberger, A. *et al.* Coulomb crystals in a cryogenic paul trap for sympathetic cooling of molecular ions and highly charged ions. *AIP Conference Proceedings* **1521**, 250–256 (2013). URL http://scitation.aip.org/content/aip/proceeding/aipcp/10.1063/1.4796081.

[45] Schmidt, P. O. *et al.* Spectroscopy Using Quantum Logic. *Science* **309**, 749–752 (2005). URL http://dx.doi.org/10.1126/science.1114375.

[46] Currell, F. J. Physics of and with electron beam ion traps and sources EBIS/T (2012). URL https://indico.cern.ch/event/127522/contribution/40/material/slides/0.pdf. [Online; accessed 03/01/2015].

[47] Beyer, H. & Shevelko, V. *Introduction to the Physics of Highly Charged Ions*. Series in Atomic Molecular Physics (Taylor & Francis, 2002).

[48] Sansonetti, C. J., Kerber, F., Reader, J. & Rosa, M. R. Characterization of the far-ultraviolet spectrum of Pt/Cr-Ne hollow cathode lamps as used on the space telescope imaging spectrograph on board the hubble space telescope. *The Astrophysical Journal Supplement Series* **153**, 555 (2004). URL http://stacks.iop.org/0067-0049/153/i=2/a=555.

[49] Aglitskii, E. V., Boiko, V. A., Zakharov, S. M., Pikuz, S. A. & Faenov, A. Y. Observation in laser plasmas and identification of dielectron satellites of spectral lines of hydrogen- and helium-like ions of elements in the Na-V range. *Soviet Journal of Quantum Electronics* **4**, 500 (1974). URL http://stacks.iop.org/0049-1748/4/i=4/a=R16.

[50] Kramida, A., Yu. Ralchenko, Reader, J. & and NIST ASD Team. NIST Atomic Spectra Database (ver. 5.2), [Online]. Available: http://physics.nist.gov/asd

[2015, March 1]. National Institute of Standards and Technology, Gaithersburg, MD. (2014).

[51] Ludlow, A. D., Boyd, M. M., Ye, J., Peik, E. & Schmidt, P. O. Optical Atomic Clocks. *ArXiv e-prints* (2014). 1407.3493.

[52] Gillaspy, J. D. Highly charged ions. *Journal of Physics B: Atomic, Molecular and Optical Physics* **34**, R93–R130 (2001). URL http://dx.doi.org/10.1088/0953-4075/34/19/201.

[53] Safronova, M. S. *et al.* Highly charged ions for atomic clocks, quantum information, and search for α variation. *Phys. Rev. Lett.* **113**, 030801 (2014). URL http://link.aps.org/doi/10.1103/PhysRevLett.113.030801.

[54] Chou, C. W., Hume, D. B., Koelemeij, J. C. J., Wineland, D. J. & Rosenband, T. Frequency comparison of two high-accuracy Al^+ optical clocks. *Phys. Rev. Lett.* **104**, 070802 (2010). URL http://link.aps.org/doi/10.1103/PhysRevLett.104.070802.

[55] Bloom, B. J. *et al.* An optical lattice clock with accuracy and stability at the 10^{-18} level. *Nature* **506**, 71–75 (2014). URL http://dx.doi.org/10.1038/nature12941.

[56] Mukherjee, D. & Pal, S. *Adv. Quantum Chem* **20**, 292 (1989).

[57] Kaldor, U. & Eliav, E. High-accuracy calculations for heavy and super-heavy elements. *Adv. Quantum Chem* **31**, 313 – 336 (1998). URL http://www.sciencedirect.com/science/article/pii/S006532760860194X.

[58] Tel-Aviv Relativistic Atomic Fock Space coupled cluster code, written by E.Eliav, U.Kaldor and Y.Ishikawa (1990-2013).

[59] Borschevsky, A. Private communication.

[60] Tupitsyn, I. I. *et al. Phys. Rev. A* **68**, 022511 (2003).

[61] Tupitsyn, I. I. *et al.* Magnetic-dipole transition probabilities in b-like and be-like ions. *Phys. Rev. A* **72**, 062503 (2005). URL http://link.aps.org/doi/10.1103/PhysRevA.72.062503.

[62] Oreshkina, N. S. Private communication.

[63] Gu, M. F. The flexible atomic code. *Canadian Journal of Physics* **86**, 675–689 (2008).

[64] Johnson, W. Relativistic calculations for few-electron systems (2005). URL http://www3.nd.edu/~johnson/Publications/markup.pdf. [Online; accessed 29/01/2015].

[65] Bartlett, R. & Musiał, M. Coupled-cluster theory in quantum chemistry. *Reviews of Modern Physics* **79**, 291–352 (2007). URL http://dx.doi.org/10.1103/revmodphys.79.291.

[66] Coester, F. & Kümmel, H. Short-range correlations in nuclear wave functions. *Nuclear Physics* **17**, 477 – 485 (1960). URL http://www.sciencedirect.com/science/article/pii/0029558260901401.

[67] Cowan, R. D. *The theory of atomic structure and spectra*, vol. 3 (Univ of California Press, 1981).

[68] Safronova, U. I. Private communication.

[69] Lotz, W. Electron-impact ionization cross-sections and ionization rate coefficients for atoms and ions from hydrogen to calcium. *Zeitschrift für Physik* **216**, 241–247 (1968). URL http://dx.doi.org/10.1007/BF01392963.

[70] Lotz, W. Electron-impact ionization cross-sections for atoms up to Z=108. *Zeitschrift für Physik* **232**, 101–107 (1970). URL http://dx.doi.org/10.1007/BF01393132.

[71] Kim, Y. S. & Pratt, R. H. Direct radiative recombination of electrons with atomic ions: Cross sections and rate coefficients. *Phys. Rev. A* **27**, 2913–2924 (1983). URL http://link.aps.org/doi/10.1103/PhysRevA.27.2913.

[72] Müller, A. & Salzborn, E. Scaling of cross sections for multiple electron transfer to highly charged ions colliding with atoms and molecules. *Physics Letters A* **62**, 391 – 394 (1977). URL http://www.sciencedirect.com/science/article/pii/0375960177906727.

[73] Kimura, M. *et al.* A scaling law of cross sections for multiple electron transfer in slow collisions between highly charged ions and atoms. *Journal of Physics B: Atomic, Molecular and Optical Physics* **28**, L643 (1995). URL http://stacks.iop.org/0953-4075/28/i=20/a=003.

[74] Baumann, T. Spektroskopische Untersuchungen resonanter Rekombinationsprozesse an hochgeladenem Silizium in einer Elektronenstrahl-Ionenfalle (2012). Ph.D. Thesis. Ruprecht-Karls-Universität Heidelberg.

[75] Mäckel, V., Klawitter, R., Brenner, G., Crespo López-Urrutia, J. R. & Ullrich, J. Laser spectroscopy on forbidden transitions in trapped highly charged Ar^{13+} ions. *Phys. Rev. Lett.* **107**, 143002 (2011). URL http://link.aps.org/doi/10.1103/PhysRevLett.107.143002.

[76] Schnorr, K. *et al.* Coronium in the laboratory: Measuring the Fe XIV green coronal line by laser spectroscopy. *The Astrophysical Journal* **776**, 121 (2013). URL http://stacks.iop.org/0004-637X/776/i=2/a=121.

[77] Hertel, I. & Schulz, C. *Atoms, Molecules and Optical Physics 1: Atoms and Spectroscopy.* Graduate Texts in Physics (Springer Berlin Heidelberg, 2014). URL https://books.google.de/books?id=vr0UBQAAQBAJ.

[78] Currell, F. & Fussmann, G. Physics of electron beam ion traps and sources. *Plasma Science, IEEE Transactions on* **33**, 1763–1777 (2005).

[79] Welsch, C., Grieser, M., Ullrich, J. & Wolf, A. An ultra-low-energy storage ring at FLAIR. *Nuclear Instruments and Methods in Physics Research Section A: Accelerators, Spectrometers, Detectors and Associated Equipment* **546**, 405 – 417 (2005). URL http://www.sciencedirect.com/science/article/pii/S0168900205008776.

[80] Epp, S. W. Röntgen-Laserspektroskopie hochgeladener Ionen in einer EBIT am Freie-Elektronen-Laser FLASH (2007). Ph.D. Thesis. Ruprecht-Karls-Universität, Heidelberg.

[81] Bernitt, S. *et al.* An unexpectedly low oscillator strength as the origin of the Fe XVII emission problem. *Nature* **492**, 225–228 (2012). URL http://dx.doi.org/10.1038/nature11627.

[82] Rudolph, J. K. *et al.* X-ray resonant photoexcitation: Linewidths and energies of $K\alpha$ transitions in highly charged Fe ions. *Phys. Rev. Lett.* **111**, 103002 (2013). URL http://link.aps.org/doi/10.1103/PhysRevLett.111.103002.

[83] Buchauer, L. F. Konstruktion einer kompakten Elektronenstrahl-Ionenfalle mit Permanentmagneten für Fluoreszenzmessungen (2012). Bachelor Thesis. Ruprecht-Karls-Universität, Heidelberg.

[84] González Martínez, A. J., Crespo López-Urrutia, J. R. & Ullrich, J. State-selective quantum interference observed in the photorecombination of ions at the Heidelberg EBIT. *Radiation Physics and Chemistry* **75**, 1771 – 1777 (2006). URL http://www.sciencedirect.com/science/article/pii/S0969806X06002581. Proceedings of

the 20th International Conference on X-ray and Inner-Shell Processes 4-8 July 2005, Melbourne, Australia Proceedings of the 20th International Conference on X-ray and Inner-Shell Processes.

[85] Herrmann, G. Optical theory of thermal velocity effects in cylindrical electron beams. *Journal of Applied Physics* **29**, 127–136 (1958). URL `http://scitation.aip.org/content/aip/journal/jap/29/2/10.1063/1.1723053`.

[86] Soria Orts, R. Isotopic effect in B-like and Be-like argon ions (2005). Ph.D. Thesis. Johann Wolfgang Goethe - Universität in Frankfurt am Main.

[87] Klawitter, R. Resonant laser spectroscopy of a visible magnetic dipole transition in Ar^{13+} (2009). Diploma Thesis. Johann Wolfgang Goethe - Universität in Frankfurt am Main.

[88] Palmer, C. A. & Loewen, E. G. *Diffraction grating handbook* (Thermo RGL, 2002), 5 edn.

[89] Soria Orts, R. *et al.* Zeeman splitting and g factor of the $1s^2 2s^2 2p\ ^2P_{3/2}$ and $^2P_{1/2}$ levels in Ar^{13+}. *Phys. Rev. A* **76**, 052501 (2007). URL `http://link.aps.org/doi/10.1103/PhysRevA.76.052501`.

[90] Peck, E. R. & Reeder, K. Dispersion of air. *J. Opt. Soc. Am.* **62**, 958–962 (1972). URL `http://www.opticsinfobase.org/abstract.cfm?URI=josa-62-8-958`.

[91] Haynes, W. *CRC Handbook of Chemistry and Physics, 95th Edition*. CRC Handbook of Chemistry and Physics (Taylor & Francis, 2014).

[92] Chapman, S. & Lindzen, R. *Atmospheric Tides: Thermal and Gravitational*. Astrophysics and space science library (Reidel, 1970).

[93] Porto, J. V., Kink, I. & Gillaspy, J. D. Uv light from the ground term of Ti-like ytterbium, tungsten, and bismuth. *Phys. Rev. A* **61**, 054501 (2000). URL `http://link.aps.org/doi/10.1103/PhysRevA.61.054501`.

[94] Bekker, H. *et al.* Forbidden optical transition in Ti-like Xe, Ba, and Ir. *AIP Conference Proceedings* **1640**, 109–111 (2015). URL `http://scitation.aip.org/content/aip/proceeding/aipcp/10.1063/1.4905406`.

[95] Lapierre, A. *et al.* Relativistic electron correlation, quantum electrodynamics, and the lifetime of the $1s^2 2s^2 2p\ ^2P^o_{3/2}$ level in boronlike argon. *Phys. Rev. Lett.* **95**, 183001 (2005). URL `http://link.aps.org/doi/10.1103/PhysRevLett.95.183001`.

[96] Liang, G. Y. *et al.* Extreme-ultraviolet spectroscopy of Fe VI-Fe XV and its diagnostic application for electron beam ion trap plasmas. *The Astrophysical Journal* **696**, 2275 (2009). URL http://stacks.iop.org/0004-637X/696/i=2/a=2275.

[97] Crespo López-Urrutia, J. R. The visible spectrum of highly charged ions: A window to fundamental physics. *Canadian Journal of Physics* **86**, 111–123 (2008). URL http://www.nrcresearchpress.com/doi/abs/10.1139/p07-115. http://www.nrcresearchpress.com/doi/pdf/10.1139/p07-115.

[98] Bekker, H. *et al. J. Phys. B.* (2015). Submitted.

[99] Berengut, J. C., Flambaum, V. V. & Kozlov, M. G. Calculation of isotope shifts and relativistic shifts in C I, C II, C III, and C IV. *Phys. Rev. A* **73**, 012504 (2006). URL http://link.aps.org/doi/10.1103/PhysRevA.73.012504.

[100] Ritz, W. On a New Law of Series Spectra. *Astrophysical Journal* **28**, 237 (1908).

[101] Schmöger, L. Ein elektrodynamisches System für den Transfer hochgeladener Ionen in eine Paulfalle (2013). Diploma Thesis. Ruprecht-Karls-Universität, Heidelberg.

Danksagung

Abschließend möchte ich gerne den Menschen danken, die mich bei der Verwirklichung dieser Arbeit unterstützt haben. Es blieb immer spannend, mit überraschenden Wendungen und einem guten Ausgang in letzter Minute. Mein herzlicher Dank geht deswegen an:

- Joachim Ullrich, als Leiter der "Experimental Few-Particle Quantum Dynamics"-Abteilung, später abgelöst durch Thomas Pfeifer, und José R. Crespo López-Urrutia für das Ermöglichen dieser Arbeit. Besonderer Dank gilt dabei José R. Crespo López-Urrutia, der dieses Projekt tatkräftig und mit großem Einsatz betreute. Ich habe ihm eine intensive, sehr lehrreiche Zeit zu verdanken.
- Selim Jochim für die Übernahme des Zweitgutachtens.
- Michael Drewsen und Piet O. Schmidt für die Gastfreundschaft und Beratung innerhalb der Kollaborationsprojekte.
- Oscar O. Versolato und Hendrik Bekker für die freundschaftliche Zusammenarbeit. Ob mit Ideen oder Hämmern, durch ihre Kreativität, Begeisterung und Einsatz wurde der nächste Schritt nach vorne oft erst möglich. Trotz der vielen gemeinsamen Arbeitsstunden kann ich mich an keinen Moment erinnern, an dem nicht eine angenehme Atmosphäre herrschte.
- Maria Schwarz, die mir besonders während des ersten Jahres den Einstieg erleichterte und ein spannendes Experiment in Aarhus auf die Beine gestellt hat.
- Die vielen Unterstützer einer gewissen Strahlzeit, allen voran die FLASH EBIT Mannschaft Sven Bernitt, Stepan Dobrodey und René Steinbrügge.
- Die Projektpraktikanten, Bachelor- und Masterstudenten Victor Bock, Arnesh Daniel, Hugo Jeanperrin, Sebastian Kaul, Baptist Piest, Ruben Schupp, Julian Stark, Ji Wei Yoon, die an diesem Projekt engagiert mitgewirkt haben.
- Die Theoretiker, die mit Rechnungen und Diskussionen einen großen Anteil an der Lösung des Iridium-Puzzles hatten, vor allem Julian Berengut, Anastasia Borschevsky, Zoltán Harman und Natalia Oreshkina.
- Alle noch nicht genannten Mitglieder der EBIT-Gruppe für ihre Hilfsbereitschaft bei kleineren oder auch größeren Problemen: Tim Ballance, Thomas Baumann, Christian Beilmann, Sören Bieling, Michael Blessenohl, Andrii Borodin, Lisa Buchauer, Thore Bücking, Sita Eberle, Stefanie Feuchtenbeiner, Zachary Hockenbery, Daniel Hollain, Christian Kaiser, Sebastian Kebrich, René Klawitter, Kathrin Kromer, Steffen Kühn, Peter Micke, Paul Mokler, Eva Peper, Jan Rudolf und Lisa Schmöger. Ich bin sehr froh, in dieser kompetenten und sympathischen Gruppe gearbeitet zu haben.

Ich möchte mich herzlich auch bei meinen Freunden bedanken, die mir schon von klein auf zur Seite standen. Eva-Maria Schmitz möchte ich für all die Kraft und Liebe danken, die sie mir trotz eigener Verluste schenkte. Meine tiefste Dankbarkeit gilt meiner Familie und insbesondere meinen Eltern, Robert F. Windberger und Joana Windberger, die mich in allen Lebenslagen selbstlos unterstützt haben.